β-DELAYED PROTON EMISSION OF ^{71}KR

by

Waniganeththi Sanjanee Waniganeththi

Submitted to the College of science,
University of Massachusetts Lowell,
in partial fulfillment of the requirements for the degree of
MASTER OF SCIENCE
February 2021

β-DELAYED PROTON EMISSION OF ^{71}KR

BY

WANIGANETHTHI SANJANEE WANIGANETHTHI

B.S UNIVERSITY OF PERADENIYA (2015)

SUBMITTED IN PARTIAL FULFILLMENT OF THE REQUIREMENTS
FOR THE DEGREE OF MASTER OF SCIENCE
DEPARTMENT OF PHYSICS AND APPLIED PHYSICS
UNIVERSITY OF MASSACHUSETTS LOWELL

Signature of

Author: ______________________________ **Date:October 23, 2020**

Signature of Thesis

Supervisor: ______________________________

Name Typed: Anderw M. Rogers, Ph.D.

Signatures of Other Thesis Committee Members:

Committee Member Signature: ______________________________

Name Typed: Partha Chowdhury, Ph.D.

Committee Member Signature: ______________________________

Name Typed: Johannes Zwanikken, Ph.D.

β-DELAYED PROTON EMISSION OF ^{71}KR

BY

WANIGANETHTHI SANJANEE WANIGANETHTHI

ABSTRACT OF A THESIS SUBMITTED TO THE FACULTY OF THE

DEPARTMENT OF PHYSICS AND APPLIED PHYSICS

IN PARTIAL FULFILLMENT OF THE REQUIREMENTS

FOR THE DEGREE OF

MASTER OF SCIENCE

UNIVERSITY OF MASSACHUSETTS LOWELL

February 2021

Thesis Supervisor: Anderw M. Rogers, Ph.D.

Associate Professor, Department of Physics and Applied Physics

ABSTRACT

Neutrons and protons can be considered as two states of the same particle, the nucleon, due to their similarities such as mass. This consideration is supported by observations of particular symmetries between protons and neutrons which have played an important role historically in nuclear physics. Nuclei in the vicinity of the $N = Z$ line have been subject to many experimental investigations to understand their nuclear structure as they allow a sensitive probe of these symmetries, formalized under the concept of isospin. Therefore, the structure and decay properties of $N \approx Z$ nuclei underlie our understanding of this symmetry. One such system is the ^{71}Kr/^{71}Br mirror pair and is the focus of this thesis. The character of the ground states of both ^{71}Kr and ^{71}Br, which should have the same spin-parity, has been under discussion for many years. In these studies, a debate has ensued as to whether the ground-state spin of ^{71}Kr is 5/2 or 1/2. Properties of this mirror system were investigated in an implant-decay experiment conducted at the National Superconducting Cyclotron Laboratory (NSCL) using a beam containing ^{71}Kr, produced by projectile fragmentation of a ^{92}Mo primary beam and purified with the Radio Frequency Fragment Separator (RFFS). The purified beam was implanted into the Beta Counting Station (BCS) surrounded by the Segmented Germanium Array (SeGA). This sensitive β-decay experiment was utilized to constrain the spins assigned for low-lying energy levels of ^{71}Br and the ground state of ^{71}Kr. A correlation method was employed to deduce the half-life, decay branches, and other properties of the β-decay. A precise half-life of 95.6 ± 0.4 ms was deduced for ^{71}Kr, based on a sample of 698955 implantations. The results obtained from β-delayed proton emission and γ-ray spectroscopy enabled an extension of the known β-decay scheme. In particular, we report the first experimental observation of β-decay branching to the 407-keV state of ^{71}Br and the delayed-proton feeding to the first excited 2+, 943-keV state of ^{70}Se. The intensity of observed 943-keV γ-ray transitions provides evidence that the spin of ^{71}Kr must be greater than 3/2 supporting the predictions of mirror symmetry.

DEDICATION

To my family

ACKNOWLEDGEMENTS

I will begin by thanking my supervisor, Prof. Rogers, for providing both an interesting and varied masters project while affording me plenty of opportunity to participate in other experiments as well. The other academics at university of Massachusetts, Lowell nuclear physics research group, Prof. Chowdhury, Prof.Lister and Prof.Bender, have also been a constant source of support. I am also grateful to Prof. Zwanikken, for always being willing to give comments, advice and corrections.

A big thank you to postdoc of our group, Dr. Hoff, that I learned so much about this particular project as well as programming. Thank you for your insights and conversations to breakup my tense work days. The remainder of the nuclear physics research group at university of Massachusetts, Lowell also deserve a lot of credit for being really nice friends.

The support of my family has been invaluable. Without them none of this would have been possible. To my sister, for her kindness and taking care of my Mom and Dad when I am many miles away from home.

To my friends: Keshani and Ketaki, for their love and support, for their time and just for being such incredible people and a source of inspiration in a middle of a pandemic.

I would like to thank everyone who has supported me during my academic career, and apologies if I have not named you.

Table of contents

List of Figures

List of Tables

1 INTRODUCTION

1.1 Overview of atomic nuclei

Nuclei form the core of atoms, the building blocks of the chemical elements that make up us and the environment around us. The idea that atoms consists of a nucleus was first proposed by Ernest Rutherford in the 19^{th} century after his "gold-foil" experiment. Since then, the nucleus of an atom has been found to be made of protons and neutrons, collectively called nucleons, defined by their proton number, Z, and neutron number, N. The mass number A of a nucleus is given by the total number of nucleons. The interaction between nucleons is dominated by the strong force, and one of the main challenges of nuclear physics is to understand the structure of nuclei on the basis of the interactions strictly between neutrons and protons.

When both types of nucleons are combined together, they can form a rich variety of nuclear systems. There are around 7000 theoretically predicted such systems, out of which about 300 nuclei are known to be stable. The number of protons Z in the nucleus characterizes each element in the periodic table of elements, while the number of neutrons N can be different for each element and defines the isotopes of a certain element. If all isotopes are placed in a 2D-diagram of Z, N one can obtain the so-called chart of the nuclides, also known as the Segré Chart shown in Fig. 1.1. Since $A = N + Z$, nuclei are typically denoted by their chemical name and total mass number, ${}^{A}X$, where X is the chemical symbol assigned to a given Z.

Certain combinations of protons and neutrons in isotopes of an element result in a stable nucleus. In the chart of nuclides there are roughly 300 stable nuclides that are naturally abundant on earth and these are shown in black squares in Fig. 1.1. If the chart of nuclides were plotted with a third axis showing the mass (total relativistic energy) of each nucleus, a deep valley emerges along the stable nuclei; the so-called "valley of stability".

Not all combinations of protons and neutrons lead to a configuration that is stable with respect to a spontaneous transformation. This transformation is referred to as radioactivity or radioactive decay and was discovered in the 19^{th} century by Becquerel and explored by Marie Curie at the turn of the century. Commonly observed radioactive decays are $\beta^{\pm}$ decay, electron capture (discussed further on), α-decay, and spontaneous fission. There also exist other types of exotic decays, such as proton emission (one of the main focuses of this work) in the proton-rich part of the Segré Chart.

In the lower mass region (up to A $\approx$ 40) of the chart of nuclides, most of the stable nuclei lie near the line of symmetry (N = Z) as the Coulomb interactions generated by protons is overcome by the attractive strong force between nucleons. However, when the mass number increases the line of stability bends towards larger number of neutrons as more strong force is

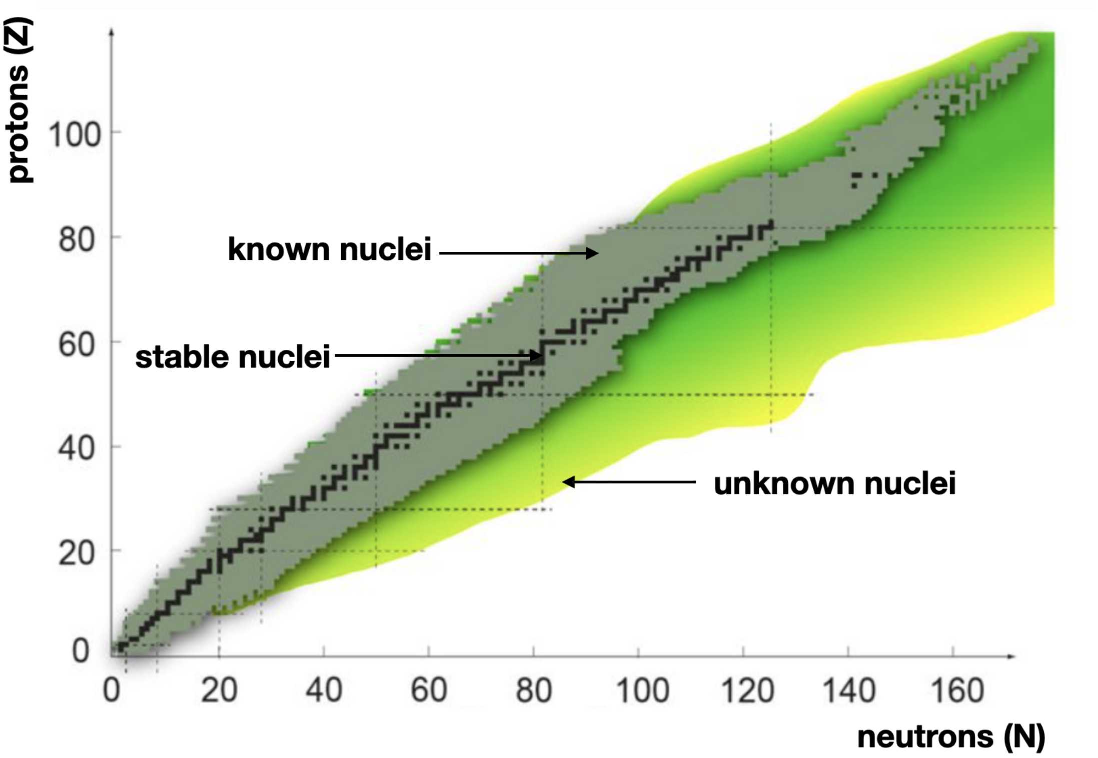

Figure 1.1: Schematic overview of the knowledge of nuclei in the chart of nuclides.[33]

needed to compensate for Coulomb repulsion.

Excessive proton and neutron numbers lead to decreasing stability of the nucleus. If, for example, more and more neutrons are added to a nucleus of given proton number, the binding energy of the last neutron drops steadily and at a certain neutron number, the nucleus decays instantaneously by neutron emission, i.e. the nucleus becomes unbound and the neutron drip line is reached.

When the extremes of the nuclear chart are reached, where a proton or neutron cannot be added (i.e. the nucleus is no longer particle-bound) the proton or neutron will "drip-off" marking the so-called drip lines. Unstable nuclei located next to drip-lines are often referred to as "exotic" nuclei. The proton drip-line is rather well known (increasing Coulomb forces drive it to be less stable), but the region of heavier neutron-rich nuclei still forms a wide terra incognita as shown in yellow and green colours in Fig. 1.1.

1.2 Properties of nuclei

Due to their small-scale structure, atomic nuclei are governed by quantum mechanics. Consequently, two important and fundamental properties of nucleons are their orbital angular momentum and intrinsic spin. Nucleons are often thought of as moving in an effective central potential of the nucleus, which gives each a constant orbital angular momentum ℓ. Within a single-particle description of the nucleus, an orbit is assigned depending on the angular momentum quantum number, where the usual spectroscopic notation is adopted,

$$\ell = 0, 1, 2, 3, 4, ... \tag{1.1}$$

$$s, p, d, f, g, ... \tag{1.2}$$

Nucleons are also fermions, which means their intrinsic spin, s, is a half-integer, specifically $s = \frac{1}{2}$ for neutrons and protons. For a nucleon in the nucleus the total nucleon angular momentum is often called "nucleon spin" j, obtained by the vector addition of orbital angular momentum and intrinsic spin,

$$j = l + s. \tag{1.3}$$

The spin (total angular momentum) for a given nucleus that contains A nucleons should be the vector sum of the spin (total angular momenta) for the constituent nucleons. This is referred as the Nuclear Spin, and typically denoted by J. This vector addition is a complicated process, since we would need to know the total angular momentum (consequently l and s) for each individual nucleon. But, to a good approximation, the nucleus can be treated as a collection of independent nucleons that move in an effective field. Therefore, the nucleons are paired up in orbits such that their momenta cancel with each other. This means that the remaining valence (unpaired) nucleons will be left to determine the nuclear spin J. Therefore, only the unpaired nucleons contribute to total spin J.

When discussing about nuclear structure another important quantity to consider is parity, which can be described as the inversion of sign for all spatial coordinates of the nuclear wavefunction. Like nuclear spin, parity π is an intrinsic property of the nuclear wave function, and can either take an even (+) or odd (−) value,

$$\pi = (-1)^{\ell} \tag{1.4}$$

Thus, the total nuclear parity is dependent on the parity of each of the individual nucleons as is the case for nuclear spin. Like nuclear spin, it is also a property of the nucleus as a whole. Therefore, the wave function of the remaining valence (unpaired) nucleons will be left to determine the overall parity. Spin and parity denoted by J^{π} is used as the notation to label the nuclear energy states.

1.3 Mirror Nuclei

Another quantity that is useful for nuclear physicists is isospin, which arises from the similarities of neutrons and protons. Nuclei with exchanged numbers of protons and neutrons are known as mirror nuclei. As a consequence of isospin symmetry, if the properties of one of the nuclei in this mirror pair is known, the properties of the other can be inferred since the neutrons and protons have just interchanged roles. These mirror nuclei provide a unique way to study and test the isospin symmetry and probe the differences between protons and neutrons [47][12]. One such property that is largely constant between mirror pairs is the ground-state spin and parity. Since the proton and neutron numbers are merely exchanged, mirror nuclei should have an identical set of states, including their ground states. The difference in their binding energies is mainly due to the different Coulomb energy in two mirror systems, since one will have more protons. An example of this mirror symmetry is shown by comparing the level schemes of $^{50}_{26}\mathrm{Fe}_{24}$ and $^{50}_{24}\mathrm{Cr}_{26}$ shown in Fig. 1.2.

Ernest Rutherford proved that the nucleus of the hydrogen atom (i.e. a proton) is present in the nuclei of all other atoms in the year 1917. After the discovery of neutron by James Chadwick in 1932 [8], Heisenberg [17] introduced the term nucleons for treating neutrons and protons as two states of one particle. In 1937 Wigner [52] proposed the idea of isospin space and isospin quantum number, T, to quantify Heisenberg's idea. A convenient way of dealing with this formally is to introduce the concept of isospin as an abstract, extra degree of freedom which is analogous to spin, S. The individual nucleon states in this new subspace are equivalent to the "up" and "down" states of a particle with spin $s = 1/2$.

In this representation neutrons and protons can be interpreted as the up and down states of a single particle, the nucleon, having isospin value $t = 1/2$. In nuclear physics, the proton is usually designated $t_z = -1/2$ (down) and $t_z = +1/2$ (up) for the neutron. The additional quantum number, T, stands for the length of the total isospin vector, $\vec{T}$, and whose projection on the quantization axis is defined as $T_z = \frac{N-Z}{2}$.

When there is invariance under a transformation, there is always a related conserved quantity. The inability to distinguish between up and down states in isospin space implies that nuclear forces are invariant under rotations in isospin space. This means that isospin should be conserved in strong interactions. States of the same spin and isospin in nuclei with the equal mass numbers form a multiplet, and are generally called isobaric analogue states (IAS).

Level schemes for nuclei in such isobaric multiplets, which may include an $N = Z$, nuclei as well as neighboring mirror nuclei, illustrate this symmetry. For example, isobar diagrams of $^{10}_{4}\mathrm{Be}_6$, $^{10}_{5}\mathrm{B}_5$ and $^{10}_{6}\mathrm{C}_4$ are shown in Fig. 1.3. The ground-state spin and parity of the mirror nuclei $^{10}_{4}\mathrm{Be}_6$ and $^{10}_{6}\mathrm{C}_4$ are similar, but in addition we find analogous states (of the same spin and parity

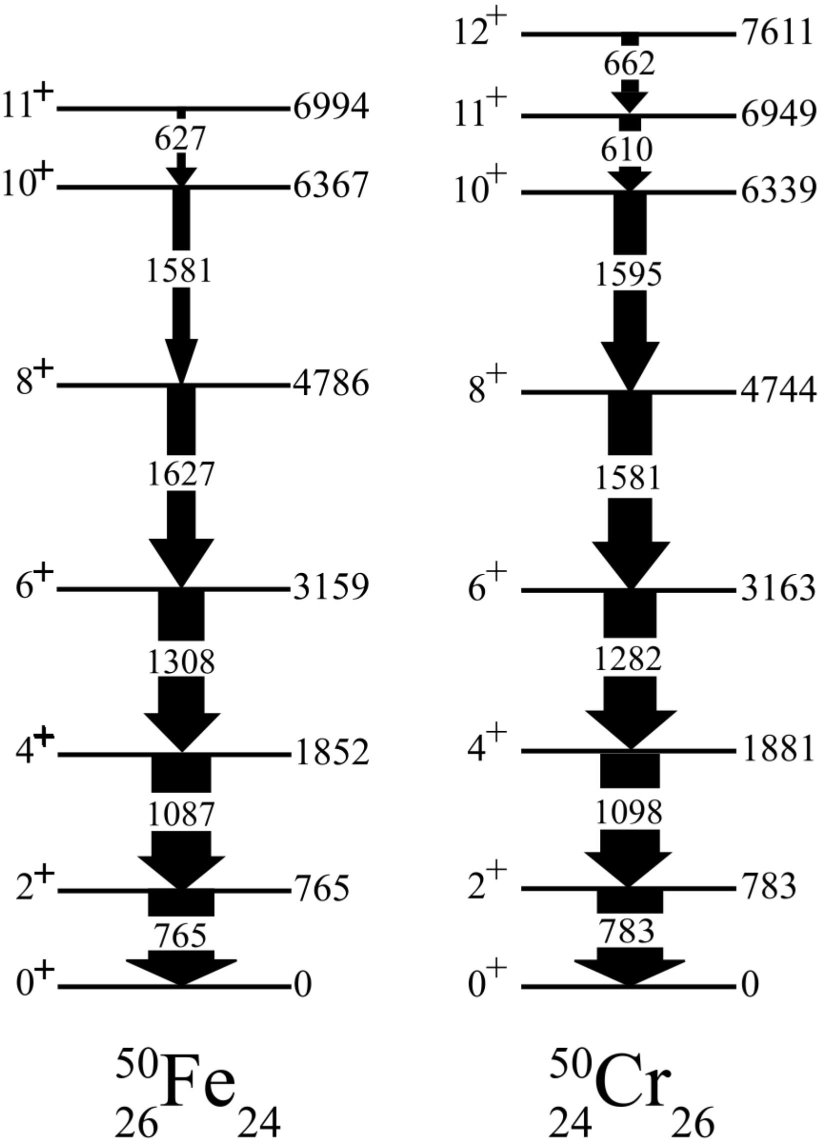

Figure 1.2: Comparison of the level schemes of $^{50}_{26}\mathrm{Fe}_{24}$ and $^{50}_{24}\mathrm{Cr}_{26}$. This plot shows only positive-parity levels and the energy difference between the ground states have been removed. The excitation energies of the states with the same total angular momentum J and parity π exhibit close similarity in mirror nuclei. Figure taken from Ref. [25].

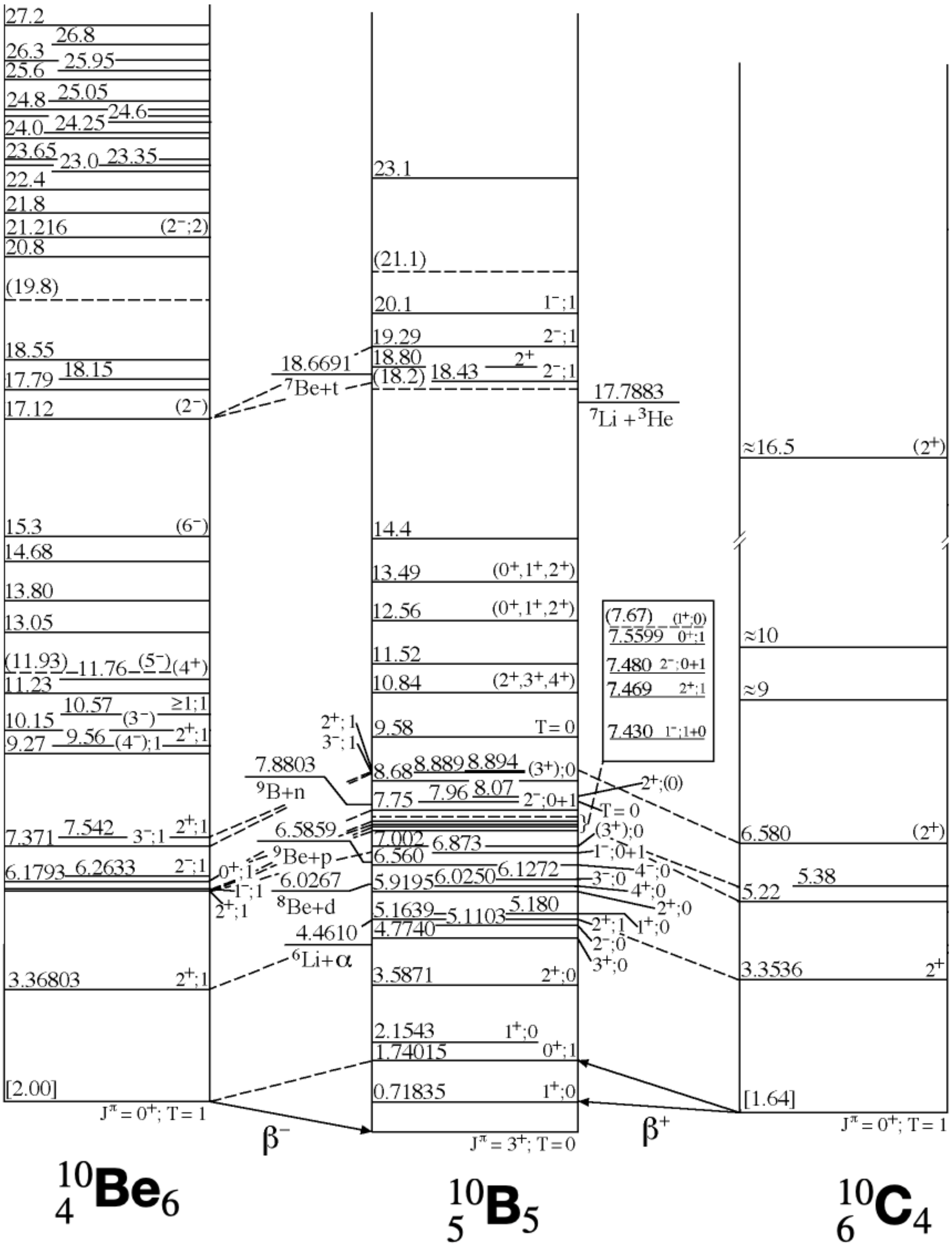

Figure 1.3: Comparison of the level schemes of $^{10}_{4}\mathrm{Be}_6$, $^{10}_{5}\mathrm{B}_5$ and $^{10}_{6}\mathrm{C}_4$. Figure taken from Ref. [1]

and similar excitation energy) among the low-lying states in ${}^{10}_{5}\mathrm{B}_5$ (only these analogue states are connected in dashed lines in Fig. 1.3). The difference in the binding energies of the isobars is mainly due to the different Coulomb energy generated by the different number of protons. Therefore, the isobar diagrams account for the shift in Coulomb energy. The similarities of the spectra allow us to conclude that the total nuclear interaction energy of the many-nucleon system is (almost) invariant under interchange of neutron-neutron, neutron-proton, and proton-proton interactions.

Under the assumption of charge independence (the forces between the nucleons are independent of the charge) of the strong interaction, hence invariance under rotation in the isospin space, the excitation energy spectra of mirror nuclei should be almost identical. In nuclear physics the observation of almost identical decay schemes between mirror nuclei [29], [51], [53] and [37] highlights the robustness of isospin symmetry. Apart from the mass difference between neutron and proton, isospin symmetry is definitely broken by the Coulomb interactions which only act on the protons.

However, isospin symmetry is only an approximate symmetry of the nuclear Hamiltonian due to the presence of electromagnetic interactions, isospin non-conserving components of the strong force, and differences between the neutron-protron (np) masses. The largest source of the isospin-symmetry breaking (ISB) is the Coulomb interaction between protons. But the difference between the binding energies between the isobaric analogue states (the so-called Coulomb Displacement Energy CDE), that are nuclei in the same isospin multiplet, cannot be described by simple differences in the electromagnetic force alone, as studied in detail by Nolen and Schiffer [35].

Although isospin-symmetry breaking has been observed in many unbound systems, there was previously only one case where weak binding of nuclei resulted in different ground states of a mirror pair. Recently, isospin-symmetry violation has been observed in the bound ground states of the mirror pair ${}^{73}\mathrm{Sr}/{}^{73}\mathrm{Br}$ by Hoff et al.[19].

The focus of this thesis is to address the mirror symmetry between ${}^{71}_{35}\mathrm{Br}_{36}$ and its mirror partner ${}^{71}_{36}\mathrm{Kr}_{35}$, which has been under debate for more than a decade, as well as understand nuclear structure in this mass region. To answer this question, data from an experiment at the National Superconducting Cyclotron Laboratory (NSCL) was analyzed where there was a strong population of ${}^{71}\mathrm{Kr}$. These ions were implanted into a detector and their decay properties measured. Through observing ${}^{71}\mathrm{Kr}$ decay, including branching leading to β-delayed proton emission, the properties its ground state are deduced. The remainder of this chapter will present background on general nuclear physics related to decays as well as previous knowledge about the ${}^{71}\mathrm{Kr}/{}^{71}\mathrm{Br}$ mirror pair.

1.4 Background on Nuclear Decays

This section will review relevant radioactive decay modes that nuclei undergo, such as β-decay, γ-decay and proton decay. Detailed knowledge about these decay processes will enable a better understanding of decays of nuclei of interest for this thesis, specifically ^{71}Kr. Furthermore it will be helpful to review the previous studies on ^{71}Kr, as well as the techniques used in the NSCL experiment such as β-spectroscopy, γ-spectroscopy and proton spectroscopy.

1.4.1 β-Decay

The three main β-decay processes occurring in nuclei, all mediated by the weak interaction, are β^--decay, β^+-decay and orbital electron capture ϵ. These processes convert neutrons into protons or vice versa, and are represented as:

$$\beta^- : X_{(Z,N)} \rightarrow X_{(Z+1,N-1)} + e^- + \overline{\nu}_e, \tag{1.5}$$

$$\beta^+ : X_{(Z,N)} \rightarrow X_{(Z-1,N+1)} + e^+ + \nu_e, \tag{1.6}$$

$$\epsilon : X_{(Z,N)} + e^- \rightarrow X_{(Z-1,N+1)} + \nu_e, \tag{1.7}$$

where e^- is an electron, e^+ is a positron, $\overline{\nu}_e$ is an electron anti-neutrino and ν_e is the electron neutrino. In general, unstable nuclei undergo β decay along a given isobar (nuclei with constant mass number) chain until they reach their lowest-energy, most stable nuclei.

The Q value of the reaction is the difference in energy between the reactants (initial state) and products (final state) in a nuclear process, and thus define the total available energy given to the products. For the case of β decay, the energy difference between the two ground states of the parent and the daughter nucleus define the Q value,

$$Q_{\beta^-} = [M_P - M_D]c^2, \tag{1.8}$$

$$Q_{\beta^+} = [M_P - M_D - 2m_e]c^2, \tag{1.9}$$

$$Q_{\epsilon} = [M_P - M_D]c^2, \tag{1.10}$$

where M_P and M_D are the nuclear masses of the parent and daughter nuclei, respectively, m_e is the mass of the electron and c is the speed of light.

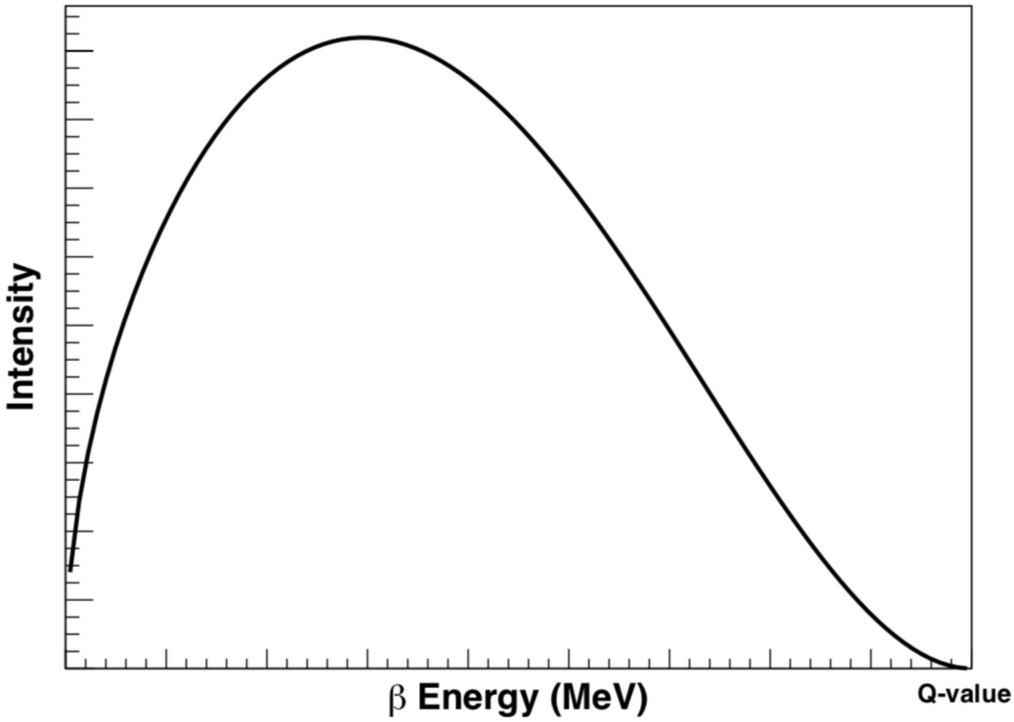

Figure 1.4: An illustration of the expected energy spectrum for a β particle. Image adapted from [18].

β^- and β^+-decays occur through three-body emission. Due to this, β particles are emitted with a continuum of energies up to the β-decay Q value, as the emitted neutrino takes away a portion of the total energy. The recoiling nucleus takes very little energy, because it is massive, compared to the leptons(β and neutrino). The angular momentum is also conserved and is shared between recoiling parent nucleus, emitted β-particle and the (anti)neutrino. The conservation of angular momentum also plays a role in the probability of decay from a particular initial state to a final state.

β decays are classified as either Gamow-Teller (GT) or Fermi depending on the spin orientation of emitted fermions, and thus the total angular momentum of the electron/positron and neutrino. If the electron and the neutrino spins are anti-parallel it is known as a Fermi decay and in GT decay the spins are aligned. Therefore, the total spin of the electron/position and neutrino is zero for Fermi decay whereas it is 1 for GT decays.

$$S_e + S_n = S_{total} = 0 \tag{1.11}$$

$$S_e + S_n = S_{total} = 1 \tag{1.12}$$

If there is no change in the angular momentum (Δl=0), the decays are named as allowed and

Decay Mode	ΔI	$\Delta\pi$	Δl
Allowed	0,1	no	0
First-Forbidden	0,1,2	yes	1
Second-Forbidden	2,3	no	2
Third-Forbidden	3,4	yes	3
Forth-Forbidden	4,5	no	4

Table 1.1: β-decay selection rules [24].

others are forbidden. Although forbidden transitions do occur with the decreasing probability for each incremental change in the angular momentum. Selection rules for the allowed and forbidden decays are:

In 1934, Fermi developed a theory for β-decay based on neutrino hypothesis. The transition rate for a β-decay from initial state i to final state f under the influence of weak interaction is given by Fermi's Golden Rule [24],

$$\lambda = \frac{2\pi}{\hbar}|V_{fi}|^2\rho(E_f), \tag{1.13}$$

where V_{fi} is the interaction matrix element and $\rho(E_f)$ is the density of final states.

The interaction matrix element which determines the overlap between the initial and final wave functions can be written as,

$$V_{fi} = \int \psi_f^* V \psi_i d\tau \tag{1.14}$$

where ψ_i is the initial nuclear wave function or the parent nuclear wave function, ψ_f represent the wave function of final nuclear state (daughter nuclear wave function), electron and neutrino wave functions and dτ is the volume integral.

The density of final states can also be written as dn/dE_f where the number of states dn in energy interval dE_f. A given interaction is more likely to happen if there is more overlap between initial and final states as well as more energy-accessible final states.

The transition probability for β-decay is often referred to in terms of the log(ft) of the transition. The Fermi integral, f, is a dimensionless quantity given by [24],

$$f(Z^{'}, E_0) = \frac{1}{(m_e c)^3 (m_e c^2)^2} \int_0^{p_{max}} F(Z^{'}, p) p^2 (E_0 - E_e)^2 dp \tag{1.15}$$

where m_e is the mass of the electron, c is the velocity of light, E_0 is the maximum electron energy, i.e. the decay end-point, E_e and p are the kinetic energy and momentum of the electron (or positron) respectively and $Z^{'}$ is the atomic number of the daughter nucleus. The function $F(Z^{'}, p)$ is known as the Fermi function. The comparative half-life gives a measure of changes in the nuclear matrix element, M_{fi}, [24]:

Decay Mode	log*ft*
Super-allowed	2.9-3.7
Allowed	4.4-6.0
First-Forbidden	6-10
Second-Forbidden	10-13
Third-Forbidden	>15

Table 1.2: Typical log *ft* value for β-decay modes [24]

$$ft_{\frac{1}{2}} = 0.693\frac{2\pi^3\hbar^7}{g^2 m_e^5 c^4 |M_{fi}|^2}, \tag{1.16}$$

with,

$$\lambda = 0.693/t_{1/2} \tag{1.17}$$

β-decay *ft* values range from 10^3 to 10^{20} s and thus, the log*ft* is often quoted to cover the wide range of *beta*-decay half-lives and also denote how likely a transition is to occur. The decays with the smallest possible $\log(ft)$ values ($\approx$ 3-4) are more likely to occur.

β-delayed particle (proton or neutron) emission has also been observed since the earliest days of nuclear physics. More specifically β-delayed proton emission was initially observed in 1960 [21]. β-delayed proton emission of heavier nuclei, in particular $\beta -$-γ-spectroscopy is used as an important tool to probe nuclear structure along the proton dripline [5].

β-decays are able to populate excited states in their daughter nuclei from the ground state nearly up the Q value of the reaction (though this becomes increasingly unlikely with increasing excitation energy of the daughter). Near the proton dripline, excited states of the daughter nucleus can be populated that are greater than the proton separation energy as shown in Fig. 1.5. This allows for decay processes to occur which may otherwise be energetically forbidden such as delayed proton emission.

β-delayed proton emission is a two-step process. The first step is through the β-decay process, the daughter nuclide is formed in an excited state, which is unstable against proton or gamma emission. The second step is the proton emission from the excited states of the nucleus. Furthermore, proton decay is generally faster than γ-decay to the ground state of daughter nuclei.

When moving from the valley of stability towards more neutron-deficient (proton-rich) nuclei the separation energy of the last proton, S_p gets smaller and smaller (less bound) and eventually when the proton drip-line is crossed S_p becomes negative. The half-life of the proton emission depends on the energy and the angular momentum carried by the proton, as it has to tunnel through the Coulomb barrier and the centrifugal barrier arising from the orbital angular mo-

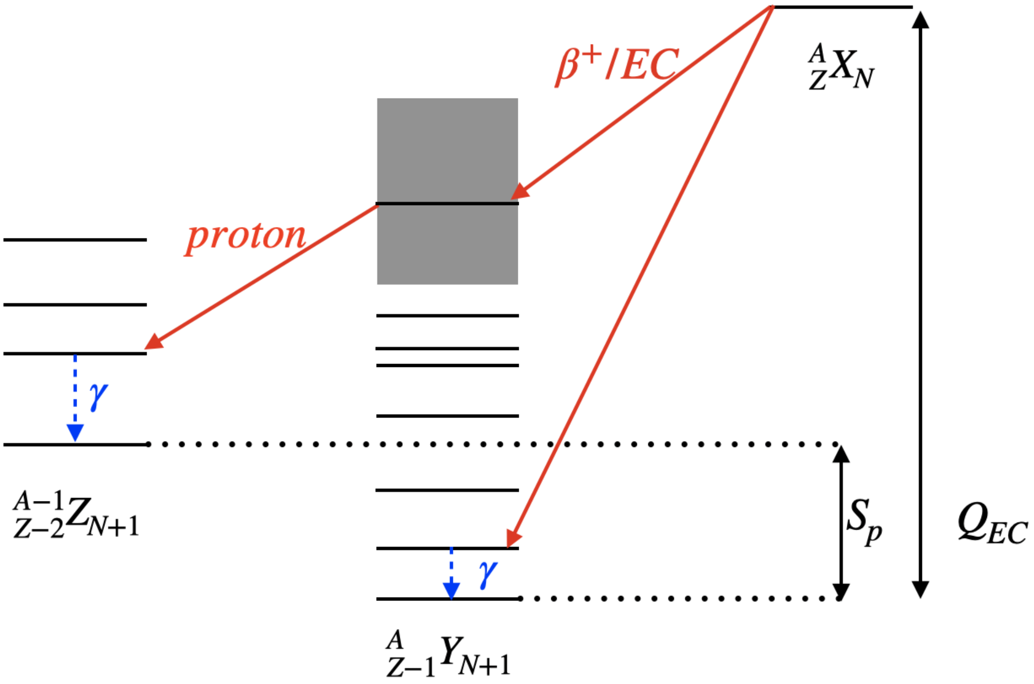

Figure 1.5: Schematic decay scheme illustrating the βp-emission. β-decays to daughter excited states above proton separation energy can result in a subsequent proton decay. The gray coloured box represents the continuum of levels above proton separation energy.

mentum of the emitted proton [6]. In particular β-delayed proton emission of ^{71}Kr is known to be very prompt(fast). But there are β-delayed proton emitters that have half-lives in the range of ms such as ^{101}Ho and ^{131}Eu [9] due to high angular-momentum barriers.

β-delayed proton emission manifests itself differently in light and heavy nuclei [6]. In light nuclei protons are emitted from discrete energy levels, and therefore the proton-energy spectra have well separated peaks. But in heavy nuclei the energy levels above the proton separation energy threshold have a high level density, as shown in Fig.1.5, which causes the proton-energy spectrum to have broader structures. These structures are commonly observed in nuclei far from stability, which have high β-decay Q value and low proton separation energy.

1.4.2 γ-Decay

Many nuclear reactions, such as α and β decay, leave the daughter nucleus in an excited state. These excited states can then decay to the ground state through electromagnetic processes called γ decay. A γ ray is a photon of electromagnetic radiation which has a discrete energy equal to the energy difference of initial and final states of nuclear decay. The excited states of nuclei have specific energies defined by the shell structure of the given nucleus, much like atomic transitions. γ decay can be represented as:

$$^{A}X^{*} \rightarrow ^{A}X + \gamma. \tag{1.18}$$

γ-ray energy spectra thus consist of discrete peaks that correspond to the energy difference of the intial and final levels with typical energies ranging from 10-keV to 10-MeV. If the half-life of a particular energy level is in the order of nanoseconds or more, it is known as an isomeric state which tends to decay through other excited states with one or more transitions ending on the ground state.

Every γ-ray carries one unit of intrinsic angular momentum, and in a given transition, the angular momentum should be conserved. The angular momentum of states in discrete values as $I\hbar$. The change in angular momentum $\Delta I = (I_i - I_f)\hbar$ should be carried out by the emitted γ-ray.

The emission of a γ-ray is caused by the rearrangement of protons or neutrons in the nucleus, which have an electric or a magnetic character associated with it. The knowledge of the change in angular momentum and parity between initial and final state can be used to figure out the electric or magnetic nature of the transition. For example, even ΔI values in transitions with no change in parity ($\Delta\pi$ = no) require electric transitions and odd values require magnetic transitions. The reverse is true for change in parity ($\Delta\pi$ = yes) transitions. The relation can be described as:

$$\Delta\pi(M) = (-1)^{\Delta I + 1}, \tag{1.19}$$

$$\Delta\pi(E) = (-1)^{\Delta I}. \tag{1.20}$$

In addition, the transition rates depend on the energy of the photon and the mass of the decaying nucleus. Weisskopf derived both electric and magnetic transition rates in terms of the energy and the mass, by assuming the transition is from the change of a single particle inside a nucleus of uniform density. The electric transition of the same multipolarity is more favourable than its magnetic transition. Moreover, lowest order multipolarity of any transition type will tend to dominate.

1.5 Previous Measurements of ^{71}Kr

^{71}Kr is an unstable nucleus which has approximately equal number of neutrons and protons as it located next to line of symmetry (N = Z) in chart of nuclides as shown in Fig. 1.6. The half-life

ΔI	Electric transition rate	Magnetic transition rate
1	$1.0 \times 10^{14}A^{2/3}E^{3}\gamma$	$3.1 \times 10^{13}A^{2/3}E^{3}\gamma$
2	$7.3 \times 10^{7}A^{4/3}E_{\gamma}^{5}$	$2.2 \times 10^{7}A^{2/3}E_{\gamma}^{5}$
3	$3.4 \times 10^{1}A^{2}E_{\gamma}^{7}$	$1.0 \times 10^{1}A^{4/3}E_{\gamma}^{7}$
4	$1.1 \times 10^{-5}A^{8/3}E_{\gamma}^{9}$	$3.3 \times 10^{-6}A^{2}E_{\gamma}^{9}$

Table 1.3: Weisskopf single particle transition rates [24].

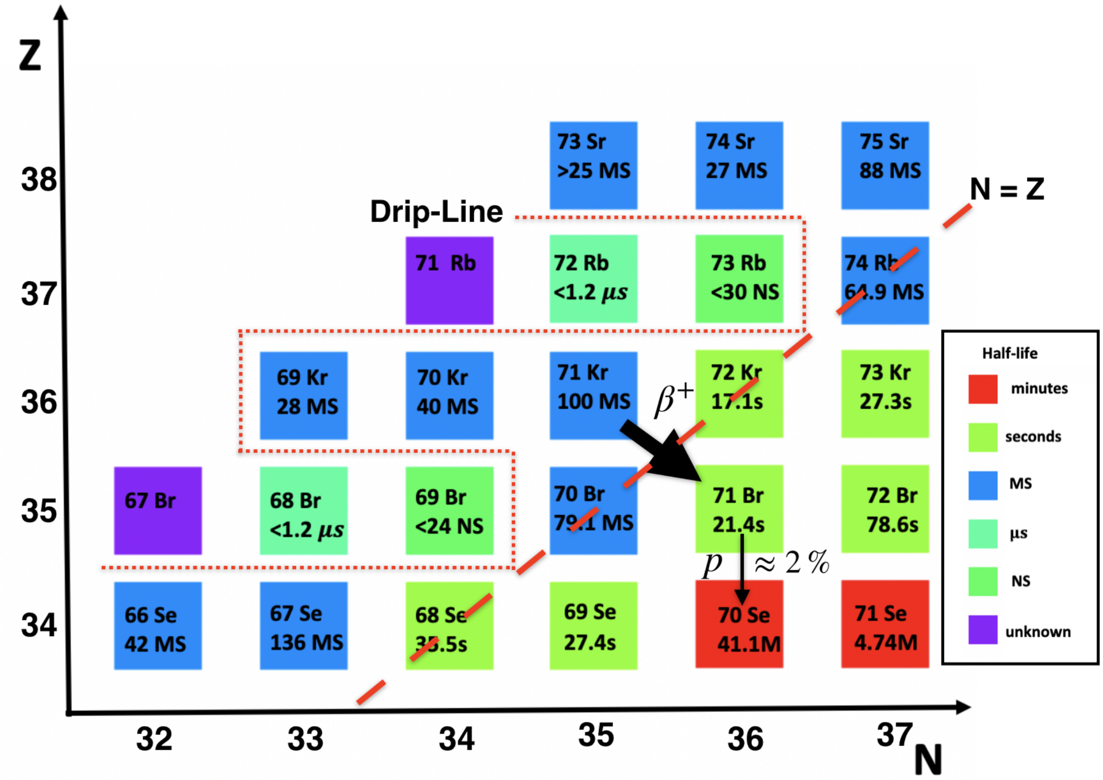

Figure 1.6: The nuclear landscape in the region of interest for the present work. The dotted line indicates the proton drip-line, while the dashed line represents the N=Z line. Colours indicate the half-life of β-decay.

of ^{71}Kr is in the range of milliseconds, decaying through the β^+/EC-decay. For decay along the isobar, the decay chain ends at the stable ^{71}Ga.

The character of the ^{71}Kr ground state, specifically its spin and parity assignment, has been under debate for many years. The current state of knowledge about the ^{71}Kr and its β-decay daughter ^{71}Br is based on an single β-decay experiment on ^{71}Kr [36] and another in-beam high resolution γ-spectroscopy experiment on ^{71}Br [14].

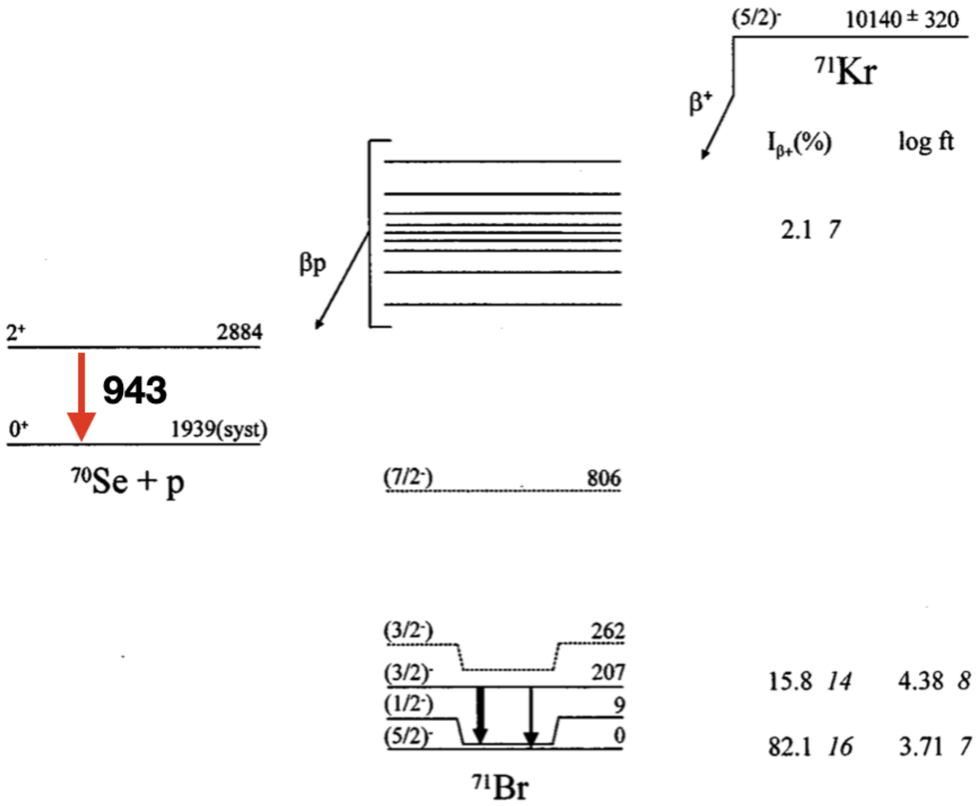

Figure 1.7: The decay scheme of ^{71}Kr adapted from [36]. Unobserved levels are represented in dashed lines. β-decay to 262-keV $3/2^-$ state in ^{71}Br and proton decay to 2^+ state in ^{70}Se were not observed. The existence of 262-keV state was excluded from the ^{71}Br decay scheme based on the observations by Fischer et al.[14].

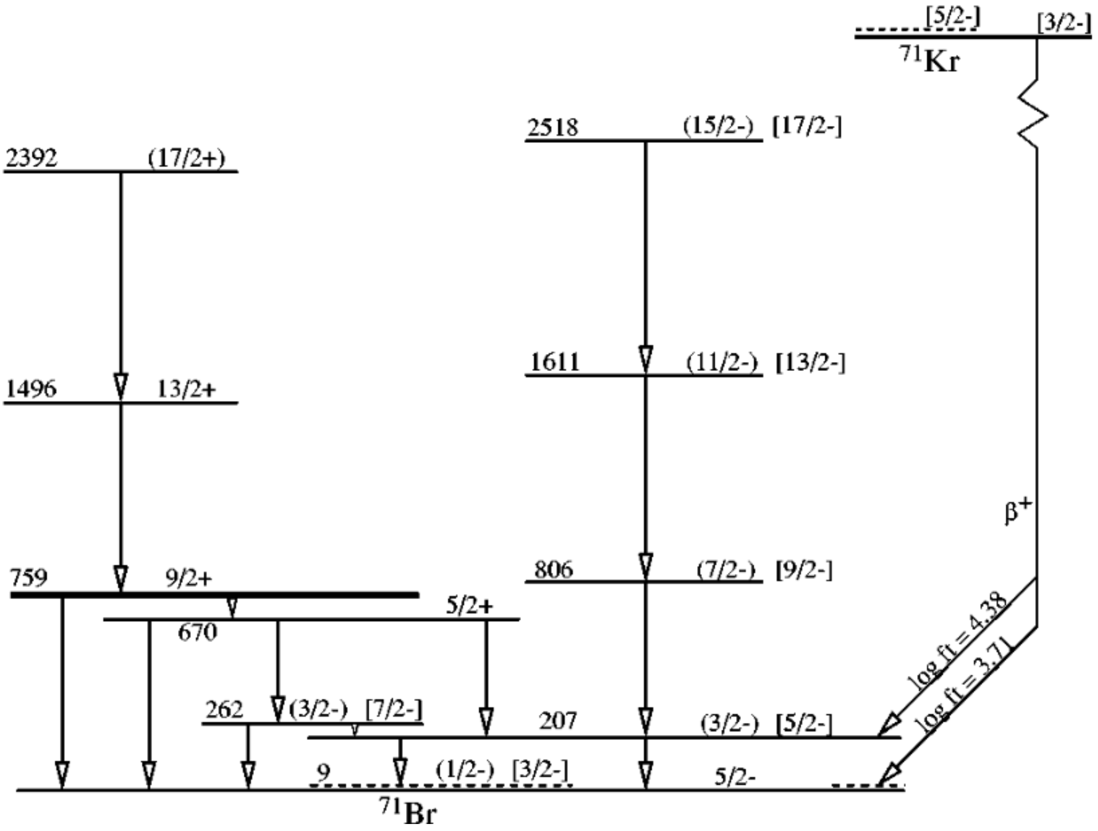

Figure 1.8: The decay scheme of ^{71}Kr reported by [49] based on the theoretical interpretation of log *ft* values of Oinonen et al. [36]. The spin assignments proposed by Urkedal et al. are within square brackets.

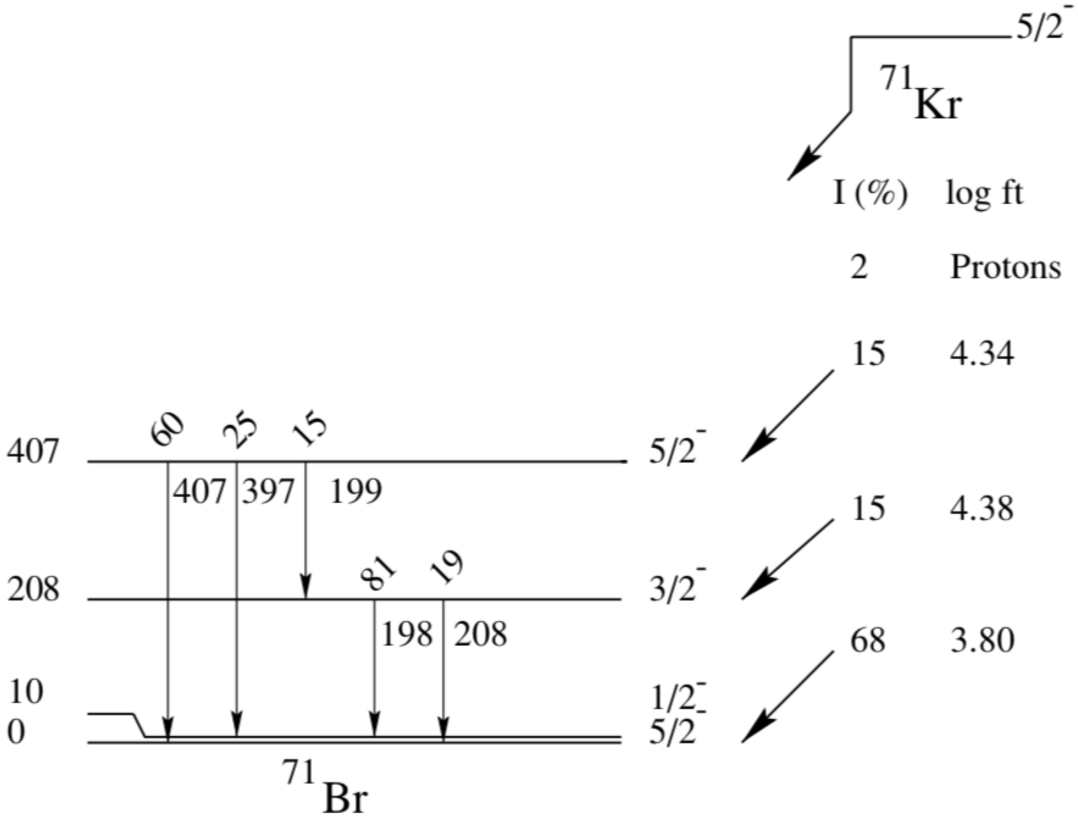

Figure 1.9: The deduced β-decay scheme of ^{71}Kr based on in-beam spectroscopic measurement of ^{71}Br, following the ^{40}Ca(^{40}Ca,$2\alpha p$) fusion-evaporation reaction at 160-MeV using Gammasphere. [14].

The report on β-spectroscopy of ^{71}Kr to ^{71}Br was by Oinonen et al. [36] at ISOLDE. In their study they observed β-decay to two states, the ground state and 208-keV state as shown in Fig. 1.7. Even though the 262-keV third excited state has been assigned a J^{π} of $3/2^-$ at the time, they failed to observe any feeding to that state. This was the key motivation for Urkedal and Hamamoto [49] work of theoretical interpretation of log *ft* values published by Oinonen et al.

According to Oinonen et al. the ground state of ^{71}Br should be $5/2^-$, the same as its mirror partner ^{71}Kr. Therefore the β-decay to the ground state is of Fermi type. Urkedal and Hamamoto claimed that the log *ft* value of 3.71 for the ground state decay of ^{71}Kr reported by Oinonen et al. might consist of contribution the closely spaced 9-keV $1/2^-$ first-excited state. Furthermore, they claimed that the sensitivity of the detection system used by Oinonen et al. was not good enough to resolve the two contributions.

At the time of the Oinonen et al. study the spin and parity of the states of ^{71}Br (9-keV, 208-keV and 262-keV) were not experimentally fixed, a fact used by the theoretical study of

Urkedal and Hamamoto. The failure of Oinonen et al. to observe the first order Gamow-Teller decay to one of the closely spaced level (262-keV) led them to assign different J^{π} to low-lying states of ^{71}Br and ^{71}Kr. According to Urkedal et al. the ground state of ^{71}Kr is $3/2^{-}$ and ^{71}Br is $5/2^{-}$. Furthermore, the assigned Fermi decay is from the ground state of ^{71}Kr to the 9-keV $3/2^{-}$ state of ^{71}Br. This theoretical interpretation by Urkedal et al. suggested the possibility that the ^{71}Kr/^{71}Br mirror pair have different ground states as ^{71}Br is known to have an almost degenerate ground state. If true, this would be the first known violation between ground states of bound mirror nuclei.

The lack of information about the ^{71}Br level scheme hinders insight into this issue. Consequently, in 2005, Fischer et al.[14] performed an in-beam spectroscopic measurement of ^{71}Br, following the ^{40}Ca(^{40}Ca,$2\alpha p$) fusion-evaporation reaction at 160 MeV using Gammasphere. In their study many new states were observed. Based on these observations a modified detailed decay scheme was published. The existence of the 262-keV state was excluded and a 407-keV state included as shown in Fig. 1.9. Interestingly, the β-gated γ-ray spectrum (Fig.1) of Oinonen et al. provides some evidence of β-decay branching to these states as peaks can be observed in their spectra around 397-keV and 407-keV (See Fig.1 in [36]).

Based on the detailed decay scheme deduced by Fischer et al. a modified β-decay branching for ^{71}Kr was published which is shown in Fig. 1.9. The spin parity assignment contradicted the Urkedal and Hamamoto assignments. The ground state of ^{71}Br was therefore assigned a J^{π} of $5/2^{-}$ whereas the 10-keV was assigned $1/2^{-}$.

The assumption of an inversion of this low-energy doublets by Urkedal and Hamamoto was not supported by Fischer et al. According to the interpretation by Urkedal and Hamamoto the ground state of ^{71}Kr which a J^{π} of $3/2^{-}$ was assigned would be a second forbidden decay to 407-keV $5/2^{-}$ state. The log *ft* for that decay found to be 4.34 which is relatively low for a decay of that kind. Hence, the assignment of $5/2^{-}$ for ground state of ^{71}Kr remains consistent and the mirror symmetry between these two pair is preserved and confirmed.

However, the assignment of $3/2^{-}$ for the ground state of ^{71}Kr cannot be fully discarded, as this inversion of a similar low-energy doublet has recently been observed in this region by Hoff at al. [19]. ^{73}Sr/^{73}Br have almost degenerate ground states and a state inversion between these nuclei was suggested in the observed β-delayed proton emission data. In order to eliminate the contradiction in the ^{71}Kr/^{71}Br case a more sensitive β-decay experiment on ^{71}Kr was needed. One of the two suggestions by Fischer at al. was to observe the population of $7/2^{-}$ states as this would completely remove the uncertainty of the spin of the ^{71}Kr ground state.

Apart from the spin-parity assignment issue another interesting observation by Oinonen et al. [36] is the proton decay from states above the proton-separation energy in ^{71}Br, as shown in Fig. 1.7. However, the overall population to states above particle threshold is only about 2% [36][14]. Since this a small fraction of the total overall branching, any signs of γ de-excitation in the $\beta - p$ decay daughter, ^{70}Se, were not observed. This is unfortunate, as feeding to the 2^+ level would aid in further constraining the decay properties.

1.6 Scope of this study

Based on the previous studies, to settle the puzzle of the ^{71}Kr/^{71}Br mirror system, the nature of the ground state in ^{71}Kr needs to be determined. An investigation of excited states of ^{71}Kr and a sensitive β-decay experiment of ^{71}Kr could provide the necessary additional information to confirm the $1/2^-$ or $5/2^-$ spin assignment for the ground state of ^{71}Kr.

This dissertation details a study of the β-delayed proton emission of ^{71}Kr in order to achieve the following goals: (a)the β-decay half life, (b) observe the β decay feeding states predicted by Fisher et al. as well as any β-decay feeding to $J^\pi = 7/2^-$ states in ^{71}Br and (c) observe proton decay to states predicted by Oinonen et al. Furthermore, be used to support a determination of the ^{71}Kr ground-state properties.

To achieve the above goals, this thesis relies on an implant-decay experiment that was conducted at the National Superconducting Cyclotron Laboratory on the campus of Michigan State University. The facility is capable of providing beams of short-lived nuclei (frequently referred to as rare isotopes or exotic nuclear beams) for nuclear structure and reaction studies as well as other fundamental physics.

A detailed description of the experiment and setup is given in Chapter 2. Chapter 3 and Chapter 4 report the analysis of raw data and results including the first evidence of the existence of the predicted states and decays in both ^{71}Br and ^{70}Se by Fisher et al. and Oinonen et al. Finally, Chapter 5 provides further analysis that can be performed to extract additional information beyond those contained in this thesis.

2 EXPERIMENT

The experiment was performed at the National Superconducting Cyclotron Laboratory (NSCL) at Michigan State University (MSU) in October 2017, under NSCL experiment number 12024. The facility is capable of producing rare nuclides using an in-flight fragmentation technique. A primary beam of heavy nuclei collides with a light fixed target and undergoes projectile fragmentation. The fragments of interest (consisting of rare isotopes) are allowed to be transmitted through the accelerator system, while the rest of the unwanted fragments are filtered out by the A1900 fragment separator. The experiment also utilized the Radio Frequency Fragment Separator (RFFS), otherwise known as the "RF-kicker", which is helpful for reducing contamination in proton-rich beams. The resulting secondary beam was delivered to the experimental end station where it was implanted into a stack of silicon detectors surrounded by an array of high-purity germanium detectors. This detector setup enabled both the identification of each implanted heavy ion and measurement of its subsequent correlated emission of charged particles (e.g. protons and positrons) and γ-ray photons.

The primary goal of the experiment was to investigate the "waiting-point" nucleus ^{72}Kr which is important for the astrophysical rapid proton (rp) capture process, by studying β-delayed proton emission of ^{73}Sr. However, ^{71}Kr was one the most intensely produced ions in the secondary beam and formed the basis for this study. This chapter presents the experimental setup in detail which was utilized to produce and study ^{71}Kr.

2.1 Isotope production

At NSCL, radioactive nuclei are produced by the process called projectile fragmentation. The stable projectile nuclei, which form the primary beam, are accelerated up to 40% the speed of light by two coupled-cyclotrons. A fully stripped ^{92}Mo beam was impinged on a stationary target

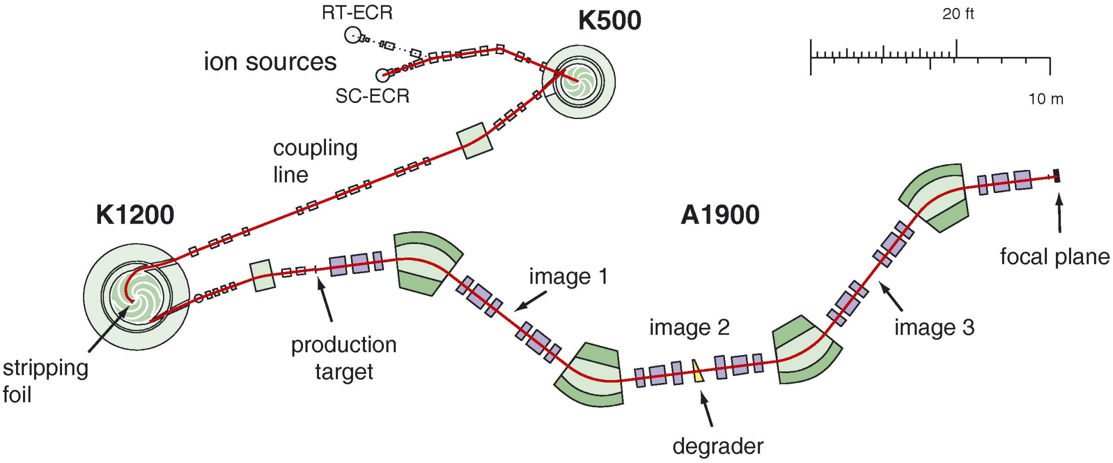

Figure 2.1: Layout of K500, K1200 and A1900 components of NSCL [42]

causing some of the projectile nuclei to fragment. This projectile fragmentation reaction outputs a cocktail beam of fragments which are filtered by the A1900 fragment separator and, for this particular experiment, the Radio Frequency Fragment Separator (RFFS) before transported to the experimental end-station.

The nuclei for this study were produced by accelerating a stable ^{92}Mo beam up to 120-MeV/nucleon utilizing the K500 and K1200 coupled cyclotrons at NSCL. Figure 2.1 shows a diagram of the coupled-cyclotrons and the A1900 at the NSCL. The accelerated beam impinged up on 152.2-mg/cm^{-2} Be target. A two-step process, called abrasion-ablation, will be followed in nucleus-nucleus collision fragmentation [27]. In the first step the projectile will be fragmented to two or more nuclei which are left in excited states. Ablation is the process in which those excited nuclei lose excess nucleons. However, all fragments will be left with sufficient forward momentum to be transported to A1900 fragment separator[26].

2.1.1 A1900 Projectile fragment separator

The A1900 separator utilizes both magnetic rigidity and energy filtering in combination, known as $B\rho$--$B\rho$ technique to separate fragments. $B\rho$, or magnetic rigidity, is defined as:

$$B\rho = mv/q, \tag{2.1}$$

where B is the magnetic field strength, ρ the radius of curvature, m the mass, v the velocity and q the charge state of the ion. The nuclei produced by fragmentation have nearly the same velocity which is approximately equal to the velocity of ^{92}Mo primary beam. Therefore the first A1900 filter selects nuclei based on their mass to charge (m/q) ratio as the fragments have different (m/q) values. Ions selected by first $B\rho$ filter will pass to second filter in the series which induces an energy loss. The differential energy loss of an ion passing through a material can be deduced from the Bethe-Bloch equation,

$$-\frac{dE}{dx} \propto \frac{AZ^2}{E}, \tag{2.2}$$

where A is the atomic mass of the ion, Z the fragment nuclear charge and E the energy of the fragment. The degrader material was a 120-mg/cm^3 thick wedge-shaped Aluminium to keep the achromatic condition (all trajectories focus to a spot and have approximately a same path length) for the isotopes in interest[27]. The third filter in the A1900 is a magnetic rigidity filter which mostly filters out large beam dispersion introduced by the first two filters.

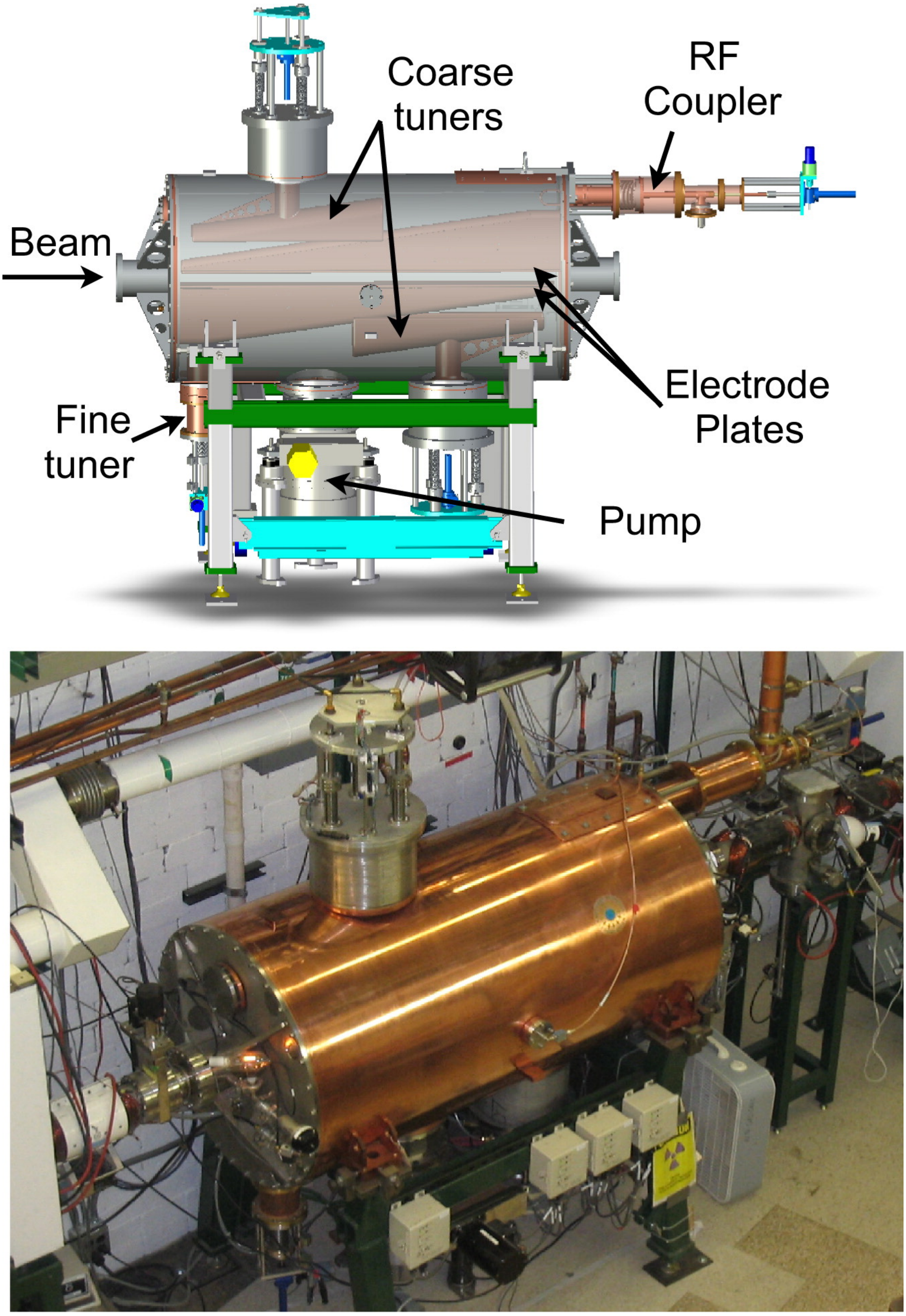

Figure 2.2: A mechanical drawing (top) and a photograph (bottom) of RFFS [4].

Parameter	Effective value
K1200 Radio-frequency	23.18 MHz
^{92}Mo Projectile Energy	140 MeV/neucleon
^{9}Be Target Thickness	152.204 mg/cm^2
$B_{\rho 1,2}$	3.1231 Tm
Dispersive Image Al wedge	122.785 mg/cm^2
$B_{\rho 3,4}$	2.9487 Tm

Table 2.1: K1200 and A1900 settings for the ^{71}Kr production runs.

2.1.2 Radio frequency Fragment Separator (RFSS)

Production of ^{71}Kr through projectile fragmentation produces a cocktail of unwanted fragments that dominate the beam composition. Dumping such a beam into the implantation detector can inflate the overall rate to unmanageable levels. Additional selective beam reduction was required beyond that usually achieved at NSCL with the A1900 separator. Therefore, the NSCL Radio Frequency Fragment Separator, was implemented to reduce the beam rate, while also making the beam cleaner, such that the implant-decay correlations of ^{71}Kr are experimentally tractable.

For a given projectile fragmentation reaction with intermediate projectile energies, roughly between 50-200 MeV/nucleon, the momentum distributions of produced nuclei are found to be asymmetric [4]. Most of the stable fragments are found at low magnetic rigidity where the nuclei of interest will also fall in. Therefore, even after A1900 magnetic rigidity filtering considerable amount of contaminants will still be present.

The selection mechanism for the RFFS is based on filtering out ions that have different velocities. The RFFS applies a sinusoidal electric field perpendicular to the direction of the beam. The beam itself, is pulsed with the frequency of the K1200 cyclotron. Different ions are spread-out in time within the beam packet (pulse) due to different velocities. The ions which enter the chamber at different times and will experience a different magnitude of electric field, depending on the frequency, resulting in different vertical deflections.

The frequency of the oscillating electric field in RFFS is equal to the K1200 cyclotron frequency so that each beam pulse will experience the same amplitude of electric field. The particles of interest will then be deflected above vertical slits, filtering out the unwanted isotopes, with the remaining nuclei transported to the experimental end station.

2.2 Experimental Setup

The purified beam utilizing the mechanisms described in the previous section, was delivered to an experimental end station located downstream in the NSCL S2 vault as shown in Fig. 2.4. The β-counting station (BCS) is a Si detector telescope used for continuous ion implantation, beta or proton decay correlation and particle identification. The segmented Germanium array

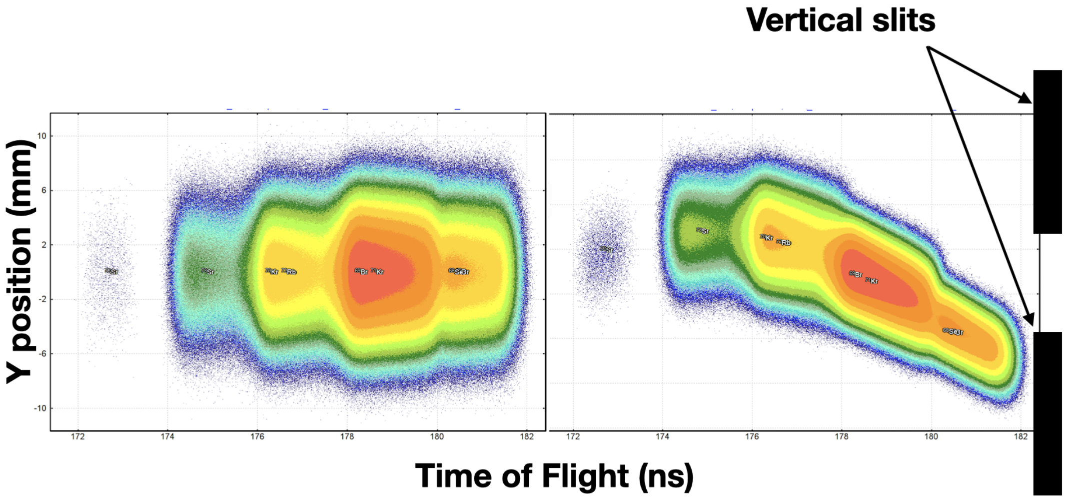

Figure 2.3: LISE++ [44] simulation for Y position of a beam pulse (left) before and (right) after RFFS.

(SeGA) was used for $\beta - \gamma$ spectroscopy and $\beta - p - \gamma$ spectroscopy.

2.2.1 β-Counting Station

The BCS allows for event-by-event correlations by implanting nuclei which undergo β decay and subsequent particle decays.

The schematic of BCS is shown in Fig. 2.5, with a 1041-μm silicon PIN detector is furthest upstream, serving as the energy-loss detector for particle identification. A variable-thickness Al degrader was next, and the thickness was selected such that the ions of interest lose a sufficient amount of energy to be stopped in the middle of the implantation detector. A 996-μm thick silicon PIN detector is used as the time of flight stop signal since the first PIN was not able to be used as the time of flight stop detector.

The fourth component of the telescope is the implantation detector which is a 520-μm thick 40-mm × 40-mm Double-Sided Si-Strip Detector (DSSSD). The DSSSD is segmented into 40, 1mm strips on both x and y directions allowing for the extraction of the implantation or decay position along with the energy. The DSSSD was given adequate space on either side so as to not hinder the γ rays emitted by the implanted ions. The last detector of the telescope was a 989-mm thick silicon single sided strip detector (SSSD) intended to be used as a β detector. At the end of the telescope a plastic scintillator was used as a veto detector to eliminate the ions that were not stopped in the DSSSD.

Even though the BCS allows for event-by-event correlations of implantation and decay, a successful correlation will depend on the rate and the make-up of the beam. Following an

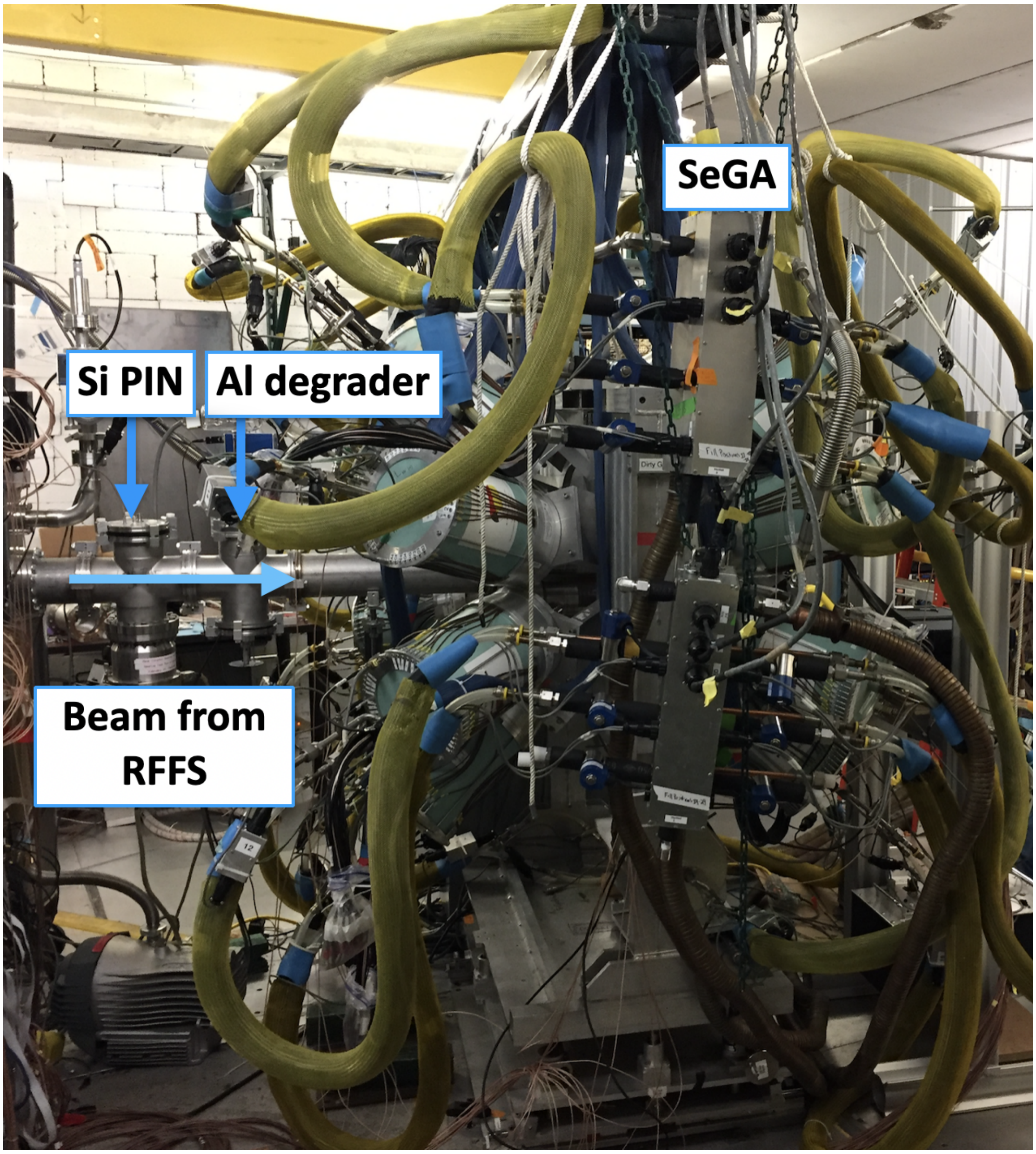

Figure 2.4: A photograph of the experimental end station at NSCL.

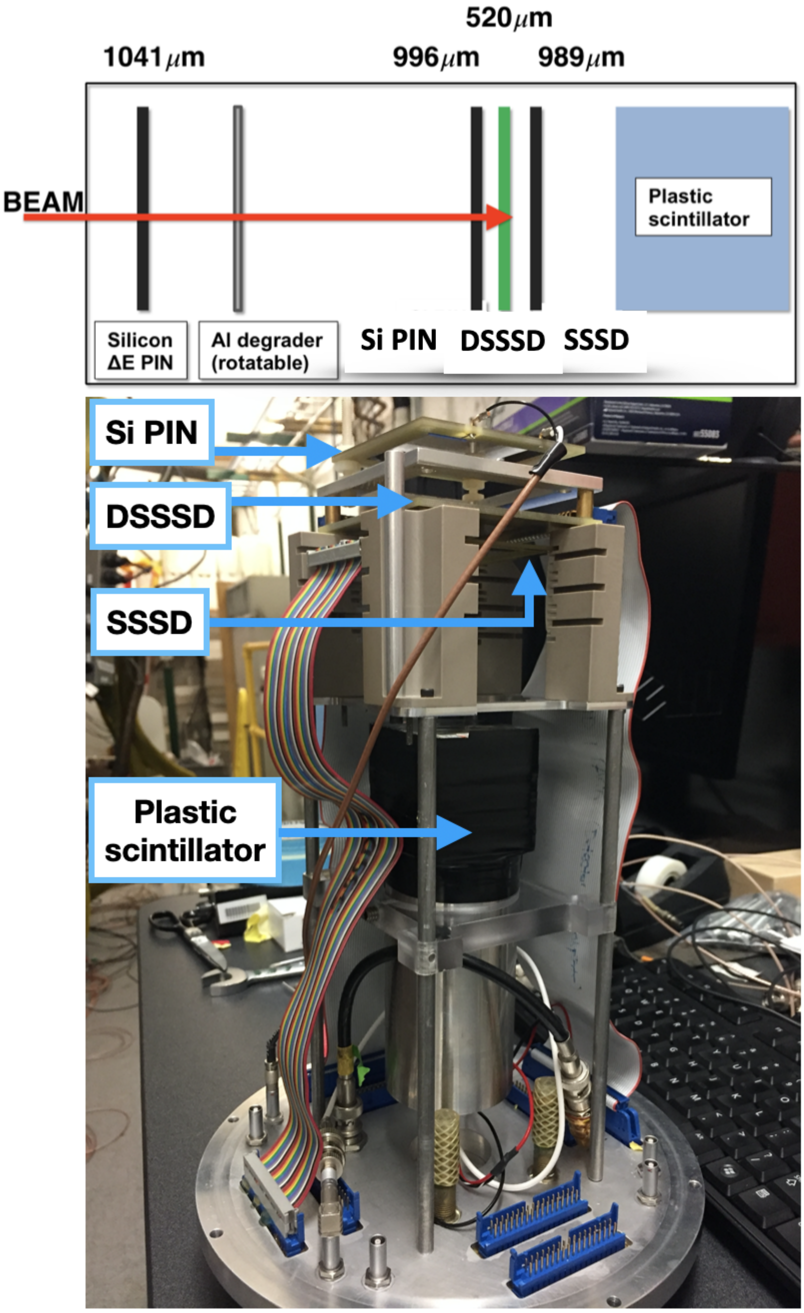

Figure 2.5: A schematic diagram and a photograph of beta counting station.

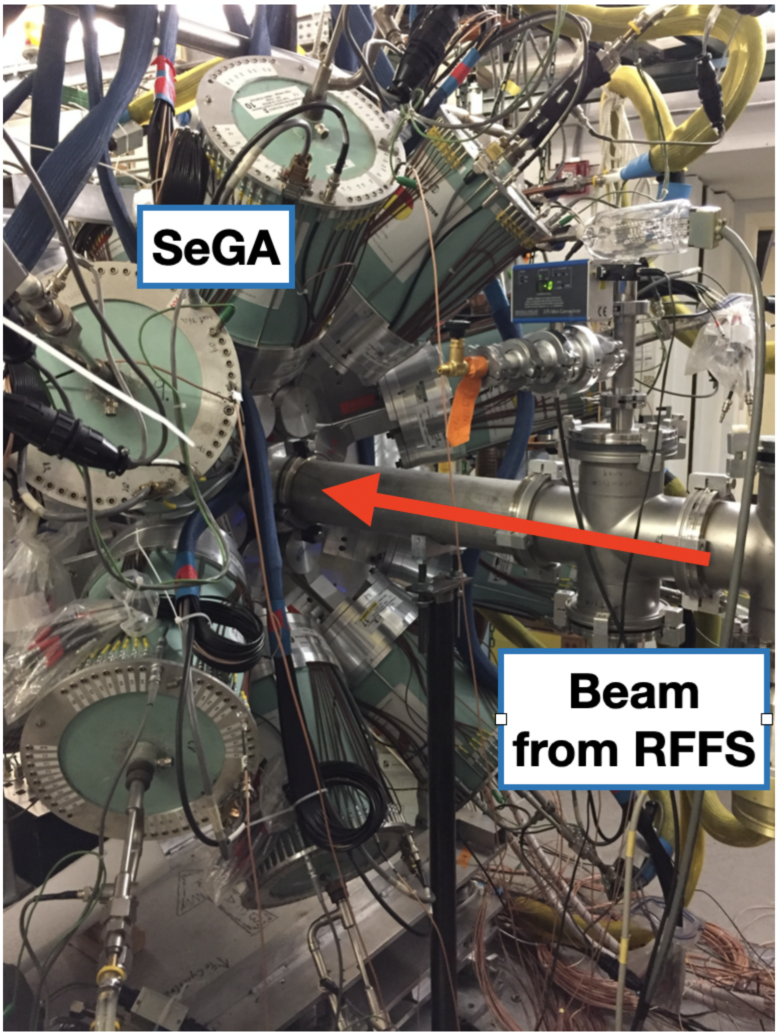

Figure 2.6: A photograph of the set-up. The beam pipe is surrounded by SeGA.

implantation, a given pixel or few nearest neighbour pixels were monitored for a time determined according to the half-life for the nuclei of interest. If the implantation rate is too high, that pixel can receive another ion prior to the detection of β decay of first implantation poisoning the correlation. The A1900 fragment separator and the RFFS were used to reduce the implantation rate required by BCS.

2.2.2 Segmented Germanium Array

The segmented Germanium array (SeGA) consists of 16 Ge crystals. Each crystal is divided into eight 10 mm disks along the length of the Ge cylinder. Then, each disk is subdivided into four quarters making a single crystal into 32 segments in total. The segmentation of the array provides improved position resolution to reduce uncertainty in the Doppler correction done for in-beam experiments. This particular experiment was focused on the γ rays emitted after the implantation of ions, hence a Doppler correction is not necessary.

As shown in the Fig. 2.6, each detector was mounted to two detector rings which are located upstream of BCS and downstream. The frame which holds all detectors is designed in such a way that all detectors cylindrical axis is parallel to the beam axis. The separation between two concentric rings is only a few mm's which allows for the cylindrical crystals to be closely packed and to maximize the overall detection efficiency of the γ rays emitted from the nuclei implanted on DSSSD.

3 DATA ANALYSIS

The raw data produced and recorded during the experiment were further processed to determine the correlations of the implanted ions, which requires a good understanding of the data acquisition system. Electrical signals generated by the detectors were digitised and acquired through the NSCL digital data acquisition (DDAS) system. With DDAS, event-by-event data were collected during the experiment, encoded and written to a computer for further processing in offline analysis. The data analysed in this thesis were generated by two main detector systems: the BCS and SeGA as described in the previous chapter. To properly process the basic signals into a form from which the physics of interest can be extracted the detectors must be calibrated, and their performance understood. The energy and efficiency calibrations and analysis of the data collected during the experiment are discussed in this chapter.

First, the calibration of the experimental end station is presented. The second section focuses on how the particle identification (PID) was done and the improvements made in the offline analysis. The implant-decay event correlations and logic are presented in the next section. In the final section, the DSSSD trace analysis is outlined, resulting in a reduction in the uncorrelated background.

3.1 Calibration of the experimental station

3.1.1 SeGA calibration

When a germanium detector measures a single γ-ray photon, it places this count in a channel. For the same energy photon this count will be in a different channel in different germanium detectors. Each germanium crystal detector has a different response to the same energy. Therefore calibration sources, which emit a decay pattern with known γ-ray peaks at known energies, are measured in the detectors so that one can match the channel numbers in each detector with the correct energies. The experimenter must plot the channel number at which each peak occurs vs. the known energy of said peak from the calibration source. This plot is then fitted with a linear which is then used when the raw data is scanned into a histogram. Thus the channel number in each germanium crystal detector is transformed into a correct energy number in keV.

In order to see if there were any significant shifts in the experimental setup, SeGA was calibrated twice during the experiment. The calibration performed at the end of the experiment was used for the offline analysis. A ^{60}Co source and a Standard Reference Material (SRM) [34] containing ^{125}Sb, ^{125m}Te, ^{154}Eu, and ^{155}Eu was used for the calibration. An SRM source, or standard reference material source, is used because the absolute amount of γ decays per second are known for the time in which the source was created. The corresponding γ-energies and

Isotope	γ-Energy (keV)	Emission Rate (γ s^{-1}) 1200 EST September 1, 1988
^{154}Eu	123.1	3.460 $\times 10^4$
^{154}Eu	247.7	5.864 $\times 10^3$
^{154}Eu	591.8	4.197 $\times 10^3$
^{154}Eu	723.3	1.703 $\times 10^4$
^{154}Eu	873.2	1.034 $\times 10^4$
^{154}Eu	996.3	8.850 $\times 10^3$
^{154}Eu	1004.7	1.534 $\times 10^4$
^{154}Eu	1274.5	2.958 $\times 10^4$

Table 3.1: Prominent γ-rays and emission rates of SRM [34] used for SeGA calibrations.

original activity are listed in the Table 3.1.

The second type of calibration is for efficiency of detecting γ-ray photons at different energies.The detectors do not cover a total 4π solid angle, thus not all γ-ray photons can be intercepted from the activity on tape. But even if they were covering total solid angle, not all γ-ray photons will deposit their energy in the germanium. Some may pass through without interaction or Compton scatter all or part of their energy. There is a relationship between the energy of the photons and the efficiency with which the germanium detectors measure them. From zero keV up to approximately 80 keV, the efficiency of detection generally rises with increasing energy. This is because with higher energy photons they are less likely to be absorbed by materials which are housing the germanium crystals. Above this point the efficiency generally decreases, but the rate of decrease depends on the energy range. To determine this curve of efficiency vs. photon energy, γ-ray sources are utilized and a source whose date of creation and absolute activity at the time of creation must be measured. Thus the absolute rate of γ-rays per second at the time of measurement is calculated from knowing the half-life for each energy emitted from said source. Measuring how many decays per second occur in the detectors vs. the absolute decays per second yields an efficiency of detection at each of these energies. A plot of these efficiencies is fitted with a polynomial to know the efficiency at any given energy in the available energy range.

The sources were placed on the beam line at the DSSD position at atmospheric pressure for the calibration runs. The calibration spectra as shown in Fig. 3.2 and were acquired for each detector in SeGA. All the peaks listed in the Table 1.18 were fit with a Gaussian function. The resulting centroids were then fit with a linear function to obtain the energy-calibration parameters.

For the absolute-efficiency calibration, the count rate of each detector in the SeGA was normalized to the known activity of each isotope in the SRM.

Isotope	γ-Energy (keV)	Measured Emission Rate (γ s^{-1}) October 29,2017	Absolute efficiency (%)
^{154}Eu	123.1	3.460 $\times 10^4$	22.79
^{154}Eu	247.7	5.864 $\times 10^3$	17.18
^{154}Eu	591.8	4.197 $\times 10^3$	9.22
^{154}Eu	723.3	1.703 $\times 10^4$	7.96
^{154}Eu	873.2	1.034 $\times 10^4$	6.86
^{154}Eu	996.3	8.850 $\times 10^3$	6.74
^{154}Eu	1004.7	1.534 $\times 10^4$	6.99
^{154}Eu	1274.5	2.958 $\times 10^4$	5.68

Table 3.2: Measured emission rates of SRM and calculated absolute efficiency of SeGA

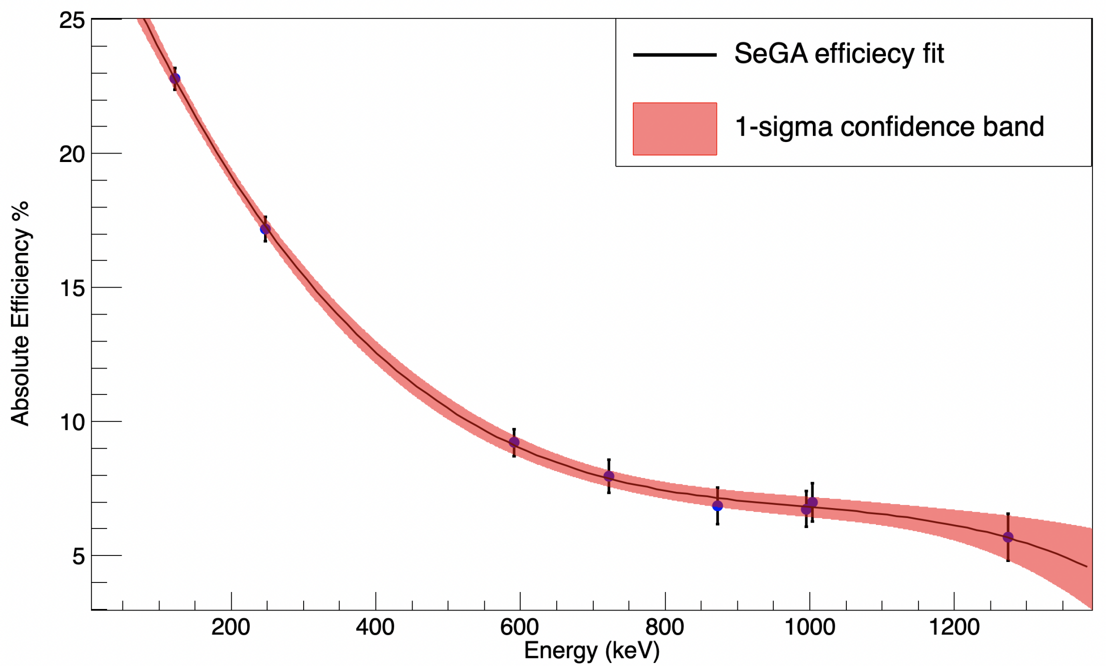

Figure 3.1: Absolute efficiency curve for SeGA. Calculated efficiencies for energies up to to 1274.5 keV were fit (black line) with third order polynomial. The red band correspond to the one σ (68%) confidence band.

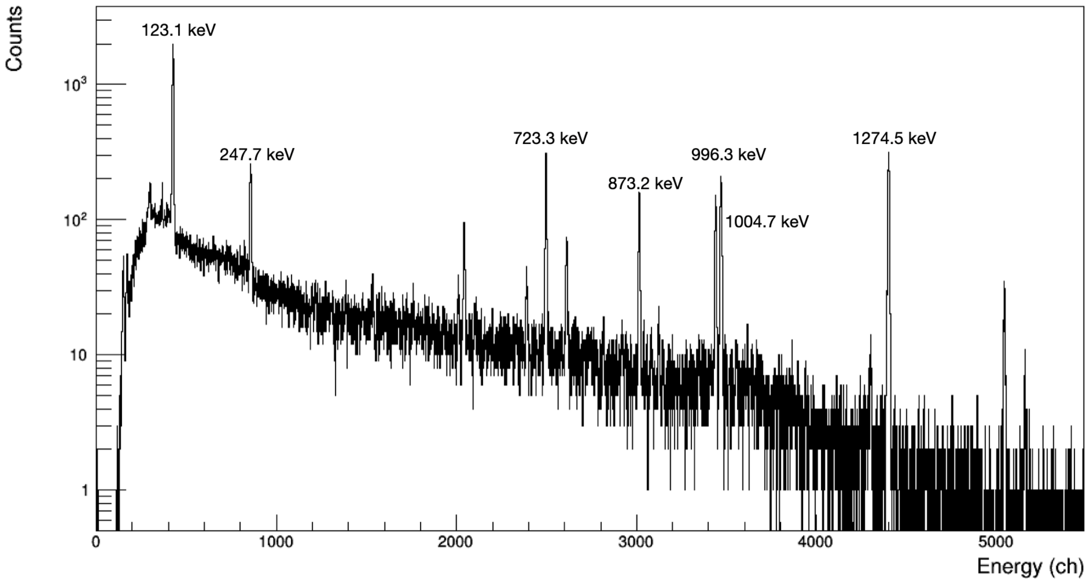

Figure 3.2: γ-spectrum of a single detector of SeGA. Calibrations were performed using a SRM [34]. The labeled γ-rays from ^{154}Eu were used for energy and efficiency calibration.

3.1.2 DSSSD calibration

The DSSSD and electronics must also be calibrated to measure the energy of light charged particles such as protons and β-particles. Two standard α-sources(^{148}Gd, ^{228}Th) were used for calibration as shown in Table 3.3. The ^{148}Gd source decays only by emitting a low-energy alpha of 3.18-MeV. In ^{228}Th source, alphas are emitted from many daughters as labeled in Fig. 3.3 in the Th decay chain. All of these alphas are above 5-MeV, therefore having ^{148}Gd low-energy alpha peak at 3.18-MeV strongly constrained the calibration for low energies. For all front and back strips, 80 spectra were acquired. The peaks labeled in Fig. 3.3 were fit with a Gaussian function, and the resulting centroids were fit with a linear function. The energy assigned to the peaks was used a dead-layer correction assuming a 0.1-nm Al dead-layer. The resulting gradient and intercept of the linear fits were then used for strip calibrations.

Parent	Half-life	α-Energy (MeV)	α-branching ratio
^{148}Gd	71.7 y	3.18	1
^{228}Th	1.91 y	5.34	0.27
^{224}Ra	3.62 d	5.68	0.95
^{220}Rn	55.6 s	6.23	0.99
^{216}Po	0.15 s	6.78	1
^{212}Po	0.3 μs	8.76	0.64

Table 3.3: Prominent α-energies and branching ratios of the sources (^{148}Gd, ^{228}Th) used for DSSSD calibrations.

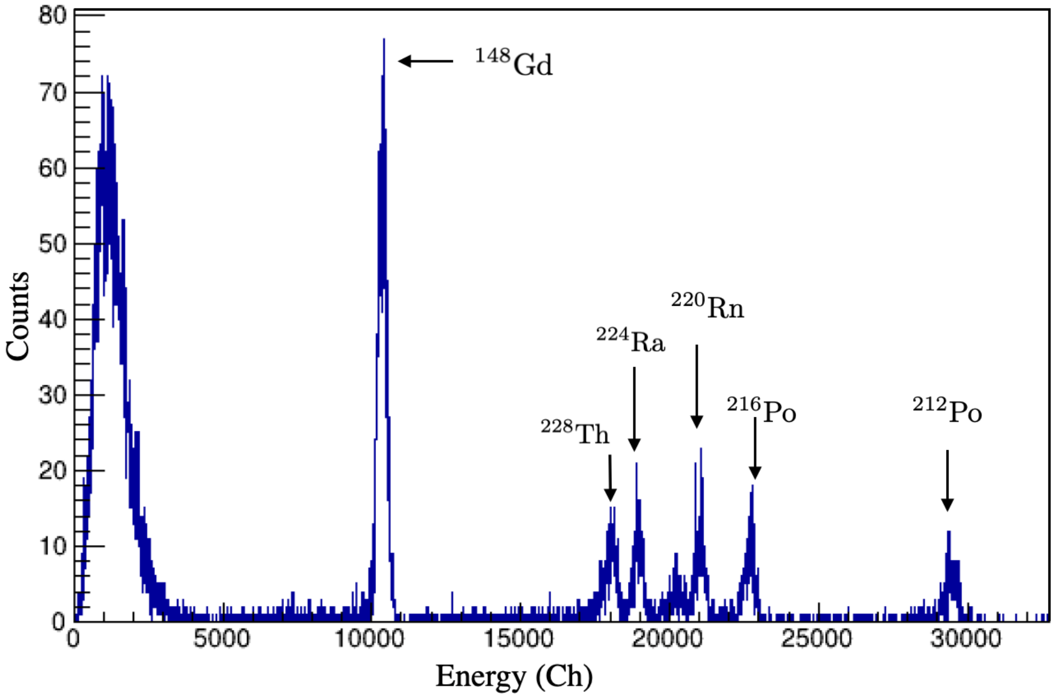

Figure 3.3: An energy calibration spectrum for sigle strip of DSSSD. Calibration was performed using ^{148}Gd and ^{228}Th α-sources. The ^{148}Gd peak and some ^{228}Th calibration peaks are labeled.

3.2 Particle Identification

Even though the goal of the experiment was to study a single exotic nucleus, it is generally not feasible to produce a completely pure beam in projectile fragmentation. This is particularly true for neutron-deficient nuclei. After being purified by the A1900 fragment separator and the RFFS, a mixture of fully stripped (ionized) exotic nuclei still remain in the beam composition. In order to perform β-decay studies, each incoming nucleus must be identified. Event-by-event Particle Identification (PID) and RFFS filtering turn the disadvantage of having a cocktail beam, to an advantage by allowing the study of multiple nuclei at the same time.

Each implanted nucleus was identified, based on their measured energy loss (ΔE) and Time-Of-Flight (TOF)[13]. The ΔE measurement was taken from the first silicon PIN detector in the BCS. The kinetic energy was determined by the TOF of the ion which is related to the velocity of the ion. Since the ions have energies around 10 GeV, the change in velocity due to insertion of materials (plastic scintillator detector, degrader wedges) is negligible [43]. Therefore, TOF information was determined from the time difference between start signal provided by PIN2 and a stop signal given by the scintillator located in the focal plane (FP) of A1900, with an added constant delay (Typically, the timing signal would have been taken from PIN1, however, the timing circuit for this detector malfunctioned and it was decided to use PIN2 instead). Individual isotopes can be observed clustered together in Fig. 3.4.

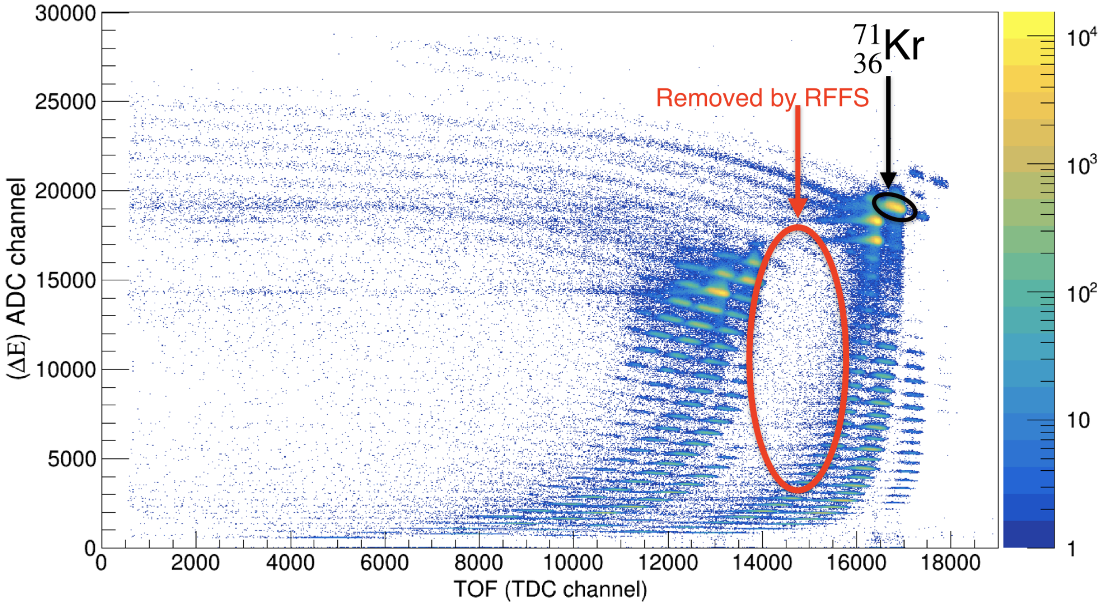

Figure 3.4: Particle identification plot of all implanted ions in the ^{73}Sr setting with RFFS. The PID plot shows PIN1 (ΔE) measurement versus the TOF measured between PIN2 and Focal Plane Scintillator. The colour scale represents the number of counts.

3.2.1 Filters used for Improving/Cleaning PID

In Fig. 3.4 some of the clusters are not well separated and streaks bleed into some of the clusters. In order to perform a cleaner isotope identification more layers of purification are required.

Due to the fact that the energy loss detector was not used as the TOF start detector, and thus there is some material between them, the process of particle identification became more complicated. To improve the identification, all the isotopes that did not get good implantation signal (ions lost in between PIN2 and DSSSD as well as the ions detected in the edge strips) were vetoed from the PID . Figure 3.5 shows the resulting PID, and confirms that the beam was spread out in between PIN2 and DSSSD, which was done to reduce pileup of ions in specific pixels. Due to this, some of the isotopes were not able to make it to the DSSSD or landed in edge strips.

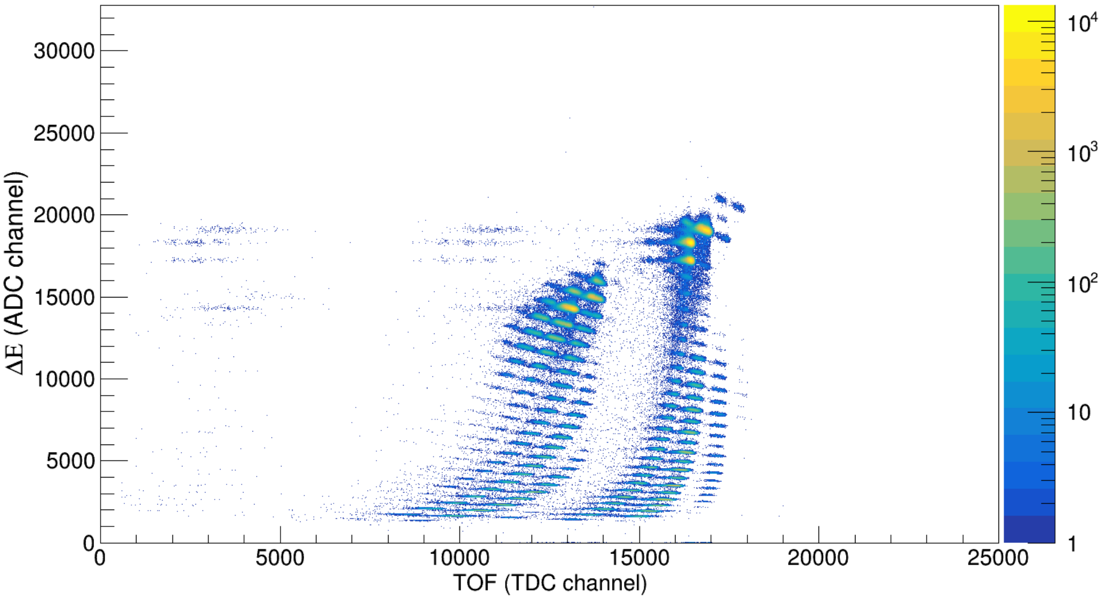

Figure 3.5: Particle identification plot of all implanted ions in the ^{73}Sr setting with RFFS. The PID plot shows PIN1 (ΔE) measurement versus the TOF measured between PIN2 and Focal Plane scintillator. The colour scale represents the number of counts. Ions implanted on edge strips were filtered.

The PID was confirmed by the identification of ^{71}Kr by its known characteristic γ-rays and half-life. Relative to the position of the ^{71}Kr isotope on the PID plot, the locations of other isotopes were determined as shown in Fig. 3.6. Isotopes are located in diagonals shown in red.

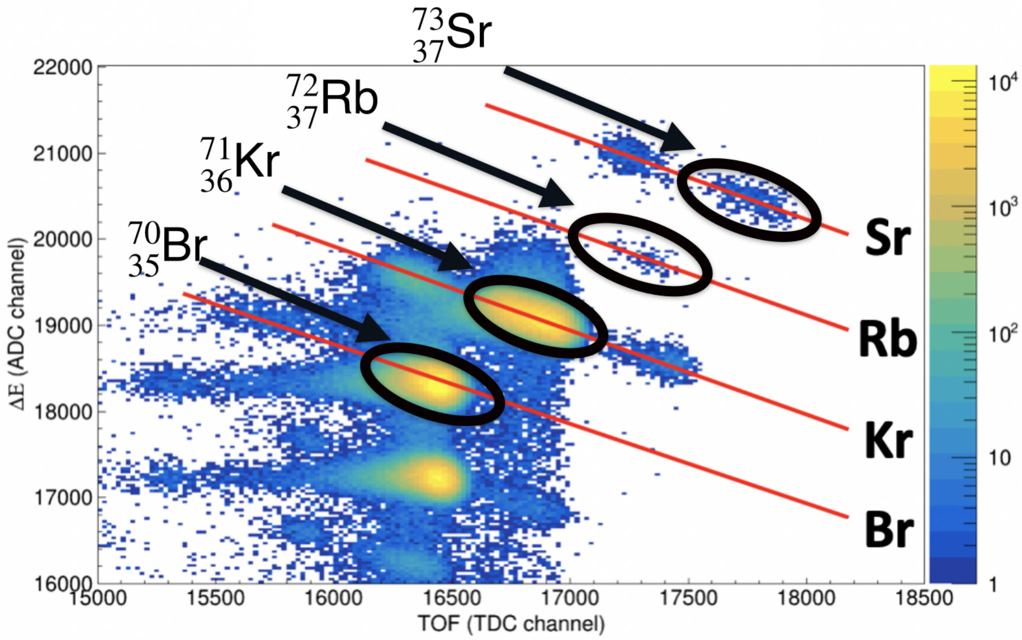

Figure 3.6: Similar to Fig.3.5 with expanded scales. Red lines represent the isotopes and ovals represent the ions of interest.

3.3 Implant-decay event correlations

For the offline analysis, once the ions of interest were implanted on the DSSSD, after being tagged by the energy-loss and time-of-flight measurements, the subsequent decay events were then used as the trigger. Following a trigger, a 5-μs gate was used to determine prompt coincidences. Furthermore, time and spacial correlations were performed to correlate an implant to a decay. The following sub sections will explain the logic used for assignment of ”implant” and ”decay” and how the time and spacial correlations were done.

During an implantation event, when an ion is stopped, several orders of GeV of energy is deposited into the DSSSD. This energy deposition can be distributed over several front and back strips. These implantation events generate a significant number of electron-hole pairs in the detector, and consequently the implantation signal does not require as much amplification as compared to the decay signal. Therefore, to cover the full energy range in the DSSSD, dual-gain pre-amplifiers were used that contained a low-gain stage for the implantation signals and a high-gain stage for the lower-energy decay signals.

An implantation event is initially defined if a low-gain pre-amplifier output in both front and back DSSSD channels were recorded coincident with a PIN1 trigger. The strips with the largest charge deposited from the front and the back channels were then assigned as the implantation pixel. On the other hand, decay events generate a significantly lower amount of energy, on the order of MeV or less. For these signals a larger amplification factor is needed and therefore a high-gain pre-amplifier stage is used for decay events. A high-gain pre-amplifier output in both front and back channels with no PIN1 signal is defined as a decay event. A decay event could be either a β or a proton.

Additional conditions must be satisfied in the process of constructing correlations of the implanted ions and their subsequent decays. For the analysis that follows, all decay events that follow an implantation within a correlation time window of 5-s are correlated. This allows for a good determination of the background [11],[41]. In order to reduce background events in the charged-particle spectrum, an additional time gate is applied. Correlated decay events are required to occur within a 1-s (about 10 times longer than the expected half-life) time window following an implantation and the decay is required to occur within the same pixel of implantation or the 24 nearest-neighbour pixels as shown in Fig. 3.7. Apart from the time and spatial correlation, the energy recorded in both front and back strips of any high-gain (decay) signal is required to be greater than 100 keV. The front side of the DSSSD was used for energy information due to the slightly better signal-to-noise ratio it provided relative to the back side of the DSSSD.

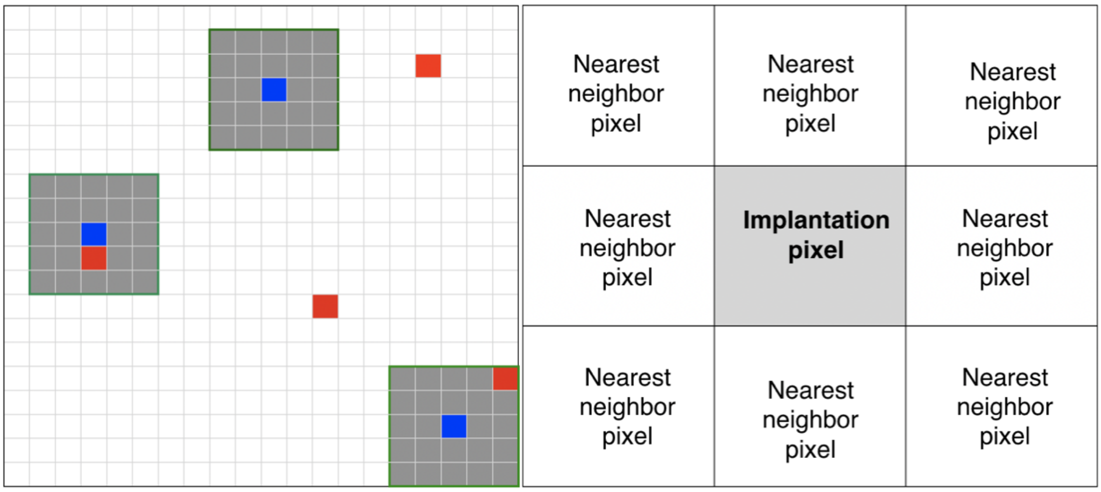

Figure 3.7: The first Schematic represents the 24-pixel correlation geometry (gray) used for correlating implantation (blue) and decay (red) events in this work. The second schematic represents 8-nearest-neighbour pixels that were looked for decay events within a fixed time to pair to the implantation.

Since heavy ions are continuously being implanted at a rate of ∼6 Hz, with ^{71}Kr implants accounting for a large fraction of the rate, multiple ^{71}Kr ions will be observed at the same time in different pixels of the DSSSD as shown in Fig. 3.7. In such instances, time correlations are preformed separately for each of those implantation events. However, if a second implantation supersedes an ongoing correlation, both implantations will be correlated with the decays. Therefore, in the time spectra, wrongly correlated decay events form a constant background, whereas decay events, which belong to the implantation event considered, form the exponential decay curve as shown in Fig. 3.8.

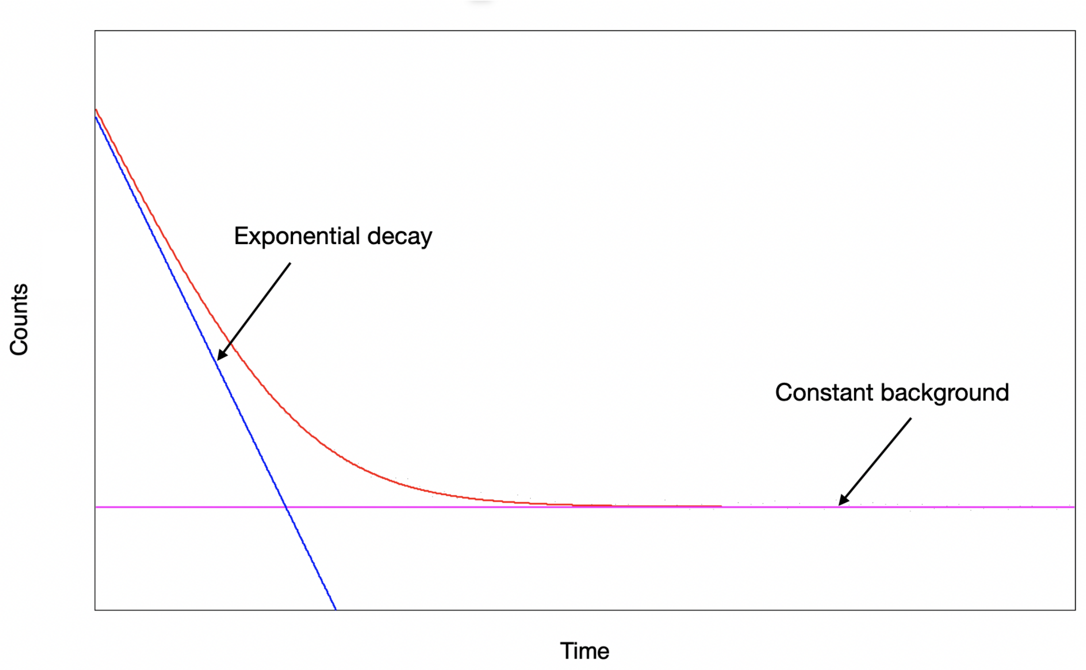

Figure 3.8: Schematic diagram of the implant-decay correlation time spectrum. Blue coloured curve represents the exponential decay of the parent and uncorrelated decays form the constant background shown in magenta. Red coloured curve represents the summation of two functions.

β particles often deposit energy in several neighbouring strips due to the relatively small amount material (silicon) of the DSSSD. For some β events the charge is deposited within several strips. In such cases the strip with the highest energy deposition is chosen to determine the energy and the pixel. To construct β-γ correlations the DSSSD decay signal is used as the offline trigger for SeGA so that only γ-rays in coincidence with charged-particle events are considered.

3.4 DSSSD trace (wave-form) analysis

In an effort to improve the offline analysis, traces of all of the DSSSD signals were also acquired. The recorded signal shows how the charge/voltage varies with the time when an interaction occurs in the detector. By analysing a trace the energy and time of a particular interaction can be obtained. Furthermore, in some detectors, the shape of the waveform can be used to identify the type of interaction (e.g. neutron or gamma), although such a distinction was not possible with this setup.

The charged particle energy was calculated by the Analog-to-Digital Conversion (ADC) value given by the digitizer, which was extracted by a trapezoidal filter [20]. For the trace analysis, a Charge-to-Digital Conversion (QDC) was calculated manually by integrating the full trace after a baseline correction, taken from an average of the first 5% of the waveform. To investigate any discrepancies between the ADC value reported by the digitizer, the calculated QDC value from the trace was plotted with respect to the calibrated digitizer ADC shown in Fig. 3.9. The true events with properly measured energy can be seen as a rectangular intense grouping intersecting zero, labeled as 1 as shown in Fig. 3.10.

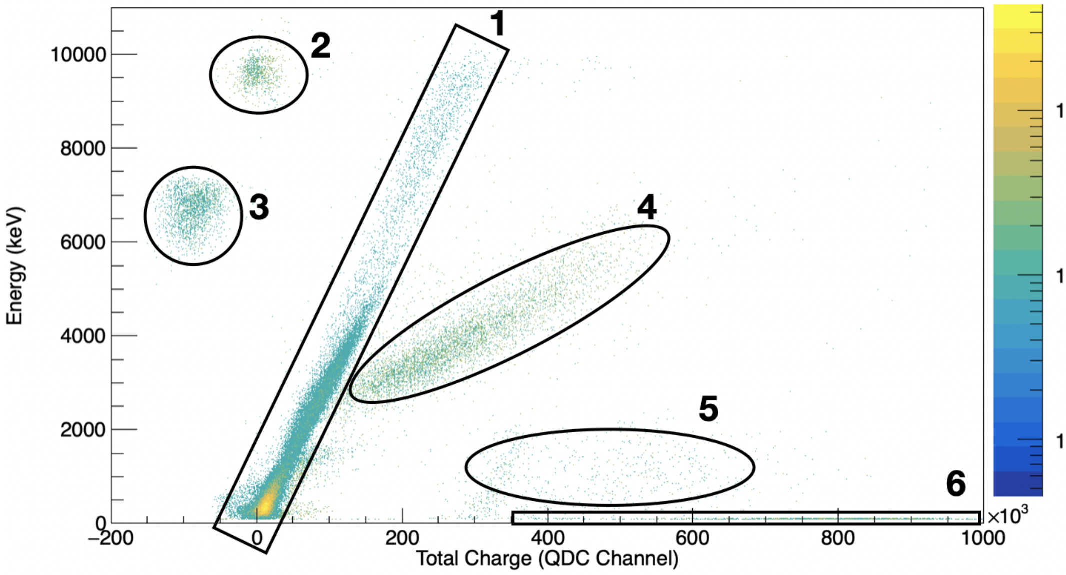

Figure 3.9: Plot of the DSSSD front event energy reported from the trapezoidal filter of the XIA Pixie-16 digitizer versus the total charge calculated from a trace analysis on potential decay events in the DSSSD occurring 5-s after implantation of ^{71}Kr. The traces were baseline corrected, and then the total charge was found by summing the entire trace. Different regions from 1 to 6 are labeled. Representative trace in each labeled group is shown in the Fig.3.10.

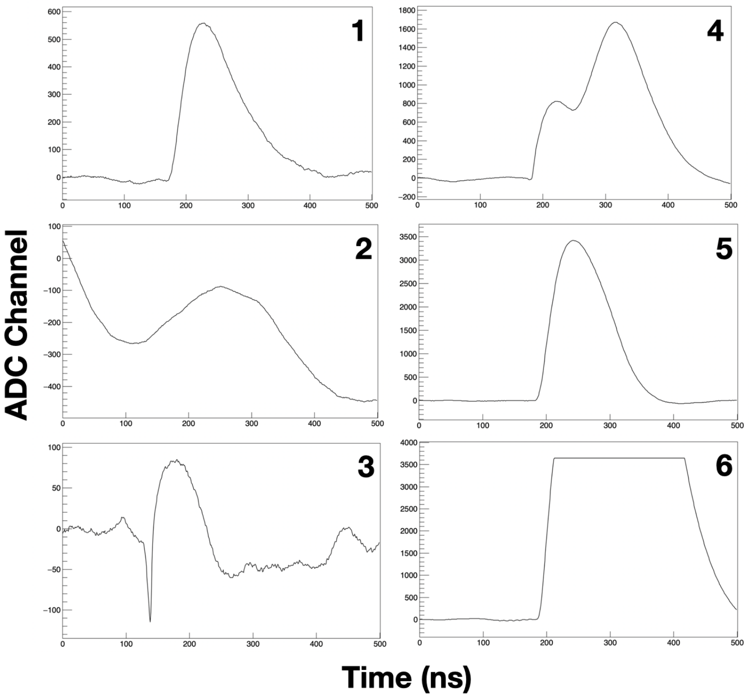

Figure 3.10: Trace representative of each labeled group in the Fig.3.9.

In order to understand other groupings (2 to 6) shown in Fig. 3.10, the sample traces were also analyzed. The group 2 found to be a result of fluctuations in the baseline, or very-low energy charged-particle events. Events in the first group appears to be the negative ADC channels reported after the baseline correction suggests that these are a re-trigger of the data acquisition. In both cases events can be explained as underflow from a 15-bit unsigned integer. The region 4 appears to be pile-up events in the detector. Furthermore, the feature seen in the energy range of 2.5 MeV to 6.5 MeV and it is observed from almost all of the strips.

Another consquence of storing the values as an unsigned short is that there is a maximum positive value that can be stored. If the ADC value is greater than this maximum it will wrap around to a smaller value. The events in grouping 5 show this issue. Furthermore, If the digitizer is saturated by a particular signal it is flagged and stored as zero which explains the events in grouping 6. In order to improve the charged particle energy spectrum a trace filter was applied in the sorting process of decay events. This trace filter cleaned the charged-particle energy spectrum significantly resulting in a lower overall uncorrelated background.

3.5 Decay-curve fitting methods

In order to determine the half-life of a particular β-decay, the time distribution between the implantation of an ion and its subsequent β-decay was analyzed by constructing the time distribution between an implantation and any potential β-decay events.

To extract the half-life, a χ^2 minimization procedure was used to fit the decay curves utilizing two different fitting functions. The first method relied on the using bins with constant width, while the second method used the logarithmic binning method as described by Schmidt [40], and will be referred in the text as the Schmidt method. Both of these methods follow from the Bateman equations for radioactive decay, detailed below.

3.5.1 Radioactive decay and Bateman equations

Consider a β-decay, where a parent nucleus disintegrates into a daughter nucleus. For a given radioactive sample of material, the β-decay rate given by the change in the number, N, of parent nuclei into daughter nuclei ($-dN/dt$). This rate of change of a sample is defined as the activity, A, which is equal to the product of the decay constant, λ, and the number of parent nuclei at a given time,

$$A = -\frac{dN}{dt} = N\lambda \tag{3.1}$$

Integration of Eqn. 3.1 with the boundary conditions that $N = N_0$ at $t = 0$ yields Eqn. 3.2, where t is time, N_0 is the number of parent nuclei at time zero and N_t is the number of parent

$$^{71}\mathrm{Kr} \rightarrow ^{71}\mathrm{Br} \rightarrow ^{71}\mathrm{Se} \rightarrow ^{71}\mathrm{As} \rightarrow ^{71}\mathrm{Ge} \rightarrow ^{71}\mathrm{Ga}$$

$$100ms \rightarrow 21.4s \rightarrow 4.74m \rightarrow 65h \rightarrow 11d \rightarrow \text{stable}$$

Figure 3.11: The β-decay chain of ^{71}Kr. The half-life of parent and daughter nuclei are noted [36][16][2][46][31].

nuclei at time t,

$$N(t) = N_0 e^{-\lambda t} \tag{3.2}$$

The half-life of a nucleus the amount of time needed for a given number of parent nuclei to decrease by one half of its initial amount. Half-life is then defined as,

$$t_{1/2} = \frac{\ln 2}{\lambda} \tag{3.3}$$

Half-lives of nuclei span many orders of magnitude. ^{71}Kr is located far from stability and has a relatively short half-life of ~100 ms. Therefore, this nucleus will be the parent of a decay chain which consists of the buildup and decay of several longer-lived isotopes until stability is reached as shown in Fig. 3.11.

To construct a decay curve one must consider the probability that the time distribution of the β-decay has contributions from the parent nuclei, and also the daughter and the subsequent grand-daughter decays. The Bateman equation [3] is a mathematical model describing abundances and activities in a decay chain as a function of time, based on the decay rates and initial abundances. The general solution describes the number of nuclei of the nth isotope, N$_n$(t), with decay constant, λ_n, at a time, t, involved in a decay chain with the following formula [24]:

$$N_n(t) = \prod_{j=1}^{n-1} \lambda_j \sum_{i=1}^{n} \sum_{j=1}^{n} \left(\frac{N_i(0) e^{-\lambda_j t}}{\pi^n_{p=i,p\neq j}(\lambda_p - \lambda_j)} \right), \tag{3.4}$$

where λ_j is the decay constant of the j^{th} precursor.

In this work only the parent decay is considered, so the expansion of the equation3.4 for $i = 1$ with a constant background term can be written as:

$$N_1(t) = \lambda_1 n_1(0) e^{-\lambda_1 t} + C_{bg} \tag{3.5}$$

3.5.2 Log-bin decay curve - Schmidt method

Logarithmic decay-time distributions can be also be used to extract the half-life of a radioactive species in a similar manner as linear decay-time distributions. This is an alternative method to the typical exponential fit particularly for cases of low statistics [40]. Additionally, it gives information about the number of radioactive species present, which is non-trivial to determine by using standard linear decay-time distribution.

The number of radioactive decay events is plotted against the natural logarithm of the time difference between ion implantation and β-particle detection, and note that the bin sizes are constant in the logarithmic transformation. The β- decay half-life can then be extracted from the centroid of the bell-shaped time distribution as shown in Fig. 3.12. Instead of plotting a linear ΔT, the natural logarithm, lnΔT can be considered. For a radioactive decay, the linear decay time frequency distribution is given by:

$$\left|\frac{dn}{dt}\right| = \lambda n_0 \exp(-\lambda t) \tag{3.6}$$

In the Schmidt method the logarithmic decay time distribution is used by transforming to a logarithmic basis:

$$\left|\frac{dn}{d\ln(t)}\right| = n_0 \exp(\ln(t) + \ln\lambda)\exp(-\exp(\ln(t) + ln\lambda)) \tag{3.7}$$

Fitting Equation 3.7 to the logarithmic-decay-time distribution results in a curve such as that shown in Fig. 3.12.

$$|\frac{d^2 n}{d^2\ln(t)}| = 0 \rightarrow \ln(t)_{max} = \ln(\frac{1}{\lambda}) \tag{3.8}$$

3.5.3 χ^2 minimisation fittings

In both methods of fitting the decay-curves mentioned in the previous sections, the half-life is found by minimizing the χ^2 while the parameters of the fitting function are changed.The total decay spectrum as a function of decay time, t, (Eqn. 3.5) is denoted as $f(t_i)$. In particular, the χ^2-fitting procedure tries to minimise:

$$\chi^2 = \sum_{i=1}^{N}[\frac{N(t_i) - f(t_i)}{\sigma_i}]^2 \tag{3.9}$$

in which the index, N, is the total bin number in the time histogram. t_i and $N(t_i$ are the central time and number of counts in the i-th bin, respectively, and σ_i is the statistical uncertainty in the i-th bin obtained from the number of counts as:

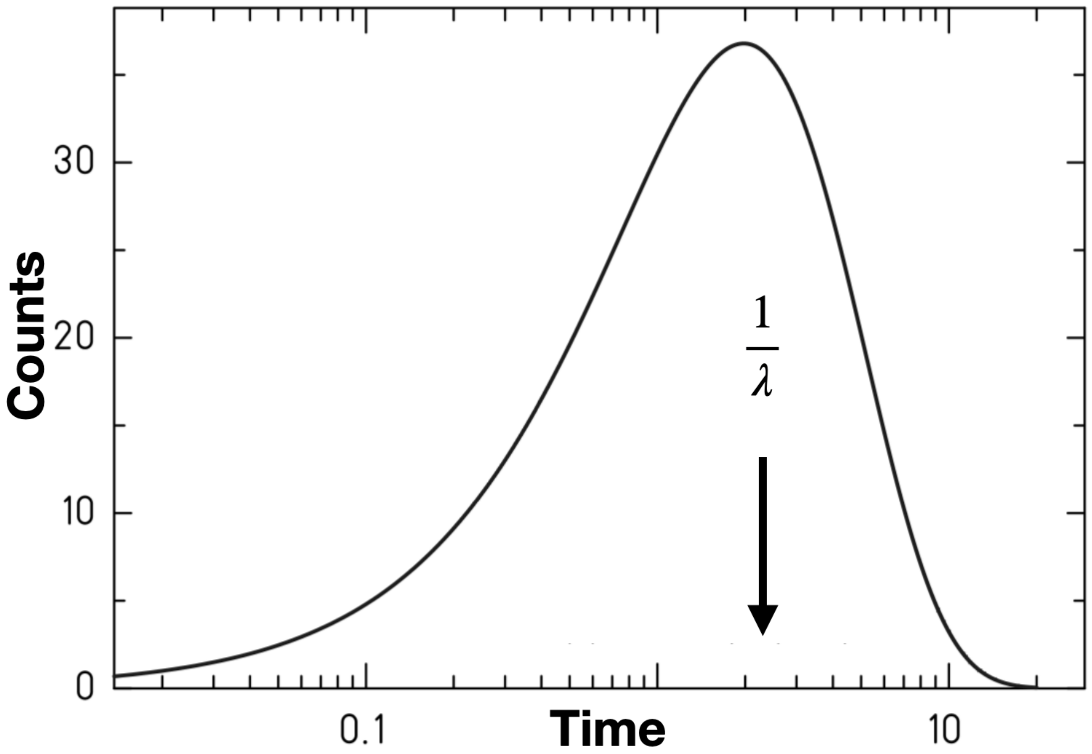

Figure 3.12: The number of counts is plotted against the natural logarithm of the time distribution, t. This gives rise to an asymmetric bell shaped curve. The peak in the distribution corresponds to the half-life of the nuclide. Figure adapted from [40].

$$\sigma_i = \sqrt{N(t_i)} \tag{3.10}$$

The three free fitting parameters in the Eqn. 3.5 are the decay constant of the parent nucleus λ_1, the initial abundance $n_1(0)$, and a constant background C_{bg}. The χ^2_{reduced} value is quoted with the fittings reported in ^{71}Kr decay-spectroscopy results.

$$\chi^2_{\text{reduced}} = \frac{\chi^2}{\text{N-3}} \tag{3.11}$$

4 ^{71}KR DECAY-SPECTROSCOPY RESULTS

To investigate mirror symmetry and nuclear structure along the $N = Z$ line, ^{71}Kr nuclei produced in the projectile fragmentation experiment were studied using charged-particle and γ spectroscopy. The method used to transform raw data into correlated physically meaningful data, as well as the statistical methods employed in this work, were discussed in detail in Chapter 3. Additional details of the analysis used to obtain β-decay half-lives, β-delayed proton spectra, as well as $\beta\gamma$ and βp branching ratios are discussed in this chapter. Finally, the decay scheme deduced based on those results is presented, including a newly observed β-decay channel and a delayed-proton channel. The effect of the new observations, specifically the β-delayed proton channel will be useful in constraining the ground-state spin of ^{71}Kr.

4.1 Decay curve analysis

Given the minimal amount of previous β-decay measurements of ^{71}Kr, one of the goals of the analysis was to precisely measure the half-life. During the experiment, each implantation and decay event as well as every γ-ray was tagged with a 10 ns timestamp. Thus, the decay time for an individual ion was measured by subtracting the time of a localized charged-particle event from the time of the implantation event. Following the identification an isotope, the time distribution between the implantation of an ion and its subsequent β-decays were histogramed and fit with a decay curve to determine the half-life. As described in Chapter 3, β-particle position and time correlations were performed. Two methods were used to determine the β-decay half-live of the ground state of ^{71}Kr as previously discussed in Chapter 3.

It should be noted that for daughter nuclei whose half-lives were several orders of magnitude longer than the parent half-life (i.e. milliseconds for the parent and seconds for the daughter), the daughter was neglected in the fitting procedure. These decay components will not contribute significantly to the half-life determination of the parent.

4.1.1 Background treatment

In this experiment, the assumption of an isolated parent population in the implantation detector does not hold as there is a buildup of activity due to the other ions in the secondary-beam cocktail, creating an uncorrelated background that can be seen in Fig. 3.8. Therefore it is necessary to add a constant background term to the exponential decay of the parent.

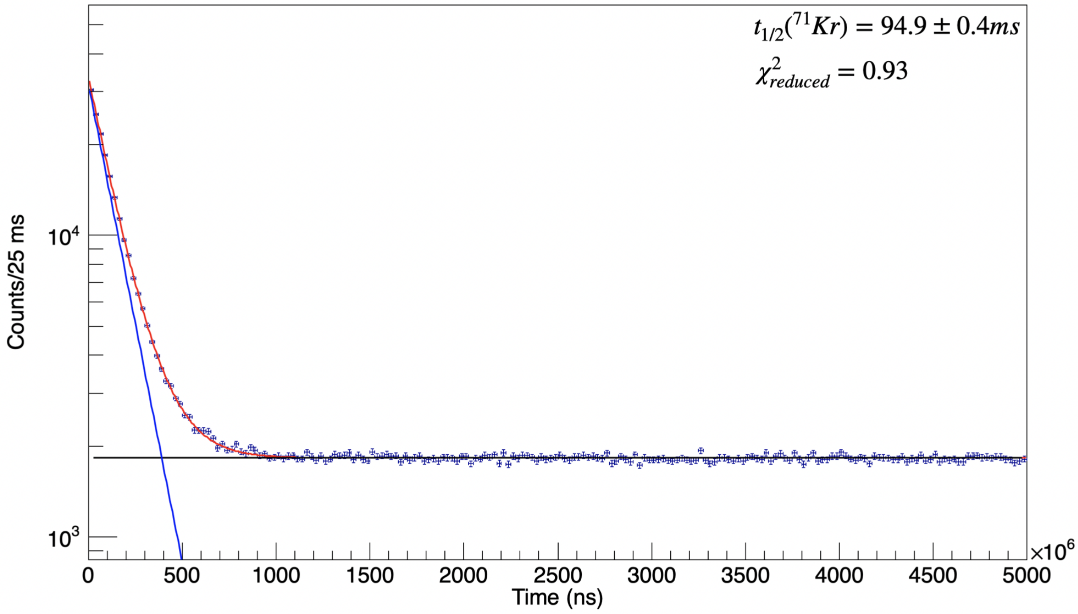

Figure 4.1: The time distribution of the decay events following the identification of ^{71}Kr nuclei. A decay time fitted with an exponential decay (blue) and a constant background (black) resulting in the combined fit (red). The half-life extracted for ^{71}Kr = 94.9 ± 0.4 ms.

4.1.2 Linear-bin decay curve

The decay curve for β or β-proton events correlated with the decay of ^{71}Kr is shown in Fig. 4.1. Again, for a potential decay event to be considered it is required that the event occurred within a time window of 5 s and in the same pixel or surrounding 24-pixels of the pixel determined for ^{71}Kr implantation. Both the β-decay daughter (^{71}Br) and proton-decay daughter (^{70}Se) have half-lives significantly longer than our correlation window of 5 s. Consequently, both ^{71}Br and ^{70}Se, whose β-decay half-lives are known to be 21.4±0.6 s [16] and 41.1±0.3 min [45], were neglected as they are expected not contribute significantly to extracting the half-life of the parent. A constant background (black) together with an exponential function was fit to the data, and this yielded the combined fit (red) resulting in a β-decay half-life of 94.9±0.4 ms for ^{71}Kr.

4.1.3 Log-bin decay curve

As described in Chapter 3, the half-life can also be extracted using a logarithmic time bin decay method [40]. The decay time of β or β-proton events correlated with the implantation of ^{71}Kr are histogramed in logarithmically increasing time bins as shown in Fig. 4.2. In this log-bin decay curve, a bell-shaped asymmetric distribution and an exponentially increasing distribution can be observed. The bell-shaped asymmetric distribution suggests only one radioactive species is decaying in the considered correlation time window since the peak position of the distribution is related to the half-life of the species and only one well-defined peak is observed. The uncorrelated

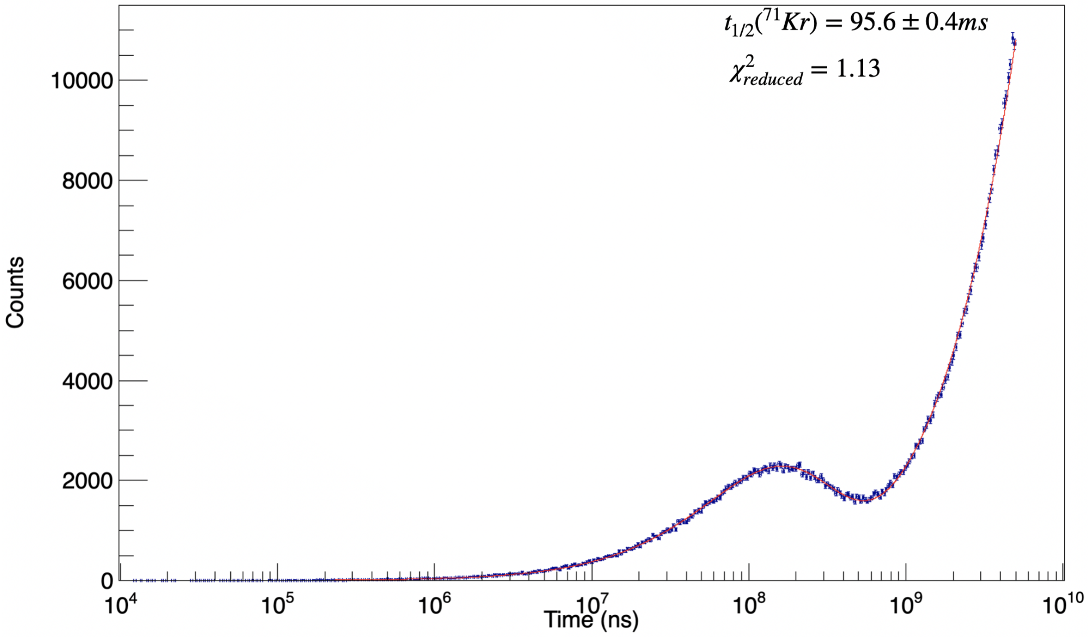

Figure 4.2: The number of radioactive decay events is plotted against the natural logarithm of the time difference between ^{71}Kr implantation and the subsequent β-decay event. The half-life extracted for ^{71}Kr = 95.6 ± 0.4 ms using Schmidt method [40].

events form an exponentially increasing background starting approximately from 1 s, as observed in Fig. 4.2, since the size of each successive bin is exponentially increasing. The decay constant was determined by fitting the curve using Eqn. 3.7, yielding a half-life for ^{71}Kr of 95.6±0.4 ms.

The half-life values obtained from two different methods are in good agreement with each other. However, the χ^2_{reduced} for the linear-bin method is slightly less than 1, which suggests the model used for the fit is over-fitting the data. Therefore, the half-life value of ^{71}Kr used for this work was taken from the log-bin method as it reports a χ^2_{reduced} value greater than 1.

The half-life found for ^{71}Kr is within 2σ of the errors reported in the previous measurement by Oinonen et al. [36] which found $t_{1/2}$= 100 ± 3 ms, although it is in very good agreement with the half-life (95 ± 6 ms) found by gating on the β-delayed protons in that work. The deviation can largely be attributed to low statistics as the previously analysis was based on about 1000 ^{71}Kr implanted ions. The half-life in this work is based on 698955 ^{71}Kr implantations. A comparison with the previously measured values by Oinonen et al. is shown in Table 4.1.

4.2 γ-ray and charged-particle spectroscopy

β-gated γ-ray energy spectra were created in order to search for γ-decays following the β-decay of ^{71}Kr. The information revealed can be used to understand the excited energy-states that are fed by β and β-delayed proton emission, thus providing insight into the level structure of the respective daughter nuclei. After each charged-particle decay trigger, a 5-μs prompt window is

Reference	Half-life (ms)	Method	χ^2_{reduced}
[36]	101 ± 4	High-energy β counting Linear-bin method	-
[36]	95 ± 6	β-delayed proton counting Linear-bin method	-
This study	94.9 ± 0.4	β and proton counting Linear-bin method	0.93
This study	95.6 ± 0.4	β and proton counting Log-bin method	1.13

Table 4.1: Comparison of β-decay half-lives obtained for ^{71}Kr in the present work with the literature values.

used for the HPGe detectors.

However, this experiment was performed with a constant beam rate without any "beam off" component. Therefore, the γ-ray energy spectrum also contains γ-rays from multiple sources including the original implanted nuclide, a different implantation event, from other nuclides different from the original implant, and background. In all cases, we have to remove these background γ-rays to obtain a γ-ray spectrum for a selected implanted species. This is done by means of using a time gate on the events. In the time spectrum, wrongly correlated decay events form a constant background, whereas decay events which belong to the implantation event considered, form an exponential decay curve. Therefore, we can divide the events into two parts (see Fig. 4.3): (i) the red coloured part, which contains the real correlations forming the exponential decay as well as the wrong correlations, which contribute to the constant background and (ii) the blue coloured part, which contains primarily wrong correlations, because this part starts after about ten half-lives.

γ-rays arising from the β-decay of ^{71}Kr within 0 s to 1 s of implantation are accumulated in the β-gated γ-ray energy spectrum, which is shown in Fig. 4.3 (a). γ-rays that are emitted within 1 to 5 s of implantation are accumulated in background spectrum as shown in Fig. 4.3 (b). The accumulated background spectrum was then scaled to correct for the difference in accumulation time and subtracted from the spectrum generated from 0 s to 1 s.

4.2.1 $\beta\gamma$ decay branch

The β-decay of ^{71}Kr feeds states in ^{71}Br from the ground state up through proton-unbound states. The states below the proton separation energy decay via γ de-excitation. Above the proton separation energy proton emission and γ-decay compete. Knowledge of the β-decay intensities are useful in understanding the spin and parity assignment of the ground state of parent nuclei if the spins of populated states in the daughter nucleus are known. Some states will be more favourable to β-decay, due to the similarity of initial and final state (overlapping) wave functions. Thus, a larger transition probability can be observed for the states with smaller

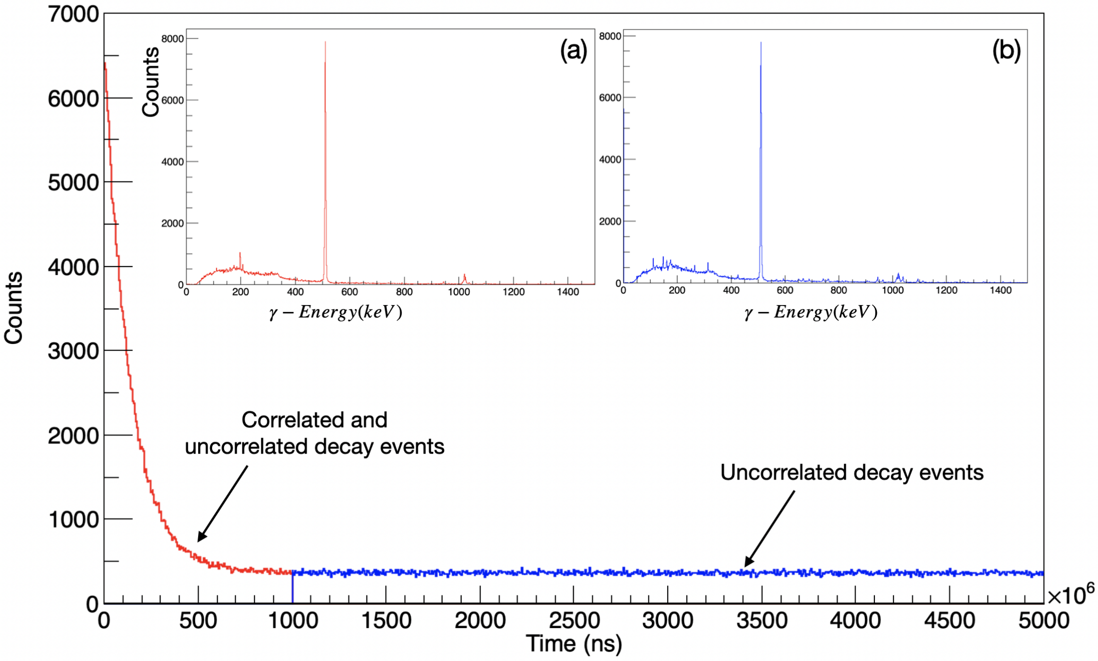

Figure 4.3: Representation of the background subtraction procedure used to analyse the data. This procedure correlates implantation events with all subsequent decay events with in the 24-strip tolerance for 5 s which is shown as red and blue combined decay curve. γ-ray energy spectrum of γ-rays detected within 1 s following the ^{71}Kr implantation is shown as (a). Time spectrum was used to remove wrong correlations by subtracting spectrum-(a) from γ-ray-energy spectrum (b) generated for events in the second part (blue part of the decay time spectrum) with correct scaling factors. This yields background corrected γ-ray-energy spectra for ^{71}Kr which is shown in Fig. 4.5. An equivalent procedure is used for the charged-particle spectrum.

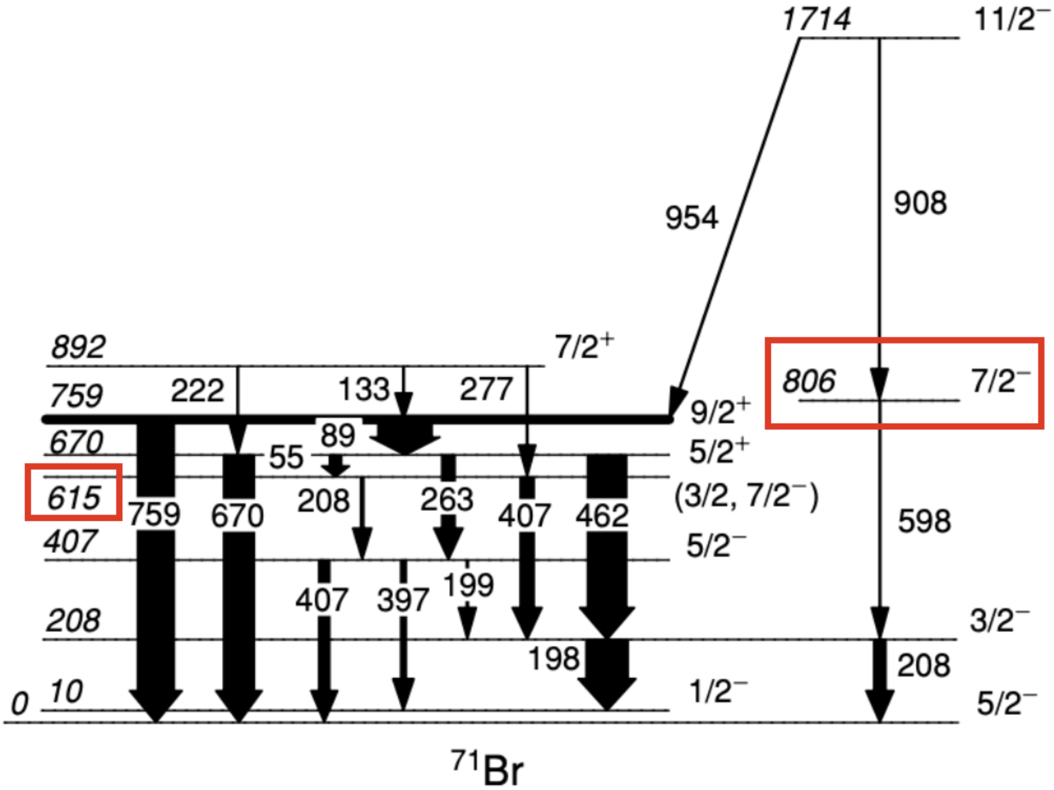

Figure 4.4: Decay scheme of low-lying states below $11/2^-$ state of ^{71}Br based on ^{71}Br de-excitation produced in the ^{40}Ca(^{40}Ca,2αp) fusion-evaporation reaction [14]. Some of the intense transitions such as 198, 207, 397 and 407 keV are observed in the measured γ-ray energy spectrum. The two energy levels labeled in red coloured rectangles have the potential to be fed by β-decay.

change in angular momentum. Furthermore, β-decay prefers a larger energy difference between initial and final states as a larger energy difference provides more phase-space. The intensity of each γ-ray (after efficiency correction) can then be used to estimate the β and γ-branching ratios as described in section 4.3.

According to the level scheme of ^{71}Br published by Fischer et al.[14], this nucleus has some very similar γ-ray transition energies as shown in Fig. 4.4. Specifically, the two different 198 and 199-keV transitions in the level scheme overlap in energy and are not resolvable as two peaks in the experiment described in this thesis given the resolution of the γ detectors used. Furthermore, the 208, 407 and 615-keV states decay via γ-ray transitions of similar energies (i.e. the 208-keV and 407-keV γ-rays) as shown in Fig. 4.4. Therefore, it was assumed that β feedings to proton bound states above 407-keV are negligible for the simplicity of the calculation process, as feeding to higher states should be smaller. Since β-decay prefers large phase-space, it will preferentially decay to the lowest allowed energy states. Thus, in this thesis γ-branching ratios were calculated based on that assumption.

For the current analysis, the background subtracted γ-ray spectrum in coincidence with ^{71}Kr

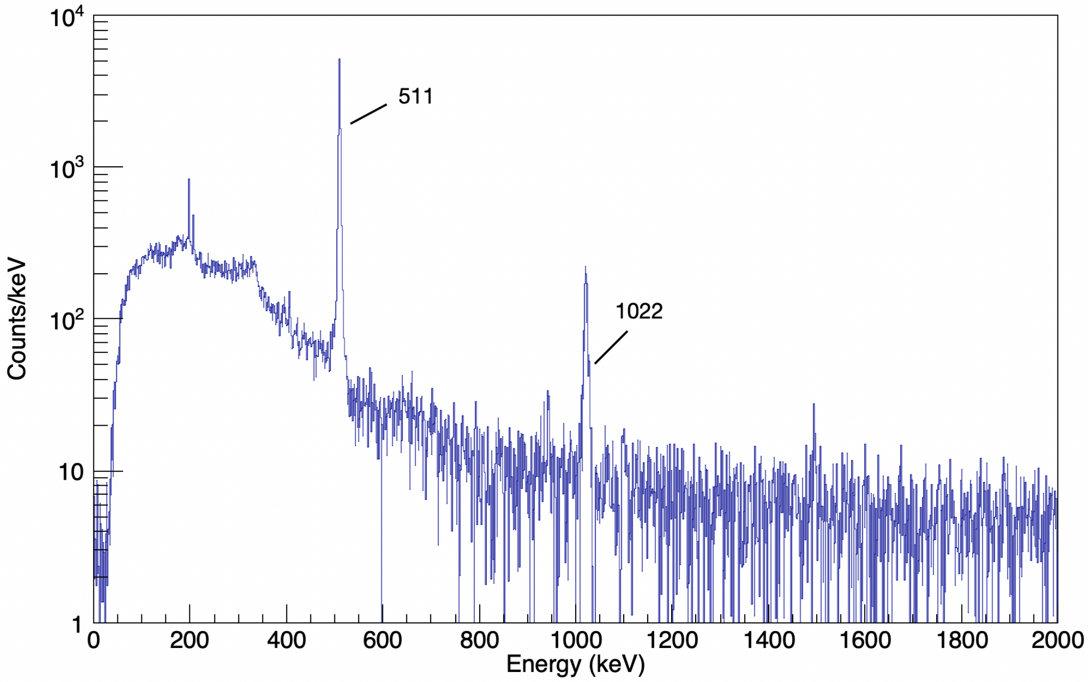

Figure 4.5: Background subtracted γ-ray energy spectrum of γ-rays correlated within 1 s of the β-decay of ^{71}Kr implantation. Peaks are observed at 511 keV (positron annihilation) and 1022 keV (511 keV summation).

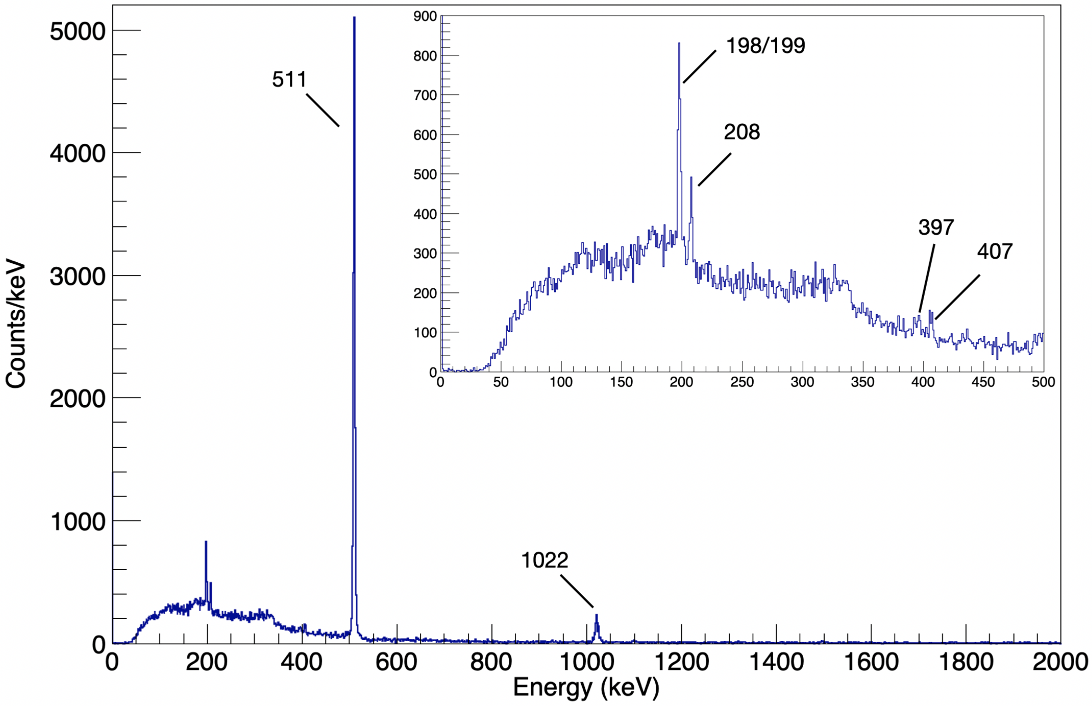

Figure 4.6: Background-subtracted γ-ray energy spectrum gated on charged-particle events below 1.5 MeV (β Energy gate), arising from the β-decay of ^{71}Kr correlated within 1 s of implantation, is shown. Peaks are observed at 511 keV (positron annihilation) and 1022 keV (511 keV summation). An expanded low-energy region is shown in the spectrum in the top right. Transitions corresponding to the de-excitation of ^{71}Br are observed at energies of 198/199, 207, 397 and 407-keV.

β-decay is shown in Fig. 4.5. The peak at 511 keV represents the energy of photons produced from positron annihilation. The second prominent peak at 1022 keV is due to summation of two 511 keV γ-rays within the Ge detectors. In order to have a closer look into the ^{71}Br de-excitation γ-rays, a β-energy gated γ-ray energy spectrum was made as shown in Fig. 4.6. It reveals four peaks related to the ^{71}Br daughter decay. Transitions are observed at energies of 198, 207, 397 and 407 keV while the spectrum is dominated by 511-keV and 1022-keV peaks.

The 198-keV peak is the most intense in Fig. 4.6. It is the sum of the intensities from the 198 and 199-keV transitions as the γ-ray detectors could not resolve these closely spaced energies. A gate on the 198/199-keV peak was made with a background subtracted $\gamma\gamma$ coincidence spectrum to determine the contribution to the 198-keV peak from the 199-keV transition as shown in Fig. 4.7. A peak at 198/199 keV is observed where this γ-ray corresponds to transitions from the 407-keV state to the 208-keV state. Interestingly, the weak accumulation of counts around 208-keV and 407-KeV energies are consistent with transitions from the 615-keV state. Furthermore, a gate on 208-keV was made on the background subtracted $\gamma\gamma$ coincidence spectrum as shown in Fig. 4.8. A peak at 198/199-keV is observed. Again, the 199-keV γ-ray corresponds to transitions from the 407-keV state to the 208-keV state. The accumulation of counts around 208-keV energy is again consistent with transitions from the 615-keV state which would be an indication of a branch to this level. However, any signs for the 407-keV transition are not observeable. Furthermore, a gate on 397-keV and 407-keV was made on the background subtracted $\gamma\gamma$ coincidence spectrum and added together (to improve the statistics) as shown in Fig. 4.9. But any signs of the 208-keV transition is not observed. According to these observations it is unclear if the 615-keV state is β fed or not. There could be a small branching, but in the analysis that follows it is assumed that feeding to the 615-keV state is negligible.

Next, in the β-gated γ-ray energy spectrum shown in Fig. 4.6, there is a prominent 208-keV γ-ray from the de-excitation of 208-keV state to the ground state. The 397-keV and 407-keV peaks can also be observed even though they are not as prominent as 198-keV, 208-keV peaks. The 397-keV peak is from the decay of the 407-keV level to first excited state at 10 keV. And the 407-KeV peak is from the decay of the 407-keV state to ground state.

To build the ^{71}Br de-excitation level scheme, the observation and interpretation of γ-rays in prompt coincidence with other γ-rays can be investigated. If γ-rays are emitted in a cascade and none of the involved states has a measurable lifetime, then those transitions can be observed in mutual prompt coincidence. The relative intensities of observed γ-rays were calculated as listed in Table 4.3 using β-gated γ-singles spectra and projections of β-gated $\gamma\gamma$-matrix assuming that no proton bound states above 407-keV were populated. The calculated values differ with those relative intensities derived in the modified β-decay scheme given in the in-beam study on ^{71}Br

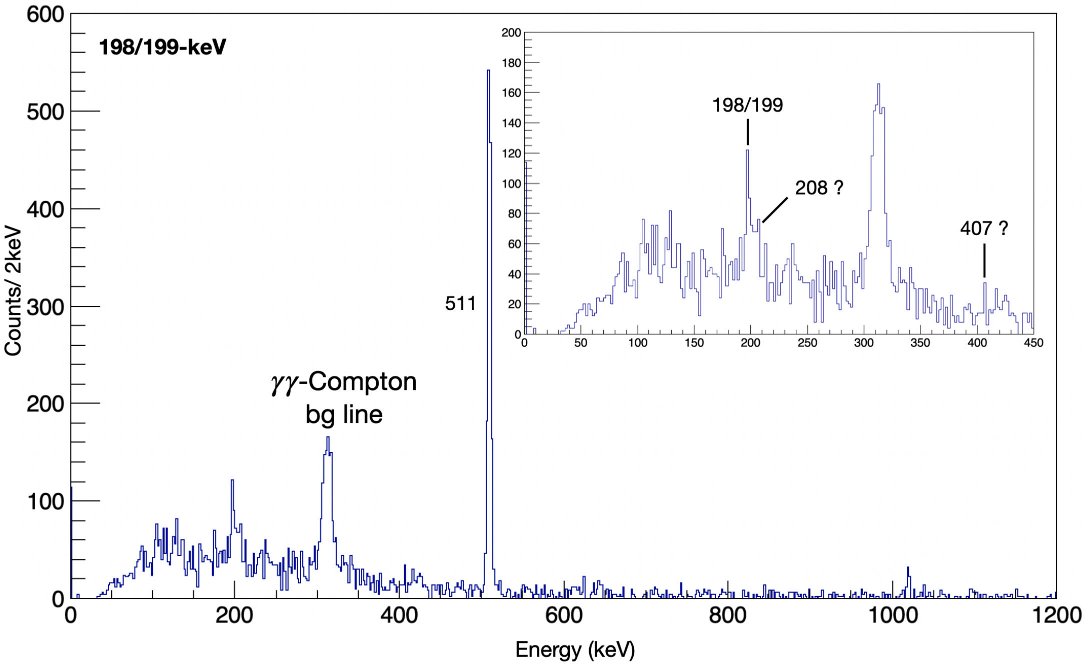

Figure 4.7: Background-subtracted β-delayed $\gamma\gamma$ coincidence spectrum gated on the 198/199-keV. An expanded low-energy region is shown in the spectrum in the top right. Peaks are observed at 199-keV, 310-keV and 511-keV (positron annihilation). The 198/199-keV peak corresponds to the feeding from the upper 407-keV state. A peak at 310-keV is observed because of the projection of an intense 511-keV diagonal band (generated by Compton scattering of 511 keV γ-rays) in the $\gamma\gamma$ coincidence spectra. A weak accumulation of counts centered around the 207-keV line and 407-keV line can also be seen.

by Fischer et al.[14] as shown in Fig. 1.9. The branching ratio for 199-keV transition is significantly different from the values published by Fischer et al.[14], however these are not directly comparable because the observed relative intensities for the overlapping transitions will depend on the populated states. In Fischer et al., ^{71}Br was populated via fusion evaporation and so lower-level transitions will be observed from the population of high-spin and high-energy states. In the case of ^{71}Kr β decay, only low-lying levels of ^{71}Br will be significantly populated. Even through there are a large number of ^{71}Kr implantations, there is a lack of statistics for certain γ-transitions (397-keV and 407-keV) due to the lower beta-decay efficiency coupled with the efficiencies for detecting γ-rays. This efficiency is exacerbated when looking at γ-γ coincidences. A comparison of γ intensities for ^{71}Br in the present work to the literature values is shown in Table 4.3. This experiment was not optimized to determine γ-branching ratios. Therefore, for the rest of the analysis γ intensities from Fischer et al.[14] were used as the experiment was optimized to determine the level scheme of ^{71}Br.

It is not uncommon for nuclei in this region of the chart to have a first-excited state that is almost degenerate with the ground state such as the 27-keV first-excited state in ^{73}Br, for example. In the case of ^{71}Br, there is only a 10-keV separation and having such a close first-excited state initiated the idea that there could be a rearrangement of states that result in

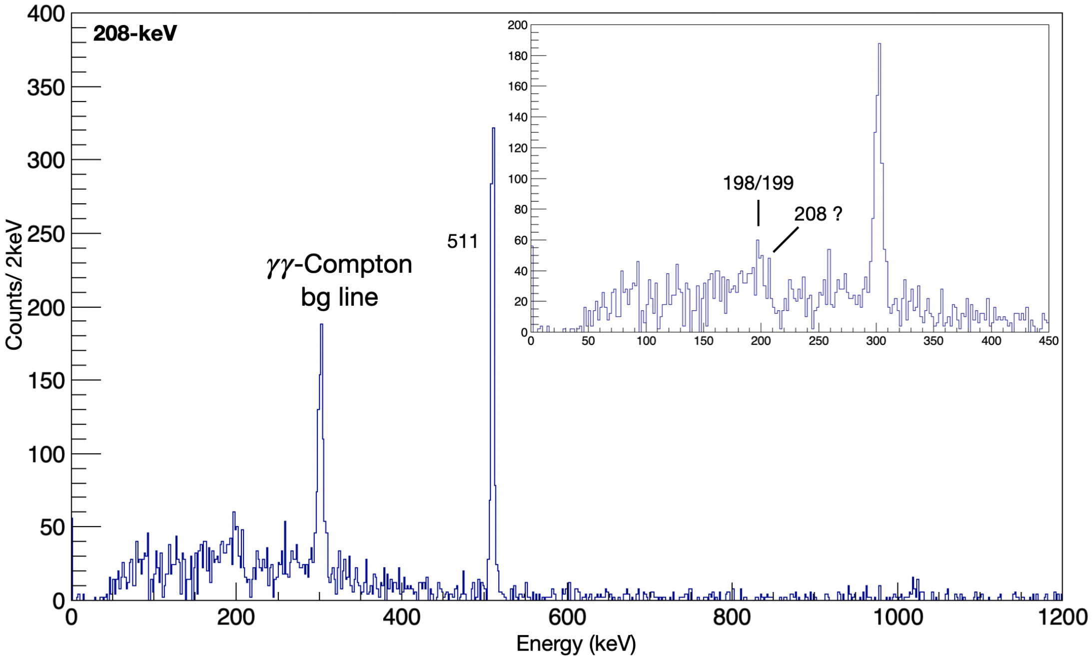

Figure 4.8: Background-subtracted β-delayed $\gamma\gamma$ coincidence spectrum gated on the 208-keV transition. An expanded low-energy region is shown in the spectrum in the top right. Peaks are observed at 199 keV, 300 keV and 511 keV (positron annihilation). The 198/199-keV peak corresponds to the feeding from the upper 407-keV state. A peak at 300 keV is observed because of the projection of an intense 511-keV diagonal band (generated by Compton scattering of 511 keV γ-rays) in the $\gamma\gamma$ coincidence spectra. As in Fig. refggProj198/199 a weak accumulation of counts around the 207-keV line can be seen.

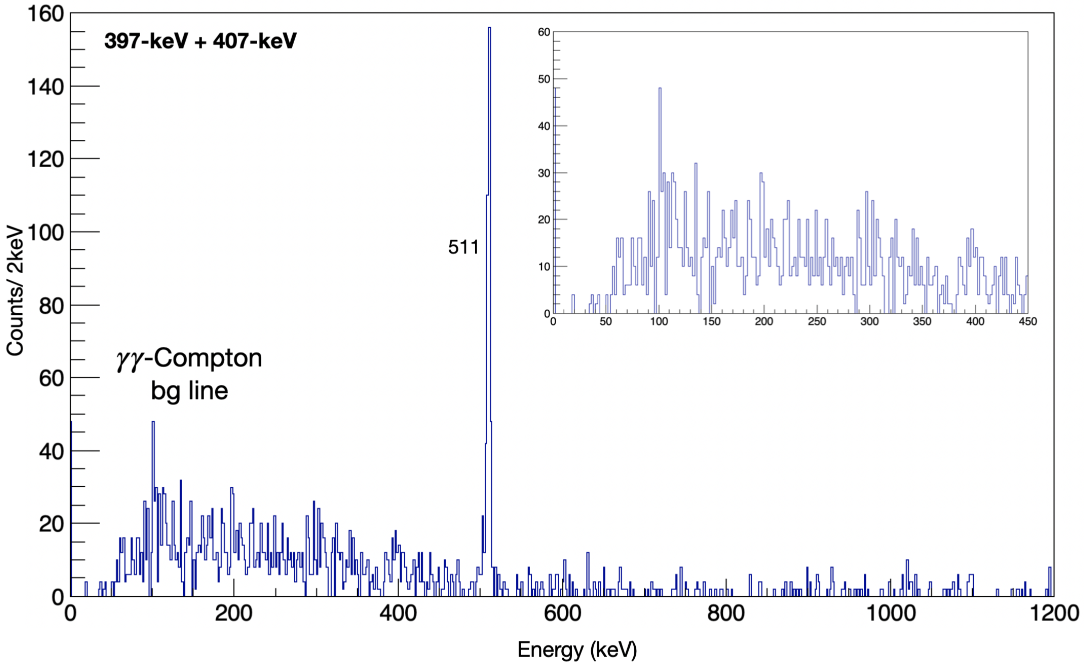

Figure 4.9: Background-subtracted β-delayed $\gamma\gamma$ coincidence spectrum gated on the 397-keV and 407-keV transitions. An expanded low-energy region is shown in the spectrum in the top right. Peaks are observed at 100 keV and 511 keV (positron annihilation). A peak at 100 keV is observed because of the projection of an intense 511-keV diagonal band (generated by Compton scattering of 511 keV γ-rays) in $\gamma\gamma$ coincidence spectra. An accumulation of counts around the 198-keV line can be seen.

γ-Energy (keV)	Area under the peak	γ Efficiency (%)
198	1490 ± 75	19.3 ± 0.3
208	477 ± 58	18.8 ± 0.3
397	117 ± 11	12.7 ± 0.4
407	256 ± 32	12.4 ± 0.4
943	144 ± 16	6.92 ± 0.4
199 in 198 gate	113 ± 11	19.3 ± 0.3
199 in 208 gate	42 ± 6	19.3 ± 0.3

Table 4.2: Number of counts under the γ-ray energy peaks in the background subtracted time gated γ-ray energy spectra shown in Fig. 4.6, 4.8 and 4.7

γ-Energy (keV)	γ Branching Ratio (%) This study	γ Branching Ratio (%) Fischer et al. [14]
198	72.5 ± 5.9	81
199	58.5 ± 5.9	15
208	27.5± 5.9	19
397	12.9 ±4.2	25
407	28.7 ± 9.8	60

Table 4.3: Comparison of γ-ray branching ratios of ^{71}Br in the present work with the literature values. The γ-ray branching ratios quoted from the reference [14] are an inference of β-decay scheme based on their detailed level scheme of ^{71}Br and previous β-decay experiment by Oinonen et al.[36].

different ground states between the mirror pair ^{71}Kr/^{71}Br.

An observation of a 598-keV γ-ray from the de-excitation of the 806-keV $(7/2)^-$ level as shown in Fig. 4.4 would have been extremely helpful in confirming the point that the ground state of ^{71}Kr is $(5/2)^-$. If the ground state of ^{71}Kr is less than $(3/2)^-$, it would be very unlikely to decay to a $(7/2)^-$ as the mode of the decay is significantly forbidden. Because there are two units of angular momentum change, this makes it an unlikely transition to occur. However, a peak around 598-keV was not observed in our work. It could be that there is some population of the $(7/2)^-$ state but it is a relatively small branch compared to other β-decay branches.

4.2.2 Charged-particle spectroscopy

Charged-particle spectroscopy will help us in understanding whether the different states are fed by β or proton decay. In the decay of ^{71}Kr, either a positron (β^+) or a positron along with a proton are emitted. The positron can easily escape the thin silicon detector by partially depositing it's energy since the range is fairly large for a positron in silicon[23]. A 5 MeV electron will travel about 1 mm before it loses all of its energy. The range in silicon for protons is fairly low. A 6-MeV proton will travel about 293 μm before it loses all of its energy. A 3-MeV proton has a range of 91 μm. If the ions stopped in the middle of the 520 μm thick DSSSD, protons could have travelled about 260 μm to the front side or back side before escaping the detector. Therefore nearly protons below 6 MeV deposit their total energy in the DSSSD (neglecting the depth variation of implanted ions). The background subtracted charged-particle energy spectrum is shown in Fig. 4.10. Background subtraction was done by following the same procedure that was used for γ-ray energy spectrum background subtraction.

The energy-loss of β-particles contribute to the lower energy region of the spectrum shown in Fig. 4.10. Events where the β-decay is followed by a proton emission, which happens almost simultaneously, contribute to the higher energy region above 1000-keV, since the protons below 6 MeV deposit all of their energy into the silicon detector, shown in Fig. 4.10. The charged-particle energy spectra includes a contribution from summing with the simultaneously emitted β-particle and proton resulting in a Landau distribution-like detector response.

The prominent structure in the lower-energy region of the spectrum is mainly from pure β-decay events. In the energy range of 1.5 MeV to 5 MeV of the spectrum two broad features can be observed due to proton decay events. The broadness of these structures can be attributed to the proton decay from a continuum of levels being populated in ^{71}Br above the proton separation energy.

The broad structures in Fig. 4.10 ranging from 1.5 MeV to 5 MeV are thus proton decays to ^{70}Se. These structures are in coincidence with 511-keV and 943-keV γ-rays according to Fig. 4.11. The 511-keV γ-rays emitted from positron annihilation, created by the β-decay of ^{71}Kr to ^{71}Br. The 943-keV γ-ray corresponds to the de-excitation from the first-excited (2^+) state of ^{70}Se to its ground state. Therefore, some of the proton events in the range of 1.5 MeV to 5 MeV are from the delayed-proton decay to first excited (2^+) state of ^{70}Se.

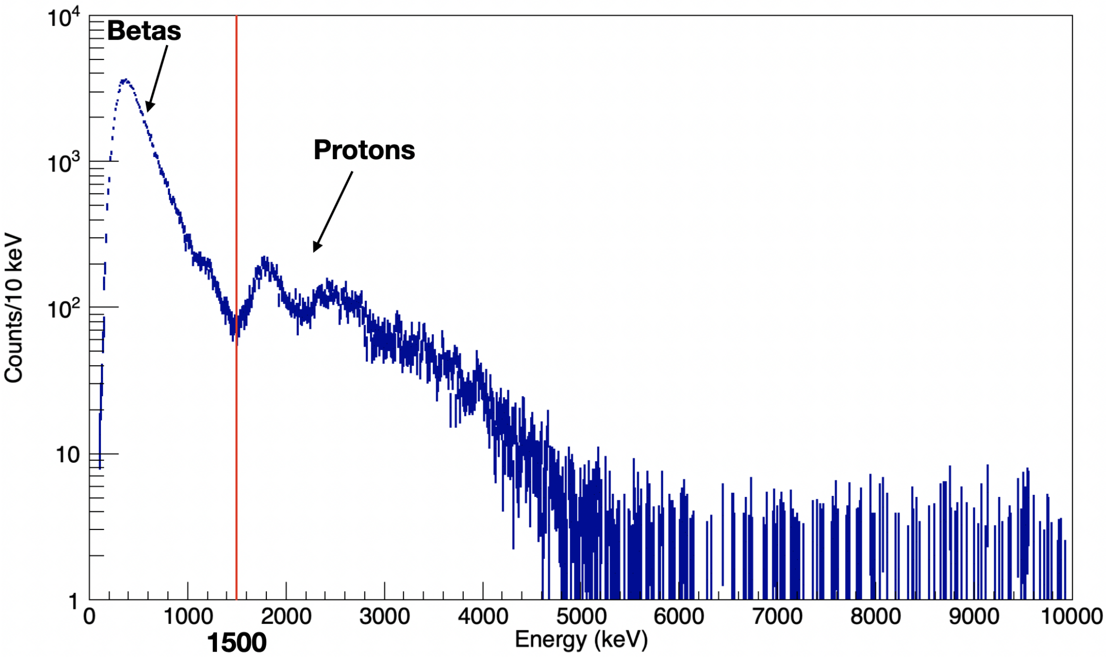

Figure 4.10: Background subtracted charged-particle spectrum for β-decay of ^{71}Kr and the subsequent proton decay of ^{71}Br. The spectrum shown corresponds to the front-side energy values of the DSSSD. Events were considered if they correlated within 1 s of implantation. 1500-keV energy gate is used to differentiate βs and protons.

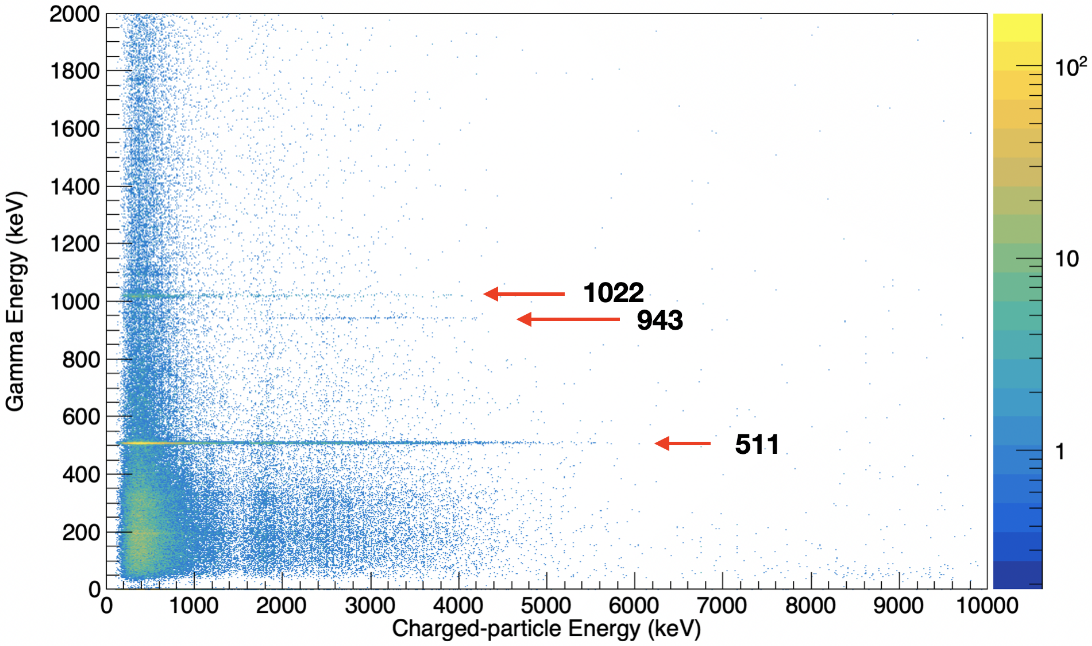

Figure 4.11: The γ-ray energy versus charged-particle energy matrix for ^{71}Kr β-decay. The 943-keV γ-ray is in coincidence with charged-particle energies from 1.5 MeV to 4.5 MeV. The colour scale represents the number of counts.

The projection of the gated 943-keV γ-ray to the charged-particle energy-axis is shown in Fig. 4.12. This spectrum represents the energy of the protons decaying to the 2^+ state of ^{70}Se. In order to perform β background subtraction, projection spectra were made considering energy bands (of similar width as the 943-keV projection) from above and below the 943-keV line. Those two spectra were averaged and subtracted from the 943-keV projection spectrum. A considerable amount of events below 1 MeV and a broad distribution from 1.5 Mev to 4.5 MeV can be observed. Observation of low-energy proton events suggests that there are proton-unbound levels close in relative energy to the 943-keV state that are also proton decaying to the 2^+ state of ^{70}Se as they deposit energies around 0.5 MeV. Furthermore it represents qualitatively, the level density of proton fed states.

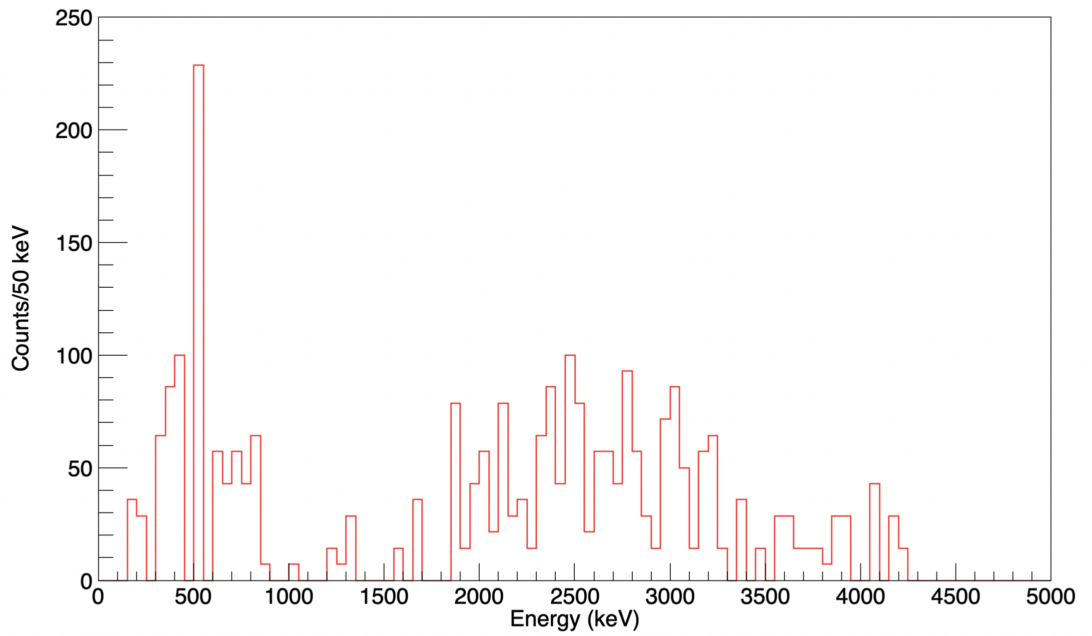

Figure 4.12: Background subtracted proton-energy spectrum in coincidence with 943-keV γ-rays.

4.3 $\beta\gamma$ and βproton branching ratios

One of the goals of this experiment was to also determine β-decay branching ratios to different levels in ^{71}Br and delayed-proton branching to levels in ^{70}Se. Since the β-decay feedings to excited states are followed by a γ-ray, the branching ratios can be determined by using the absolute γ-ray intensities. In order to determine the branching ratios we need to rely on the precise absolute efficiency calibration of the HPGe detector and a reasonable understanding of the relative efficiencies of the β-detector.

4.3.1 β and proton efficiencies

In order to estimate β-branching ratios of ^{71}Kr, the DSSSD detection efficiencies for β's and protons were determined. The proton detection efficiency of the DSSSD was measured using a known β-delayed proton emitter, ^{73}Sr. The Fermi β-decay of the parent nucleus decays into the IAS of the daughter nucleus ^{73}Rb and immediately proton decays to ^{72}Kr since it is completely

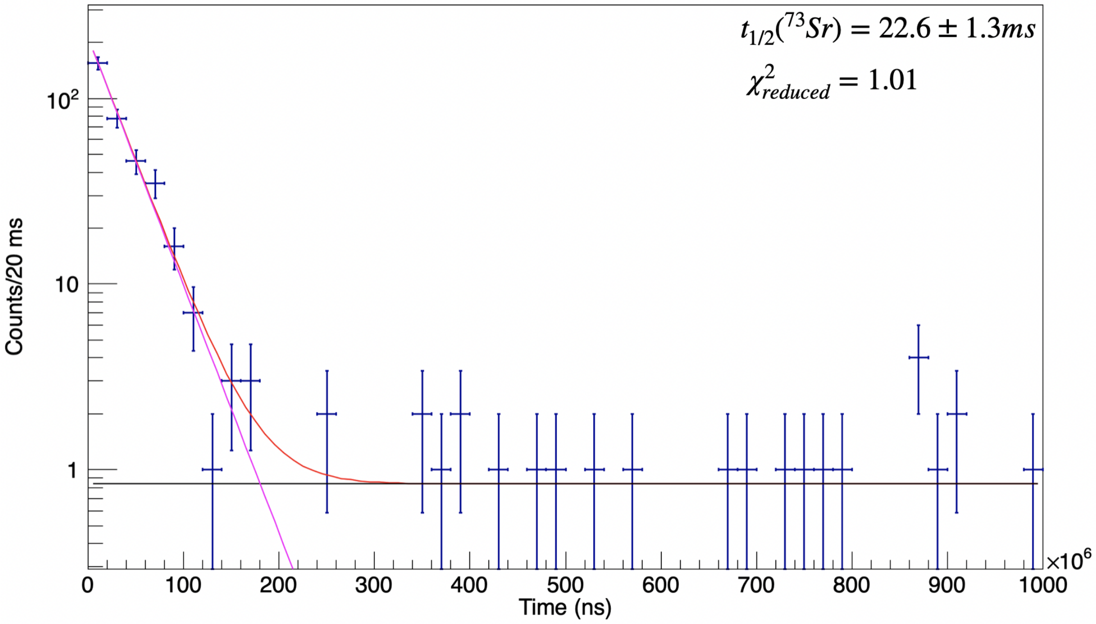

Figure 4.13: The time distribution of the decay events following the identification of ^{73}Sr nuclei. A decay time fitted with an exponential decay (magenta) and a constant background (black) resulting in the combined fit (red). The half-life extracted for ^{73}Sr is 22.6 ± 1.3ms.

proton-unbound. To determine the proton efficiency the decay curve of ^{73}Sr as shown in Fig. 4.13 was analysed. The position-correlation utilized a 24-strip tolerance and only events that occurred within 250 ms of implantation were considered. The total number of ^{73}Sr ions cleanly identified, i.e. those having a well-defined front and back strip, was 369, and of these 336 were detected in time-correlation with an implant event, yielding a proton-detection efficiency of 91.1 ± 6.9 %.

Similarly, in order to calculate the β detection efficiency, a known almost pure β emitter was used. Therefore, to measure the β efficiency the decay curve of ^{70}Br as shown in Fig. 4.14 was analysed. The position-correlation utilized a 24-strip tolerance and only events occurring within 10-s of implantation were considered, in large part due to the long-lived β-decaying isomer [32] [50]. The total number of ^{70}Br ions identified in the PID was 676240, and of these 166906 were detected in time-correlation, yielding a β-detection efficiency of 24.7 ± 0.1 %.

To determine the branching ratios for β-delayed proton emission, a method of separating pure β-decay events and βp decay events is required. The two distributions can overlap, and because we did not have any methods for differentiating these two types of event, the separation of the βp events was based purely on the energy deposition on DSSSD. For the most part, β-particles are expected to deposit less than 1.5 MeV in the detector, although there is a large tail to higher energies from the Landau-like distribution. In comparison, protons in this mass region typically have energies above 1.5-MeV, in large part due to the Coulomb barrier, and therefore are expected to deposit more than 1.5-MeV in a single pixel.

The total number of decays recorded in the DSSSD can be written as:

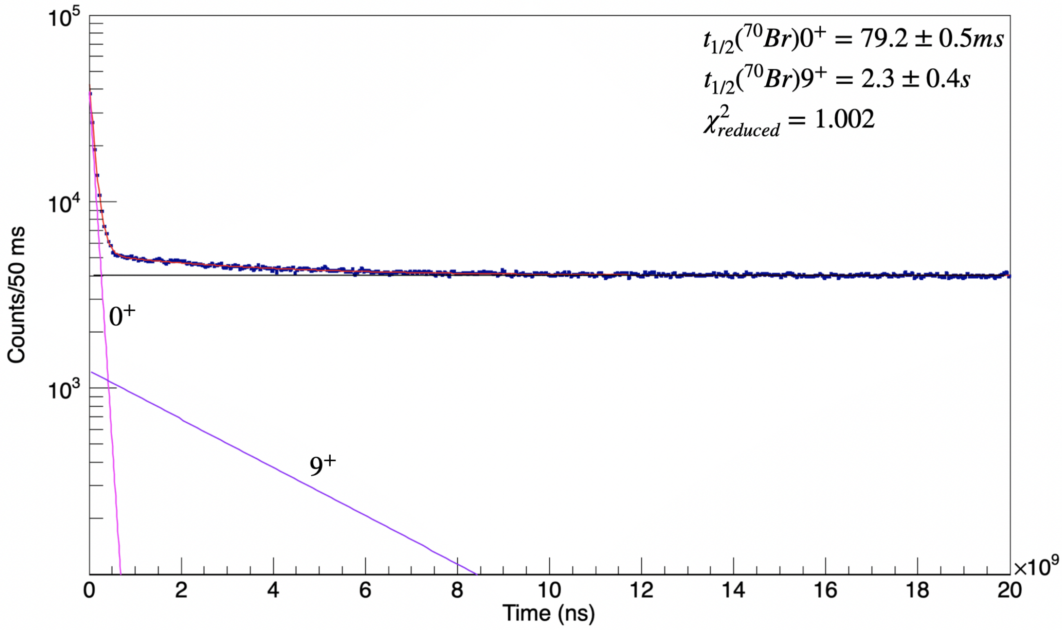

Figure 4.14: The time distribution of the decay events following the identification of ^{70}Br nuclei. A decay time fitted with an exponential decay of ground state of ^{70}Br (magenta), 9^+ isomer (purple) and a constant background (black) resulting in the combined fit (red). The half-life extracted for ground state of ^{70}Br and 9^+ isomer is 79.2 ± 0.5 ms and is 2.3 ± 0.4s respectively.

$$N_{\text{Measured Decays}} = N_\beta \epsilon_\beta + N_p \epsilon_p \tag{4.1}$$

where, N_β is the total number of β-decays, ϵ_β is the β detection efficiency, N_p is the total number of proton-decays and ϵ_p is the p detection efficiency.

The total number of decays recorded in the DSSSD can be found by the integral from 0 s to 1 s in the background subtracted decay curve which is 171158(414). The number of events with energy greater than 1500 keV in charged-particle energy spectrum is 31826(178)(measured number of protons). After correcting the measured number of protons, for DSSSD proton detection efficiency it is found out that 34951(2643) protons were emitted.

The number of events with energy lower than 1000 keV in charged-particle energy spectrum is 139332(451)(measured number of βs). After correcting the measured number of βs, for DSSSD β detection efficiency it is found out that 564520(2390) βs were emitted. Therefore, the total number of emitted charged-particles is 599472(3563).

From theses considerations, the Branching ratio for proton unbound states was 4.1±0.3 % , obtained by comparing total number of emitted charged-particles (599472) to total number of emitted protons (34951). The previous work by Oinonen et al.[36] at ISOLDE, obtained a value of 2.1±0.7% for the β-proton branch ratio while Fischer et al. [14] predicted 2 %.

βp events were identified by requiring an energy deposition of more than 1.5-MeV in the implantation pixel or in the neighbouring pixels (i.e. the considered position-correlation). This procedure misses proton activity below 1.5-MeV. However, as the β-particle tail exceeds this 1.5-MeV limit, both parts compensate each other reasonably well.

To get an estimate for the systematic error of such a procedure, we also determined the total proton-emission branching ratio for a threshold of 1-MeV. By varying the 1.5-MeV energy cut to 1-MeV, the proton branching changed from 4.1 % to 5.8 %. The percentage change in the two proton branching ratios is about 29%.The difference between the 1-MeV cut and the 1.5-MeV cut analysis was used as the systematic error for the β proton and $\beta\gamma$-branching ratios is on the order of 29%. Only the statistical uncertainty is quoted with the reported branching ratios.

One of the largest sources of error is the inability to distinguish between $\beta\gamma$ and βp events. In order to improve the identification of β's and protons the detector response for pure β's should be modeled [30][28]. A pure proton spectrum can be obtained after subtracting the pure β-events from the charged-particle spectrum.

4.3.2 β-proton decay branch

As mentioned in the previous section, the proton-unbound states in ^{71}Br fed by ^{71}Kr, can emit a proton and decay to ^{70}Se. Depending on the spin of the proton unbound state, ^{71}Br can decay to excited states of ^{70}Se after emitting protons, which will de-excite via γ-emission. In order to have a closer look into the ^{70}Se de-excitation γ-rays, a proton energy gated γ-ray energy spectrum was made as shown in Fig. 4.15.

The observation of a 943-keV, 653-keV γ-ray confirms the proton decay to the 2^+ 943-keV and 1600-keV states in ^{70}Se as shown in Fig. 4.15. A gate on the 943-keV peak was made with a background subtracted $\gamma\gamma$ coincidence spectrum to determine the contribution to the 943-keV peak from the de-excitation from 1600-keV state as shown in Fig. 4.16. And signs of 653-keV was not observed. Therefore, it is not clear that 1600-keV state is fed by proton decay. However, levels above the 2^+ 943-keV state in ^{70}Se could also be proton fed with a smaller ratio. But since proton-decay prefers a large phase-space, it will preferentially decay to the lowest allowed energy states. Therefore, proton feeding to states above 2^+ state is unlikely to occur. This 943-keV γ-ray transition was not observed, although it was predicted, by the previous β-decay experiment on ^{71}Kr [36].

When the proton is emitted from the proton unbound states of ^{71}Br it must obey the following angular momentum change rule.

$$\mathbf{J_f} - \mathbf{J_i} = \boldsymbol{\ell} + \mathbf{s}. \tag{4.2}$$

The total angular momentum the proton carries away between the initial and final states

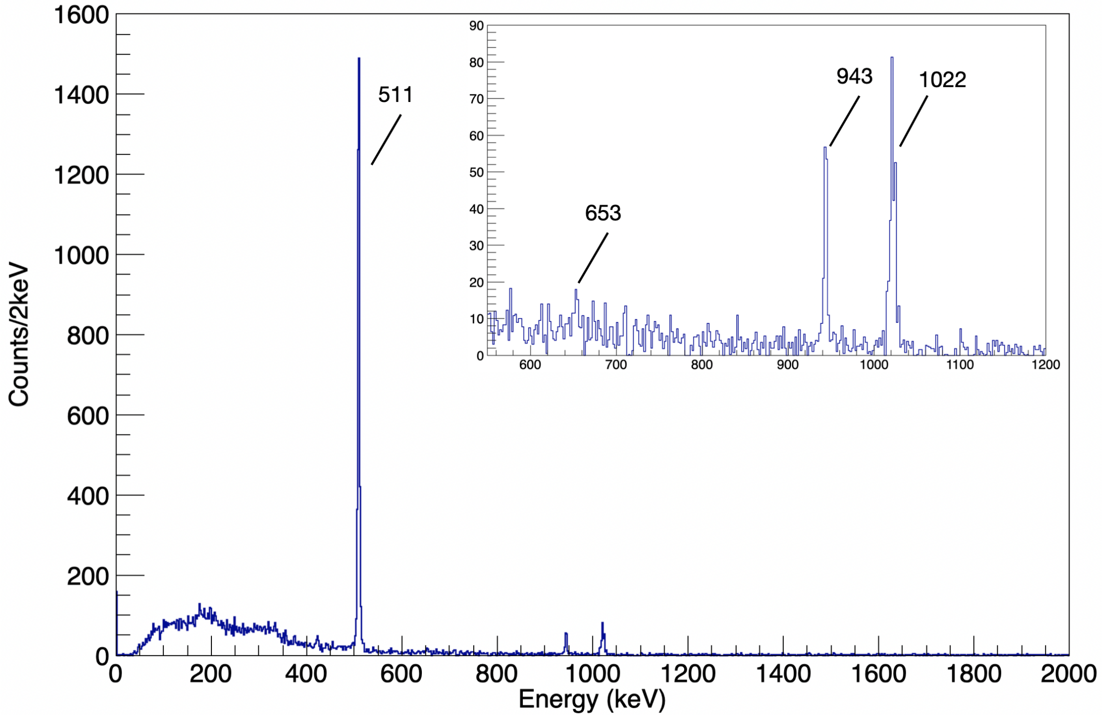

Figure 4.15: Background subtracted γ-ray energy spectrum gated on charged-particle events above 1.5-MeV, arising from the β-decay of ^{71}Kr within 1 s of implantation. Expanded energy region (550-keV to 1200-keV) is shown in the top right and the $2^+ \rightarrow 0^+$ 943-keV transition in ^{70}Se is seen. A peak in 653-keV is observed. This possibly could be from the γ de-excitation of 1066-keV state to 943-keV state. Peaks are observed at 511-keV(positron annihilation) and 1022-keV(511 keV summation).

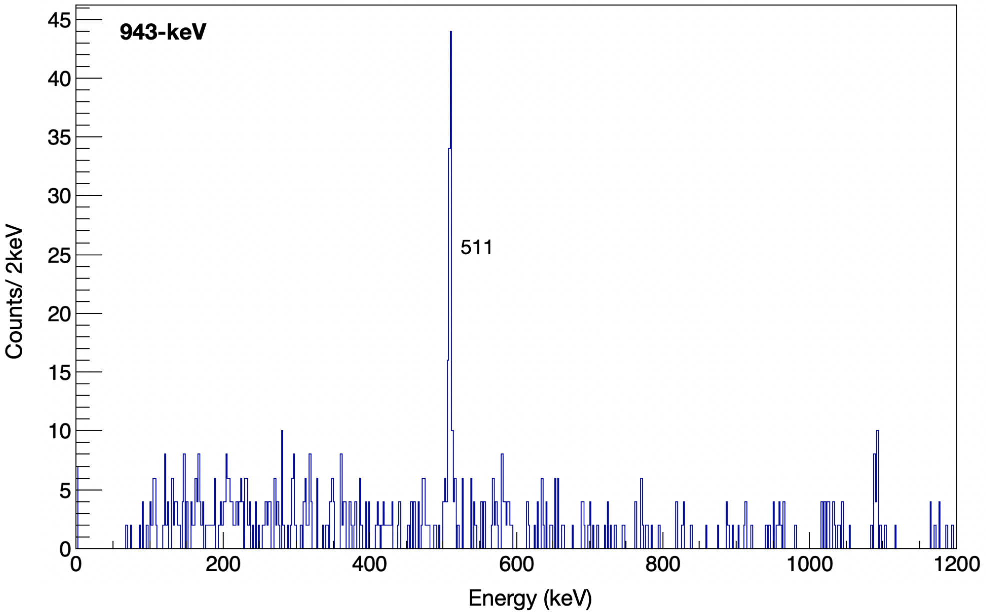

Figure 4.16: Background subtracted β-delayed $\gamma\gamma$ coincidence spectrum gated on the 943-keV. A peaks is observed at 511-keV (positron annihilation).

must go into both the orbital angular momentum ℓ and the intrinsic spin of the proton s, which is $1/2\hbar$. The orbital angular momentum, ℓ, and the intrinsic angular momentum, s, of the proton can couple to a number of values. These values are integer or half integer values between $|J_f - J_i|$ and $J_f + J_i$. For example, if the initial $J_i = 3/2$ and the final $J_f = 2$, then the orbital plus intrinsic angular momenta can both couple to J=1/2, J=3/2, J=5/2 or J=7/2 . Since the intrinsic angular momentum of a proton is always 1/2, this means that the ℓ value is ℓ=0 for J=1/2, $\ell = 1$ for J=3/2, ℓ=2 for J=5/2 or finally ℓ=3 for J=7/2. The amount of orbital angular momentum ℓ the proton carries away will affect the potential barrier it must pass through. Higher the ℓ, higher the angular momentum barrier that proton experience. Therefore lower ℓ channels are more favorable. Since proton-decay prefers large phase-space, it will preferentially decay to the lowest allowed energy states.

The observation of proton-decay branch to the 2^+ state in ^{70}Se strengthens the idea that the ground state of ^{71}Kr is $J^\pi = 5/2^-$ [38][39][10]. For there to be an appreciable amount of decays to the $J^\pi = 2^+$ state in ^{70}Se, the initial unbound states in ^{71}Br must have $J \geq 5/2$. If the ground state of ^{71}Kr were to have $J^\pi = 1/2^-$ spin then this would be very unlikely as the β-decay would have to proceed to a $3/2^-$ (a small probability) which then decay to the 2^+ state in ^{70}Se (also a small probability). Thus the observation of this transition strengthens the $J^\pi = 5/2^-$ spin assignment of ^{71}Kr.

To calculate the absolute proton-decay branches one needs a measure of the total number of ^{71}Br that decayed into each level in ^{70}Se. The intensity of 943-keV γ-ray that decayed from 2^+ state in ^{70}Se can then be used to determine the proton population to 2^+ state. The number of counts under 943-keV peak was determined by fitting the peaks with a Gaussian and a constant background.

The proton branching ratio of the 943-keV level of ^{70}Se can be written as:

$$\mathrm{BR}_{943} = \frac{P_{943}}{N_{\mathrm{Protons}}} \tag{4.3}$$

where, P_{943} is the proton-population of the 943-keV in ^{70}Se level and $\mathrm{N}_{\mathrm{Protons}}$ is the total number of emitted protons. The proton-population to the 943-keV level in ^{70}Se can then be found by:

$$P_{943} = \frac{A_{943}}{I_{943}\epsilon_{943}\epsilon_t} \tag{4.4}$$

where, A_{943} is the area under 943-keV peak in background subtracted β-gated γ-ray energy spectrum, ϵ_{943} is the detection efficiency of 943-keV γ-ray, ϵ_t is the proton (trigger) efficiency and I is the branching ratio of 943-keV γ-ray.

The proton-branching ratio to the 2^+ state in ^{70}Se was calculated using the equations 4.3 and 4.4 with the assumption that the states above 943-keV do not contribute to the βp branch. Out of the 4.1±0.3 % that decayed to proton unbound levels, as shown in fig. 4.17, about 8.9±4.6 % were found to decay through the 2^+ state in ^{70}Se. The β-decay has to have a spin change to reach $3/2^-$ states in ^{71}Br to be able the to have (ℓ=1) protons to make (2^+) in ^{70}Se. This adds more strength to the idea that β decay has to be occurring from a state with spin greater than $1/2^-$.

To calculate the absolute β-decay branches one needs a measure of the total number of ^{71}Kr atoms that decayed into each level in ^{71}Br. The intensity of γ-rays that decayed from those states in ^{71}Br can then be used to determine the population of each state. The number of counts for these γ-rays were determined by fitting the peaks with a Gaussian and a constant background.

The β branching ratio of the i^{th} level of ^{71}Br can be written as:

$$\mathrm{BR}_i = \frac{P_i}{N_{\text{Charged particles}}} \tag{4.5}$$

where, P_i is the β-population to the i^{th} level and $\mathrm{N}_{\text{Charged particles}}$ is the total number of emitted charged-particles. The β-population to the 407-keV level in ^{71}Br can then be found by,

$$P_{407} = \frac{A_{407}}{I_{407}\epsilon_{407}\epsilon_t} \tag{4.6}$$

where, A_{407} is the area under 407-keV peak in background subtracted β-gated γ-ray energy spectrum, ϵ_{407} is the detection efficiency of γ-energy, ϵ_t is the β (trigger) efficiency and I is the branching ratio of the 407-keV γ-ray.

The 208-keV level in ^{71}Br is fed by βs as well as γ de-excitation of 407-keV state. Considering those two feedings the β-population to the 208-keV level in ^{71}Br can be found by,

$$P_{208} = \frac{A_{208} - P_{407}I_{199}I_{208}\epsilon_{208}\epsilon_t}{I_{208}\epsilon_{208}\epsilon_t} \tag{4.7}$$

where, A_{208} is the area under 208-keV peak in background subtracted β-gated γ-ray energy spectrum, ϵ_{208} is the detection efficiency of 208-keV γ-energy, ϵ_t is the β (trigger) efficiency and I is the branching ratio of the 208-keV γ-ray.

The β-branching ratios to different energy states were calculated using the equations 4.5 4.7, and 4.6. The counts under considered peaks and efficiencies are shown in Table 4.2. The calculation was done under the assumption that the states β fed above 407-keV are not contributing to the $\beta\gamma$-branch. The branching ratio to the 208-keV and 407-keV states were found to be 8.3±1.4% and 2.3±0.9%. The ground-state branch was determined by subtracting the total branching ratios to excited states from 100%. β feeding to the ground state was 85.3±1.7%

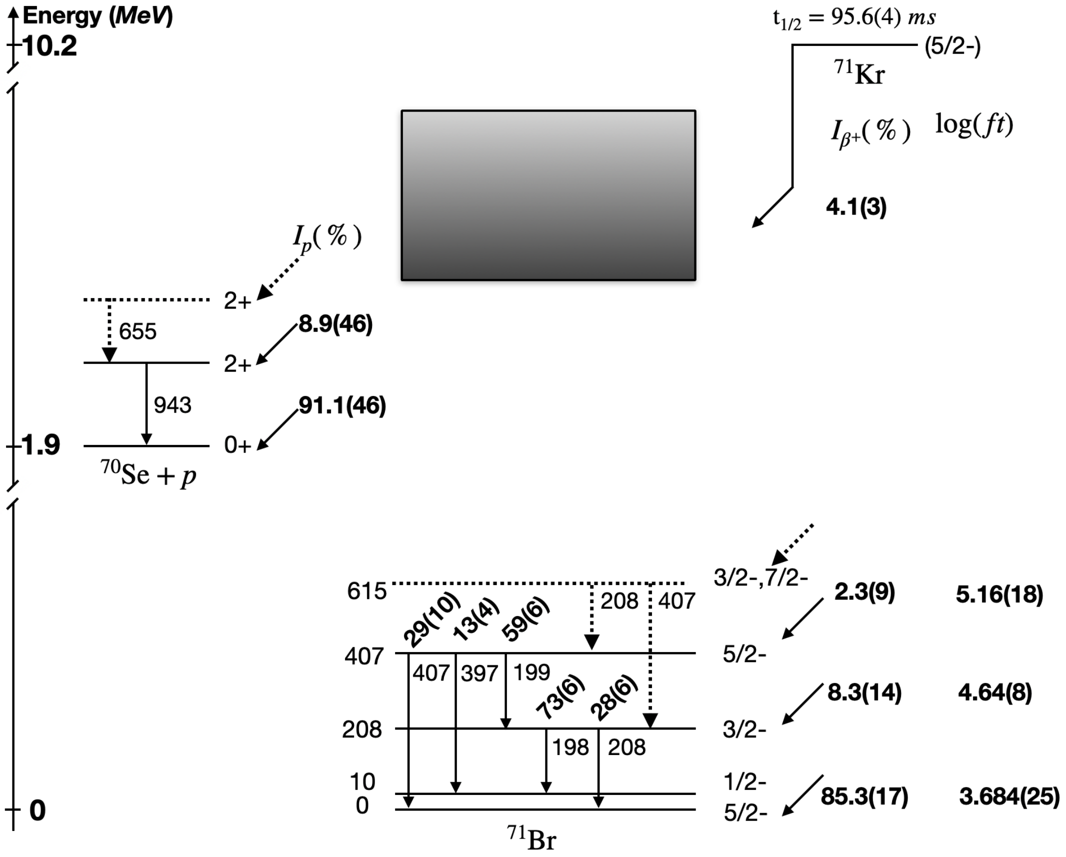

Figure 4.17: Deduced β-delayed proton decay scheme of ^{71}Kr. Charged-particle events above 1.5-Mev are considered as protons. The proton unbound states (continuum of states) in ^{71}Br are denoted as a rectangle. Only the statistical uncertainty is quoted with the reported branching ratios. Unobserved states are shown in dashed lines [48].

Energy state (keV)	I (%) This study	I (%) [36]	I (%) [14]	I (%) [7]
Ground state of 71Br	85.3 ±1.7	82.1 ±1.6	68	-
208 of 71Br	8.3 ±1.4	15.8 ±1.4	15	-
407 of 71Br	2.3 ±0.9	-	15	-
Proton unbound states of 70Se	4.1 ±0.3	2.1 ±0.7	2	5.2 ±0.6
943 keV of 70Se	8.9 ±4.6	-	-	-
Ground state of 70Se	91.1 ±4.6	-	-	-

Table 4.4: Comparison of β and proton branching ratios (I) obtained for ^{71}Kr in the present work with the literature values.

yielding a total $\beta\gamma$-branch of 95.9±1.7%.

The ground-state branching that is reported in this work, 85.3±1.7%, is consistent with the value obtained by Oinonen et al.[36] which was 82.1±1.6 %. It is obvious that the ground state has the largest energy difference and thus the largest phase-space. Since β-decay prefers large phase-space, it will tend to preferentially decay to the lowest-allowed energy states. Apart from larger phase-space, β-decay prefers to minimize the change in angular momentum. Therefore, our results are consistent with the ground-state spin of ^{71}Kr being identical to that of ^{71}Br to achieve this lowest possible change in angular momentum.

A comparison with the previously measured [7], [36] and deduced[14] branching ratios is shown in Table 4.4. The branching to the 207-keV state of 9.2±1.5% is significantly different from the previous observation of 15.8 ±1.4%. Interestingly however, we were able to observe a 5.8 ±0.4% branch feeding the 407-keV state which was not observed by Oinonen et al.[36]. This might be due to the lack of statistics in their measurement resulting in the non-obervation of a 407 and 397-keV transition. This particular feeding was predicted by Fischer et al. [14] but the predicted branching is very different from ours. However, the strong β-decay (15 % each) to excited states predicted by Fischer et al. between this mirror pair was not observed.

5 SUMMARY AND CONCLUSIONS

This thesis reports on the β- and γ-ray spectroscopy of proton-rich ^{71}Kr from an experimet that was performed at the NSCL at MSU in October 2017. The nuclei of interest, ^{71}Kr were produced via fragmentation of a 120-MeV/nucleon ^{92}Mo primary beam. ^{92}Mo was a newly developed beam that was used to populate the exotic nuclei in the region around ^{73}Sr. The nuclei of interest were additionally filtered by the radio-frequency fragment separator (RFFS) [4][15] before being transported to the experimental end station. The RFFS made this experiment feasible by considerably purifying the beam cocktail, and is a very useful separator for proton-rich beams.

One of the main questions of this work was to determine whether the nuclide ^{71}Kr and its mirror partner ^{71}Br have different ground state spins as the ground state character of ^{71}Kr is not well known. It was theoretically interpreted [49] that the ground state of ^{71}Kr could be interchanged with closely spaced first excited state. To disentangle whether mirror-symmetry was broken, the β-decay branches of ^{71}Kr were studied in order to constrain the ground-state spin of ^{71}Kr. Specifically, signature of the population to $7/2^-$ states of ^{71}Br were searched for but not observed. β-delayed proton emission provides a unique method of probing the spin of decaying states, as the proton decay is sensitive to angular momentum of the decay[22].

As part of this analysis using implant-decay correlations, a improved constraint was put on the β-decay half-life of ^{71}Kr, which was found to be 95.6(4) ms. The observed features of the β-delayed proton energy spectrum obtained for ^{71}Kr confirm that a continuum of proton decaying states in ^{71}Br are being populated by the β-decay of ^{71}Kr, as was previously observed [36]. In order to determine branching ratios from the data on ^{71}Kr, β and proton detection efficiencies were measured with ^{70}Br and ^{73}Sr. Interestingly, a strong population of the 9^+ isomeric state in ^{70}Br [32] was observed.

The β-delayed γ-rays were analyzed to identify the states in ^{71}Br and ^{70}Se that have been fed by β-decay and delayed proton decay. The β-γ coincidence technique is a powerful way to achieve this goal. It was that the ground state, 208-keV and 407-keV states of ^{71}Br were fed 85.3(17) %, 8.3(14)% and 2.3(9) % of the time respectively. The data recorded were used to search for new β feedings to states above 407-keV, however the results were inconclusive on the feeding of higher energy levels. More than 80 % of the time ground state was populated, which implies that the wave-functions of the ^{71}Kr and ^{71}Br ground states can not be much different from each other and strengthen the idea of mirror symmetry of the ground states in this pair is preserved. The proton unbound states in ^{71}Br were found to be fed 4.1(3) % of the time, and of these 8.9(46)% were found to decay to the 2^+ state in ^{70}Se. The observation of proton decay to 943-keV state ^{70}Se, observed for the first time, confirms that ground state of β-decay parent has to be greater than $3/2^-$ in order to β-delayed proton decay to a 2^+ state so strongly. Based on that argument one of two possibilities for ground state spin of ^{71}Kr, which is $1/2^-$ can be completely excluded. Therefore, this work suggests that the ground state spin of ^{71}Kr is $5/2^-$ and the mirror symmetry between ground state spin of ^{71}Kr/^{71}Br pair is preserved.

5.1 Future Work

Further work on the ^{71}Kr decay energy spectrum is needed to constrain the $\beta\gamma$ branch and βproton branch in to a greater extent. The discrimination of β and proton decay events using 1000-keV energy cut is one of main uncertainties in obtaining the different branching ratios. By varying the 1000-keV energy cut to 1500-keV, the proton branching changed from 5.8 % to 4.1 %. This systematic error is very large compared to the statistical error. Modelling the detector response for pure beta and beta protons through sophisticated simulation techniques (such as GEANT4) might allow us to differentiate between those events and would be further interesting extension to the present work. It may also be possible to model the resulting distribution of β-γ events by finding an appropriate model that incorporates the effect of the energy threshold on the pure β-spectrum.

A further investigation into β-delayed proton spectrum for ^{71}Kr is needed, as the low statistics in this work could not yield a definite answer. For example, it was observed that there may be low-energy protons associated with proton decays to the 2+ state in ^{70}Se but not much can be said about this distribution to the low number of counts. Observing a greater number of decays would further the knowledge about the continuum of states above proton separation energy that were populated. If an experiment to further investigate the β-delayed proton spectrum of ^{71}Kr were performed, implementing a technique to do identification of β and protons by energy loss and total energy would provide better separation. This could be achieved by implanting the beam on a tape in conjunction with detector telescope to measure energy loss and total energy. Also, due to the number of overlapping γ-ray transitions in ^{71}Br an analysis of the β-γ branching ratios was complicated. If the full energy of the β particles were measured, then the end point energy of βs in coincidence with particular γ rays would allow for a direct determination in the population of certain states.

Collecting the statistics necessary in a similar experiment, to characterize the ^{71}Kr β-decay fed excited states in ^{71}Br would require an accelerator facility that could produce ^{71}Kr at higher intensities than what was obtained in this experiment. Since the level scheme of ^{71}Br consisted of many similar and overlapping γ-ray transitions γ-γ coincidence studies were required to extract γ branching ratios. The decay scheme presented in this work is based on the assumption that proton bound states above 407-keV level do not contribute to the $\beta\gamma$-branch. But ultimately contribution from those states should be checked and included, as there are many transitions with overlapping energies. Therefore, a detector setup improving the efficiency of both β and γ-detection would aid in improving the number of statistics collected, as the present work was limited by the fact that having low statistics in β-gated γ spectrum. A future experiment using a similar setup with an advanced γ spectrometer, such as GAMMASPHERE or GRETINA would allow for better γ-spectroscopy and putting to rest the the idea that mirror symmetry is violated in the ground states of ^{71}Kr/^{71}Br.

References

[1] Energy level diagrams A=10 -TUNL. http://tunlweb.tunl.duke.edu/nucldata.shtml, 2017. Online; accessed 05 August 2020.

[2] J.W. Arrison, T. Chapuran, U.J. Hüttmeier, and D.P. Balamuth. Electromagnetic transitions in the N= Z + 1 nucleus ^{71}Br. *Physics Letters B*, 248(1):39 – 43, 1990.

[3] H. Bateman. The solution of a system of differential equations occurring in the theory of radioactive transformations. *In Proc. Cambridge Philos. Soc*, 15:423–427, 1910.

[4] D Bazin, V Andreev, A Becerril, M Doléans, PF Mantica, J Ottarson, H Schatz, JB Stoker, and J Vincent. Radio frequency fragment separator at nscl. *Nuclear Instruments and Methods in Physics Research Section A: Accelerators, Spectrometers, Detectors and Associated Equipment*, 606(3):314–319, 2009.

[5] B. Blank. Studies with one- and two-proton drip line nuclei. *Springer*, 2003.

[6] B. Blank and M.J.G. Borge. Nuclear structure at the proton drip line: Advances with nuclear decay studies. *Progress in Particle and Nuclear Physics*, 60(2):403 – 483, 2008.

[7] B. Blank et al. β-delayed proton emission from the proton-rich isotopes ^{67}Se, ^{71}Kr, and ^{75}Sr. *Phys. Lett. B*, 364:8–12, 1995.

[8] J. Chadwick. Possible existence of a neutron. *Nature*, 129(3252):312–312, 1932.

[9] C. N. Davids, P. J. Woods, D. Seweryniak, A. A. Sonzogni, J. C. Batchelder, C. R. Bingham, T. Davinson, D. J. Henderson, R. J. Irvine, G. L. Poli, J. Uusitalo, and W. B. Walters. Proton radioactivity from highly deformed nuclei. *Phys. Rev. Lett.*, 80:1849–1852, Mar 1998.

[10] M. Del Santo, Z. Meisel, D. Bazin, A. Becerril, B.A. Brown, H. Crawford, R. Cyburt, S. George, G.F. Grinyer, G. Lorusso, P.F. Mantica, F. Montes, J. Pereira, H. Schatz, K. Smith, and M. Wiescher. β-delayed proton emission of ^{69}Kr and the ^{68}Se rp-process waiting point. *Physics Letters B*, 738:453 – 456, 2014.

[11] C. Dossat, N. Adimi, F. Aksouh, F. Becker, A. Bey, B. Blank, C. Borcea, R. Borcea, A. Boston, M. Caamano, G. Canchel, M. Chartier, D. Cortina, S. Czajkowski, G. de France, F. de Oliveira Santos, A. Fleury, G. Georgiev, J. Giovinazzo, S. Grévy, R. Grzywacz, M. Hellström, M. Honma, Z. Janas, D. Karamanis, J. Kurcewicz, M. Lewitowicz, M.J. López Jiménez, C. Mazzocchi, I. Matea, V. Maslov, P. Mayet, C. Moore, M. Pfützner, M.S.

Pravikoff, M. Stanoiu, I. Stefan, and J.C. Thomas. The decay of proton-rich nuclei in the mass A=36–56 region. *Nuclear Physics A*, 792(1):18 – 86, 2007.

[12] Joachim B. Ehrman. On the displacement of corresponding energy levels of ^{13}C and ^{13}N. *Phys. Rev.*, 81(3):412–416, 1951.

[13] Alfredo Estrade. *Time-of-flight mass measurements of neutron rich isotopes at the NSCL*. Michigan State University, 2010.

[14] SM Fischer, T Anderson, P Kerns, G Mesoloras, D Svelnys, CJ Lister, DP Balamuth, PA Hausladen, and DG Sarantites. Shape coexistence in ^{71}Br and the question of the ground-state spin of ^{71}Kr. *Physical Review C*, 72(2):024321, 2005.

[15] D. Gorelov, V. Andreev, D. Bazin, M. Doleans, T. Grimm, F. Marti, John Vincent, and X. Wu. Rf-kicker system for secondary beams at the nscl. pages 3880 – 3882, 06 2005.

[16] E. Hagberg, J.C. Hardy, H. Schmeing, H.C. Evans, U.J. Schrewe, V.T. Koslowsky, K.S. Sharma, and E.T.H. Clifford. The decay of a new nuclide: ^{71}Br. *Nuclear Physics A*, 383(1):109 – 118, 1982.

[17] W. Heisenberg. Über den bau der atomkerne. i. *On the Structure of Atomic Nuclei*, 77, 1932.

[18] Jack Henderson. Decay tagging of neutron – deficient ^{73}Sr, ^{74}Sr. PhD thesis, University of York, 2014.

[19] D. E. M. Hoff, A. M. Rogers, S. M. Wang, K. Childers K. Bender, P. C. Brandenburg, J. A. Clark, A. C. Dombos, E. R. Doucet, S. Jin, R. Lewis, S. N. Liddick, C. J. Lister, Z. Meisel, W. Schatz H. Schmidt K. Soltesz D. Subedi S. K. Morse, C. Nazarewicz, and S. Waniganeththi. Mirror-symmetry violation in bound nuclear ground states. *Nature*, 580, 2020.

[20] D. E. M. Hoff, A. M. Rogers, S. M. Wang, K. Childers K. Bender, P. C. Brandenburg, J. A. Clark, A. C. Dombos, E. R. Doucet, S. Jin, R. Lewis, S. N. Liddick, C. J. Lister, Z. Meisel, W. Schatz H. Schmidt K. Soltesz D. Subedi S. K. Morse, C. Nazarewicz, and S. Waniganeththi. Influence of ^{73}Rb on the ashes of accreting neutron stars. *Phys. Rev. C*, 2020.

[21] VA Karnaukhov and NI Tarantin. On the possibility of proton decay of nuclei. *Zhur. Eksptl'. i Teoret Fiz.*, 39, 1960.

[22] M. Karny, K.P. Rykaczewski, R.K. Grzywacz, J.C. Batchelder, C.R. Bingham, C. Goodin, C.J. Gross, J.H. Hamilton, A. Korgul, W. Królas, S.N. Liddick, K. Li, K.H. Maier, C. Mazzocchi, A. Piechaczek, K. Rykaczewski, D. Schapira, D. Simpson, M.N. Tantawy, J.A. Winger, C.H. Yu, E.F. Zganjar, N. Nikolov, J. Dobaczewski, A.T. Kruppa, W. Nazarewicz, and M.V. Stoitsov. Shell structure beyond the proton drip line studied via proton emission from deformed ^{141}Ho. *Physics Letters B*, 664(1):52 – 56, 2008.

[23] G. F. Knoll. *Radiation Detection and Measurement.* 2000.

[24] Kenneth S Krane, David Halliday, et al. *Introductory nuclear physics.* 1987.

[25] S. M. Lenzi, N. Mărginean, D. R. Napoli, C. A. Ur, A. P. Zuker, G. de Angelis, A. Algora, M. Axiotis, D. Bazzacco, N. Belcari, M. A. Bentley, P. G. Bizzeti, A. Bizzeti-Sona, F. Brandolini, P. von Brentano, D. Bucurescu, J. A. Cameron, C. Chandler, M. De Poli, A. Dewald, H. Eberth, E. Farnea, A. Gadea, J. Garces-Narro, W. Gelletly, H. Grawe, R. Isocrate, D. T. Joss, C. A. Kalfas, T. Klug, T. Lampman, S. Lunardi, T. Martínez, G. Martínez-Pinedo, R. Menegazzo, J. Nyberg, Zs. Podolyak, A. Poves, R. V. Ribas, C. Rossi Alvarez, B. Rubio, J. Sánchez-Solano, P. Spolaore, T. Steinhardt, O. Thelen, D. Tonev, A. Vitturi, W. von Oertzen, and M. Weiszflog. Coulomb energy differences in $T = 1$ mirror rotational bands in ^{50}Fe and ^{50}Cr. *Phys. Rev. Lett.*, 87:122501, Aug 2001.

[26] G. Lorusso. *β-delayed proton emission in the* ^{100}Sn *region.* PhD thesis, Michigan State University, 2010.

[27] G. Lorusso, A. Becerril, A. Amthor, T. Baumann, D. Bazin, J. S. Berryman, B. A. Brown, R. H. Cyburt, H. L. Crawford, A. Estrade, A. Gade, T. Ginter, C. J. Guess, M. Hausmann, G. W. Hitt, P. F. Mantica, M. Matos, R. Meharchand, K. Minamisono, F. Montes, G. Perdikakis, J. Pereira, M. Portillo, H. Schatz, K. Smith, J. Stoker, A. Stolz, and R. G. T. Zegers. β-delayed proton emission in the ^{100}sn region. *Phys. Rev. C*, 86:014313, Jul 2012.

[28] G. Lorusso, A. Becerril, A. Amthor, T. Baumann, D. Bazin, J. S. Berryman, B. A. Brown, R. H. Cyburt, H. L. Crawford, A. Estrade, A. Gade, T. Ginter, C. J. Guess, M. Hausmann, G. W. Hitt, P. F. Mantica, M. Matos, R. Meharchand, K. Minamisono, F. Montes, G. Perdikakis, J. Pereira, M. Portillo, H. Schatz, K. Smith, J. Stoker, A. Stolz, and R. G. T. Zegers. β-delayed proton emission in the ^{100}Sn region. *Phys. Rev. C*, 86:014313, Jul 2012.

[29] S.M. Lenzi M.A. Bentley. Coulomb energy differences between high-spin states in isobaric multiplets. *Progress in Particle and Nuclear Physics*, 59(2):497–561, 2007.

[30] Zach Meisel, M. Santo, Heather Crawford, Richard Cyburt, Gwen Grinyer, Christoph Langer, F. Montes, H. Schatz, and Kotoga Smith. β-particle energy-summing correction

for β-delayed proton emission measurements. *Nuclear Instruments and Methods in Physics Research Section A: Accelerators, Spectrometers, Detectors and Associated Equipment*, 844, 11 2016.

[31] R. A. Meyer, R. J. Nagle, S. Brant, E. Frle, V. Paar, and P. K. Hopke. Interacting boson fermion model description for the levels of ^{71}Ge$_{39}$ populated in the beta decay of 65.30-h ^{71}As. *Phys. Rev. C*, 41:686–696, Feb 1990.

[32] A. Morales, Alejandro Algora, Berta Rubio, Kazunari Kaneko, Sumiko Nishimura, Pame Aguilera, S. Orrigo, Francisco Molina, Giacomo de Angelis, F. Recchia, G. Kiss, Vi Phong, Jin Wu, D. Nishimura, H. Oikawa, T. Goigoux, Jérôme Giovinazzo, P. Ascher, J. Agramunt, and S. Yagi. Simultaneous investigation of the T$_z$=1 (J$^\pi$ = 0$^+$) and T$_z$=0 (J$^\pi$ = 9$^+$) β decays in ^{70}Br. 04 2017.

[33] D. Morrissey. Production of unstable nuclei for astrophysical studies and the new accelerator project at msu. page 32, 09 2014.

[34] National Institute of Standards Technology. *Stardard Reference Material*, 9 1988. 4.

[35] J.A. Nolen and J.P. Schiffer. Coulomb energies. *Annual Review of Nuclear Science*, 19(1):471–526, 1969.

[36] M Oinonen, A Jokinen, J Äystö, P Baumann, F Didierjean, A Honkanen, A Huck, Marc Huyse, A Knipper, G Marguier, et al. β-decay of the proton-rich T$_z$=- 1/2 nucleus, ^{71}Kr. *Physical Review C*, 56(2):745, 1997.

[37] A. Petrovici, K.W. Schmid, and Amand Faessler. Microscopic description of the mirror nuclei ^{70}Se and ^{70}Kr. *Nuclear Physics A*, 728(3):396 – 414, 2003.

[38] A. M. Rogers, M. A. Famiano, W. G. Lynch, M. S. Wallace, F. Amorini, D. Bazin, R. J. Charity, F. Delaunay, R. T. de Souza, J. Elson, A. Gade, D. Galaviz, M.-J. van Goethem, S. Hudan, J. Lee, S. Lobastov, S. Lukyanov, M. Matoš, M. Mocko, H. Schatz, D. Shapira, L. G. Sobotka, M. B. Tsang, and G. Verde. Ground-state proton decay of ^{69}Br and implications for the ^{68}Se astrophysical rapid proton-capture process waiting point. *Phys. Rev. Lett.*, 106:252503, Jun 2011.

[39] A.M. Rogers et al. ^{69}Br β-delayed proton emission: A Trojan horse for studying states in proton-unbound ^{69}Br. *Phys. Rev. C*, 84:051306, 2011.

[40] Karl-Heinz Schmidt. A new test for random events of an exponential distribution. *The European Physical Journal A*, 8(1):141–145, 2000.

[41] Joshua Bradshaw Stoker. *β-decay Half-life of the Rp-process Waiting-point Nuclide* ^{84}Mo. Michigan State University, 2009.

[42] A Stolz, T Baumann, TN Ginter, DJ Morrissey, M Portillo, BM Sherrill, M Steiner, and JW Stetson. Production of rare isotope beams with the nscl fragment separator. *Nuclear Instruments and Methods in Physics Research Section B: Beam Interactions with Materials and Atoms*, 241(1-4):858–861, 2005.

[43] O. B. Tarasov, M. Portillo, A. M. Amthor, T. Baumann, D. Bazin, A. Gade, T. N. Ginter, M. Hausmann, N. Inabe, T. Kubo, D. J. Morrissey, A. Nettleton, J. Pereira, B. M. Sherrill, A. Stolz, and M. Thoennessen. Production of very neutron-rich nuclei with a ^{76}Ge beam. *Phys. Rev. C*, 80:034609, Sep 2009.

[44] O.B. Tarasov and D. Bazin. Lise++ : design your own spectrometer. *Nuclear Physics A*, 746:411 – 414, 2004. Proceedings of the Sixth International Conference on Radioactive Nuclear Beams (RNB6).

[45] B. O. ten Brink, R. D. Vis, A. W. B. Kalshoven, and H. Verheul. The decay of ^{70}Se. *Zeitschrift für Physik*, 270, 1974.

[46] B.O. Ten Brink, P. Van Nes, C. Hoetmer, and H. Verheul. On the structure of ^{71}As and ^{73}As. *Nuclear Physics A*, 338(1):24 – 44, 1980.

[47] R. G. Thomas. An analysis of the energy levels of the mirror nuclei, ^{13}C and ^{13}N. *Phys. Rev.*, 88(5):1109–1125, 1952.

[48] B. E. Tomlin, C. J. Barton, N. V. Zamfir, M. A. Caprio, R. L. Gill, R. Krücken, J. R. Novak, J. R. Cooper, K. E. Zyromski, G. Cata-Danil, C. W. Beausang, A. Wolf, N. A. Pietralla, H. Newman, J. Cederkall, Benyuan Liu, Z. Wang, R. F. Casten, and D. S. Brenner. Mass measurements of ^{70}Se, ^{71}Se, ^{72}Br, and ^{73}Br. *Phys. Rev. C*, 63:034314, Feb 2001.

[49] P Urkedal and I Hamamoto. Deformation and one-particle orbits in ^{71}Kr and ^{71}Br. *Physical Review C*, 58(4):R1889, 1998.

[50] A. Vitz-Sveiczer et al. Studying the exotic decay ^{70}Kr ^{70}Br. *Acta Physica Polonica B*, 51, 2020.

[51] D. D. Warner, M. A. Bentley, and P. Van Isacker. The role of isospin symmetry in collective nuclear structure. *Nature Physics*, 2(5):311–318, 2006.

[52] E. Wigner. On the consequences of the symmetry of the nuclear hamiltonian on the spectroscopy of nuclei. *Phys. Rev.*, 51:106–119, Jan 1937.

[53] K. Wimmer, W. Korten, T. Arici, P. Doornenbal, P. Aguilera, A. Algora, T. Ando, H. Baba, B. Blank, A. Boso, S. Chen, A. Corsi, P. Davies, G. de Angelis, G. de France, D.T. Doherty, J. Gerl, R. Gernhäuser, D. Jenkins, S. Koyama, T. Motobayashi, S. Nagamine, M. Niikura, A. Obertelli, D. Lubos, B. Rubio, E. Sahin, T.Y. Saito, H. Sakurai, L. Sinclair, D. Steppenbeck, R. Taniuchi, R. Wadsworth, and M. Zielinska. Shape coexistence and isospin symmetry in A=70 nuclei: Spectroscopy of the T_z=1 nucleus ^{70}Kr. *Physics Letters B*, 785:441 – 446, 2018.